

---

# Preserving Atomic Coherences for Light Storage in $\text{Pr}^{3+}:\text{Y}_2\text{SiO}_5$ Driven by an OPO Laser System

---

Erhaltung atomarer Kohärenzen zur Lichtspeicherung in  $\text{Pr}^{3+}:\text{Y}_2\text{SiO}_5$  unter Verwendung  
eines OPO Lasersystems Dissertation von Simon Robert Mieth, Oktober 2015



TECHNISCHE  
UNIVERSITÄT  
DARMSTADT

Fachbereich Physik  
Institut für Angewandte Physik  
Nichtlineare Optik und  
Quantenoptik

Bitte zitieren Sie dieses Dokument als:

URN: urn:nbn:de:tuda-tuprints-52348

URL: <http://tuprints.ulb.tu-darmstadt.de/id/eprint/5234>

Dieses Dokument wird bereitgestellt von tuprints,  
E-Publishing-Service der TU Darmstadt.

<http://tuprints.ulb.tu-darmstadt.de>



Die Veröffentlichung steht unter folgender Creative Commons Lizenz:  
Namensnennung - Keine kommerzielle Nutzung - Keine Bearbeitung 3.0  
Deutschland

<http://creativecommons.org/licenses/by-nc-nd/3.0/de/>

# Preserving Atomic Coherences for Light Storage in $\text{Pr}^{3+}:\text{Y}_2\text{SiO}_5$ Driven by an OPO Laser System

Vom Fachbereich Physik  
der Technischen Universität Darmstadt

zur Erlangung des Grades  
eines Doktors der Naturwissenschaften  
(Dr. rer. nat.)

genehmigte Dissertation  
von M.Sc. Simon Robert Mieth  
aus Berlin

Referent: Prof. Dr. Thomas Halfmann  
Korreferent: Prof. Dr. Thomas Walther

Tag der Einreichung: 12. 10. 2015  
Tag der Prüfung: 16. 11. 2015

Darmstadt 2016

D17



---

# Abbreviations

**AOM** Acousto-optical modulator

**CPM** Coherence population mapping

**cw** Continuous wave

**DDS** Direct digital synthesis

**DFG** Difference-frequency generation

**EIT** Electromagnetically induced transparency

**EOM** Electro-optical modulator

**FSR** Free spectral range

**FWHM** Full width half maximum

**HFS** Hyperfine structure

**HV** High voltage

**MgO:PPLN** Magnesium-oxide doped, periodically poled lithium niobate

**OPO** Optical parametric oscillation

**PDH** Pound-Drever-Hall (stabilization)

**PE** Peltier element

**PID** Proportional Integral Differential

**pp** Peak to peak

**Pr** Praseodymium

**PrYSO** Praseodymium-doped yttrium orthosilicate

**PSD** Power spectral density

**PZT** Piezo-electric transducer

**QPM** Quasi phase matching

---

**RAP** Rapid adiabatic passage  
**REIDC** Rare-earth-ion-doped crystal  
**RF** Radio frequency  
**RHD** Raman heterodyne detection  
**rms** Root mean square  
**SFG** Sum-frequency generation  
**SHG** Second-harmonic generation  
**SPE** Stimulated photon echo  
**TDSE** Time-dependent Schrödinger equation  
**ULE** Ultra-low expansion (glass)  
**Y** Yttrium  
**YSO** Yttrium orthosilicate

# Contents

<b>Introduction</b>	<b>1</b>
<b>1 Praseodymium-doped Yttrium Orthosilicate</b>	<b>3</b>
1.1 Free Praseodymium Ions . . . . .	3
1.2 Yttrium Orthosilicate Host Crystal . . . . .	4
1.3 Crystal Field Interaction . . . . .	4
1.4 Hyperfine Splitting . . . . .	5
1.5 Homogeneous and Inhomogeneous Broadening . . . . .	7
<b>2 Solid-State-Laser System</b>	<b>10</b>
2.1 Overview . . . . .	10
2.2 Sum- and Difference-Frequency Mixing . . . . .	12
2.3 Quasi Phase Matching . . . . .	15
2.4 Experimental Setup . . . . .	18
2.4.1 Design of the Nonlinear Crystal . . . . .	18
2.4.2 The OPO-SFG Setup . . . . .	20
2.4.3 Pound-Drever-Hall Frequency Stabilization . . . . .	22
2.5 Experimental Results . . . . .	29
2.5.1 Operation at 606 nm . . . . .	29
2.5.2 Tuning the SFG Output Wavelength . . . . .	30
2.5.3 Long-Term Operation . . . . .	32
2.5.4 Frequency-Stabilized Operation . . . . .	33
2.6 Conclusion . . . . .	37
<b>3 Coherent Light-Atom Interaction</b>	<b>38</b>
3.1 Interaction with a Two-State System . . . . .	38
3.1.1 Rabi Oscillations and Pulse Area . . . . .	39
3.1.2 Description of Macroscopic Systems . . . . .	40
3.2 Interaction with a Three-State System . . . . .	43
3.2.1 EIT-Based Light Storage . . . . .	44
3.2.2 Limitations of Storage Duration . . . . .	47
<b>4 Adiabatic Rephasing of Atomic Coherences</b>	<b>49</b>
4.1 Dephasing and Rephasing . . . . .	49
4.1.1 Limitations of $\pi$ Pulse Based Rephasing . . . . .	51
4.2 Adiabatic Interaction with a Two-State System . . . . .	51
4.2.1 Rapid Adiabatic Passage . . . . .	53
4.3 Rephasing by Rapid Adiabatic Passage . . . . .	55
4.3.1 Rephasing with Two RAP Pulses . . . . .	58

4.4	Experimental Setup . . . . .	60
4.4.1	Crystal and Cryostat . . . . .	61
4.4.2	Optical Setup . . . . .	61
4.4.3	Generation of Radio-Frequency Magnetic Fields . . . . .	62
4.4.4	Detection of Stored Light Signals . . . . .	63
4.4.5	Measurement Procedure . . . . .	63
4.5	Experimental Results . . . . .	66
4.5.1	Rephasing with Limited Rabi Frequency . . . . .	66
4.5.2	Rephasing with RF Field Inhomogeneities . . . . .	68
4.5.3	Rephasing with Varying Rabi Frequency . . . . .	70
4.5.4	Rephasing with a Static Detuning . . . . .	71
4.5.5	Perfect RAP Pulses . . . . .	72
4.6	Conclusion . . . . .	74
<b>5</b>	<b>Coherence Population Mapping</b>	<b>75</b>
5.1	Theoretical Background . . . . .	77
5.2	Stimulated Photon Echo . . . . .	81
5.2.1	Theoretical Background . . . . .	81
5.2.2	Comparison of CPM and SPE . . . . .	84
5.3	Experimental Setup . . . . .	85
5.3.1	Optical Setup . . . . .	85
5.3.2	Generation of Radio-Frequency Magnetic Fields . . . . .	86
5.3.3	Raman Heterodyne Detection . . . . .	87
5.3.4	Measurement Procedure . . . . .	89
5.4	Experimental Results . . . . .	91
5.4.1	Mapping Efficiency Depending on the Coherence Phase . . . . .	91
5.4.2	Mapping Efficiency Depending on the Storage Duration . . . . .	93
5.4.3	Light Storage with CPM and SPE . . . . .	96
	<b>Conclusions and Future Work</b>	<b>99</b>
	<b>Zusammenfassung</b>	<b>101</b>
<b>A</b>	<b>Ground-State Population-Relaxation Times</b>	<b>104</b>
<b>B</b>	<b>Laser-Linewidth Measurement via Spectral Holeburning</b>	<b>105</b>
<b>C</b>	<b>Supplementary CPM and SPE Measurements</b>	<b>106</b>
<b>D</b>	<b>Single- and Two-Frequency Impedance-Matching</b>	<b>107</b>
	<b>Bibliography</b>	<b>109</b>
	<b>Publications and Contribution to Conferences</b>	<b>117</b>
	<b>Supervised Theses and Contribution to Teaching</b>	<b>120</b>
	<b>Curriculum Vitae</b>	<b>121</b>
	<b>Acknowledgement</b>	<b>122</b>



# Introduction

Efficient quantum information storage is of growing importance to modern computation and communication networks. Storage is crucial in order to extend the complexity of computation, to synchronize communication processes or to provide long distance data transfer. However, storage devices are often based on electronics that are meant to store classical information bits. Quantum information on the other hand is based on the phenomena of quantum mechanics, i.e., a quantum state can be a superposition of two states, which is impossible in classical information. The properties of quantum states enable novel applications, e.g., implementation of quantum computing algorithms [1], quantum cryptography or the setup of quantum networks [2]. Thus, future quantum memories should preserve the full quantum state. The interaction between light and matter on a quantum level exhibits promising approaches towards storing and processing quantum information [3,4]. Light is a fast and efficient transmitter and a light pulse contains phase, amplitude, polarization and propagation direction, i.e., many degrees of freedom to encode information.

In order to realize optical data storage, a number of proposals are currently investigated, which aim for high efficiency, multi-mode capacity and long storage duration in future light storage devices [3–8]. A prominent approach towards light storage is based on electromagnetically induced transparency (EIT) [7,9,10]. EIT-based memories use a classical laser field to manipulate absorption and dispersion properties of a medium to enable lossless propagation and stopping of light pulses. The information of the light pulse is thereby transformed into a manifold of persistent atomic coherences, i.e., a superposition of two atomic states. The EIT-based memory preserves the full quantum state of the input light pulse and enables on-demand read-out of the latter from the atomic coherence. EIT-based light storage was first realized in vapors [11,12] and cold atomic gases [13], which exhibit excellent spectral properties. However, gaseous media suffer from diffusion, collisions and technically challenging setups. Rare-earth-ion doped crystals (REIDC) on the other hand provide atom-like spectral properties in combination with the advantages of solids, i.e., scalability, localized interaction centers and easier handling. REIDCs have therefore experienced growing attention for the use as quantum memories [14–18]. This work is embedded in a project to develop and improve an efficient, long-term solid-state memory for coherent light pulses and in the future also for single photons. In particular, we extend an EIT-based memory in the REIDC praseodymium-doped yttrium orthosilicate (PrYSO) with a novel laser system and experimental procedures to achieve efficient rephasing and easily accessible, ultra-long storage durations. The thesis is structured as follows:

**Chapter 1** gives a short introduction to the storage medium PrYSO. It contains the main spectroscopic properties of the relevant level structure as well as an overview about relevant interactions and processes within the PrYSO crystal.

**Chapter 2** presents the first objective of our work, i.e., the setup of a laser system at the wavelength  $\lambda = 606\text{ nm}$  for coherent manipulations in PrYSO. In previous experiments, this rather exceptional wavelength was generated by a dye laser. These systems provide widely tunable output with sufficient continuous wave power  $\sim 1\text{ W}$  in the visible spectrum and have been successfully frequency stabilized to sub-kHz level [19]. However, dye lasers contain complex optical resonators and require a high level of maintenance, which complicates their use in non-laboratory environments. Our required wavelength is otherwise only available from frequency mixing of two phase-locked lasers or laser systems based on nonlinear frequency generation [20–22]. However, these systems obtained so far only little output power or suffered from output instabilities on longer time scales. Here, we present a novel approach based on optical parametric oscillation and intra-cavity sum-frequency generation in periodically-poled lithium niobate to generate tunable, visible output. Our solid-state system is meant as an approach towards robust laser sources in the visible and for future quantum memories.

**Chapter 3** introduces coherent light matter interactions. These form the basis of EIT-based light storage and for all procedures that we implement to enhance storage time and efficiency of our EIT-based memory.

**Chapters 4 and 5** present our efforts to prolong the storage duration in our memory. The storage time is limited by the life-time of an atomic coherence in PrYSO. Dephasing and decoherence reduce the latter to times, which are typically shorter than the theoretical maximum given by twice the population life-time.

**Chapter 4** presents the work on efficient compensation of dephasing. The latter is caused by inhomogeneous broadening, which leads to different (but deterministic) phase evolutions for individual coherences. After a typically very short dephasing time, this leads to destructive interference and prevents a read-out of the memory. However, the application of pulsed radio-frequency (RF) magnetic fields can rephase the coherences. Most common rephasing sequences use  $\pi$  pulses, which are tied to strict conditions and therefore sensitive to errors. In our work, we implement rephasing by adiabatic pulses. These are known for robust and efficient manipulation of quantum systems [23, 24] and we experimentally compare their rephasing capabilities to rephasing with  $\pi$  pulses.

Beyond dephasing, the coherence life-time suffers from decoherence, i.e., statistical phase changes caused by fluctuations in the crystal environment. Dynamic and static decoupling from the environment is one way to increase the decoherence time towards its theoretical maximum [25–29]. However, these techniques require precisely chosen static and RF magnetic fields and make experiments quite complex. **Chapter 5** presents an alternative approach to reach ultra-long storage times by reversibly mapping coherences onto long-lived populations with a short writing and reading sequence. The storage duration is thus insensitive to decoherence and only limited by population relaxation. We implement and investigate our novel coherence population mapping (CPM) protocol in PrYSO and compare it to the well-known stimulated photon echo storage protocol [30, 31].

# Chapter 1

## Praseodymium-doped Yttrium Orthosilicate

This work deals with coherent storage and retrieval of optical or radio-frequency (RF) information, whereat the storage medium is a rare-earth-ion-doped crystal (REIDC). In comparison to many solids, REIDCs typically provide narrow homogeneous broadening and therefore good coherence properties. This atom-like characteristic and the fact that solids enable easy handling, scalability and potential high optical depth, make REIDCs suitable media for solid state memories either for classical or quantum information [15–18].

In this work, all light storage and related experiments are performed in a praseodymium-doped yttrium orthosilicate crystal (hereafter termed PrYSO), which is a favorable storage medium, because it combines relatively high oscillator strength, long-lived ground states and good coherence properties.

This chapter presents all relevant spectroscopic properties of PrYSO, which are important to understand the results presented in this thesis. This includes the relevant energy levels, line broadening mechanisms and a spectroscopic characterization of the relevant optical and RF transitions. Complementary information is provided by e.g., [32, 33].

### 1.1 Free Praseodymium Ions

Praseodymium (Pr) is an element of the lanthanide group that has only one stable isotope,  $^{141}_{59}\text{Pr}$ . Along with scandium (Sc) and yttrium (Y), the lanthanides are more commonly termed rare-earth elements. The electronic configuration of  $\text{Pr}^{3+}$  ions is  $[\text{Xe}]4f^2$ , with two free electrons in the 4f shell, which contains all relevant transitions. The fully populated 5s and 5p shells have a larger spatial extent than the 4f shell. This electronic configuration results in an electronic shielding of the 4f electrons and provides rather narrow homogeneous linewidth for the 4f-transitions [34, 35]. The energy levels of a free ion are determined by the eigenvalues of the Hamilton operator

$$\hat{H}_{\text{FI}} = \hat{H}_0 + \hat{H}_C + \hat{H}_{\text{SO}}. \quad (1.1)$$

$\hat{H}_0$  is the unperturbed Hamiltonian of the 4f-electrons in the field of the Pr-nucleus. The Coulomb interaction between the electrons is represented by  $\hat{H}_C$  and the spin-orbital interaction by  $\hat{H}_{\text{SO}}$ . The level scheme of a free Pr ion is shown in figure 1.1, in which the relevant levels are the  $^3\text{H}_4$  ground and the  $^1\text{D}_2$  optically excited state (written in Russel-Saunders notation  $^{2S+1}L_J$ ). Note that in the free ion this transition is still dipole forbidden, a restriction that is not present when praseodymium is doped in a host crystal.

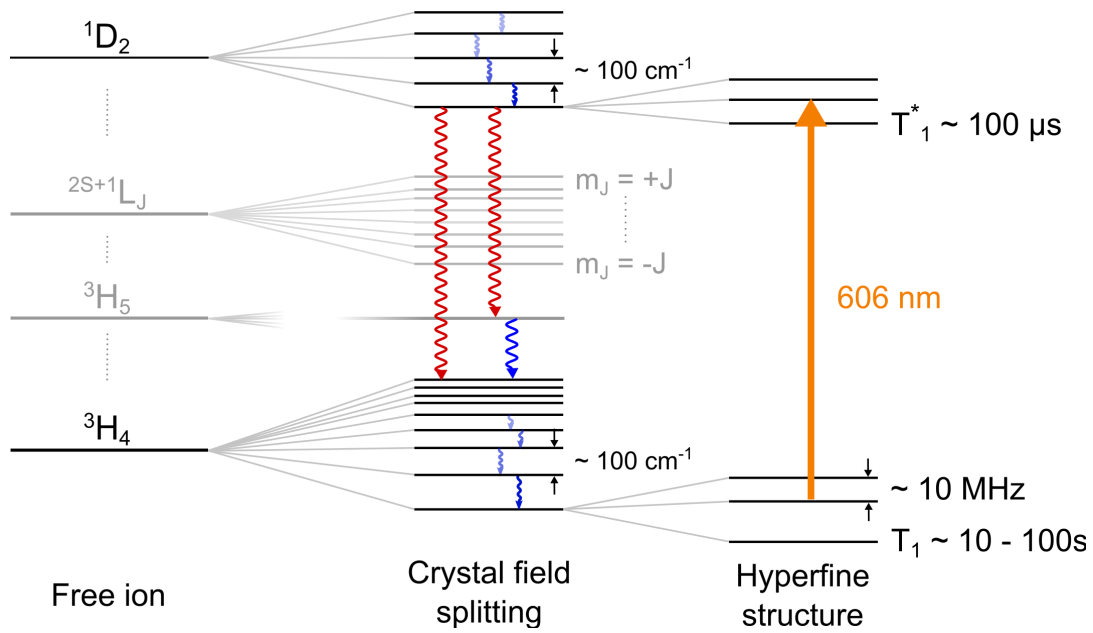


Figure 1.1: (Left) Relevant energy levels of a free Pr ion, (center) after the interaction of the latter with the host crystal field and (right) the relevant hyperfine levels for this work. Spectroscopic data taken from [33]

## 1.2 Yttrium Orthosilicate Host Crystal

Yttrium orthosilicate (YSO) is a monoclinic crystal with  $C_{2h}^6$  symmetry and four  $Y_2SiO_5$  molecules per unit cell [36]. In order to dope the host matrix with Pr ions, some of the Y ions are replaced with the latter. This is a favorable exchange because both ion radii are of similar size and thus only weak crystal deformation occurs. Furthermore, Y ions have only a weak nuclear magnetic moment, resulting in weak interaction between a Pr ion and the host crystal environment [34]. In each unit cell, Y ions (and possible dopant locations, respectively), occur in two different crystallographic sites, each with the low  $C_1$  symmetry [37]. Different crystal environments result in slightly different spectroscopic properties for each site. All experiments presented in this thesis are performed in ions at site 1. These exhibit a larger transition dipole moment and have an optical transition with a wavelength of  $\lambda = 606$  nm for the  $^3H_4 \leftrightarrow ^1D_2$  transition [38]. In addition, each crystallographic site involves two magnetic sites, resulting from opposing alignments of the nuclear magnetic spins with respect to the  $C_2$  crystal axis. In the crystal used in this thesis, 0.05% of  $Y^{3+}$  ions are replaced with  $Pr^{3+}$  ions.

## 1.3 Crystal Field Interaction

When praseodymium is doped into YSO, its spectroscopic properties change as indicated in figure 1.1. Due to the low crystal symmetry, the degeneracy with respect to the total angular momentum  $J$  vanishes, the free ion's energy levels are Stark shifted and split up by the crystal's electric field into  $2J + 1$  levels. The

energy spacing between these  $J$ -multiplets is about  $1000 \text{ cm}^{-1}$  [32] and the energy spacing within a multiplet is of the order of  $100 \text{ cm}^{-1}$  [33]. For each ion, the crystal field also leads to a superposition of alternative electron configurations with different parity, such as  $[\text{Xe}]4f^{N-1}5d$ , and the  $[\text{Xe}]4f^2$  configuration. The result is a weakly allowed transition  ${}^3\text{H}_4 \leftrightarrow {}^1\text{D}_2$ . The corresponding weak transition moment also leads to a rather long population life-time for the optically excited state  ${}^1\text{D}_2$ . However, when population is excited, it decays not only directly to the lowest crystal field state  ${}^3\text{H}_4(m_J = -4)$ , but also to  ${}^3\text{H}_4(m_J > -4)$  or  ${}^3\text{H}_5$  states, as indicated in figure 1.1 by the red arrows. From these intermediate states the population eventually relaxes without emission of radiation back to the lowest crystal field state (indicated by the blue arrows in figure 1.1). Here the relevant, responsible relaxation process is phonon excitation. Of course, phonon absorption can also lead to electron excitation to higher crystal fields or within a  $J$ -multiplet, which is why the crystal is kept at cryogenic temperatures below 5 K to prevent additional, thermal excitation of phonons. The multiple decay channels lead to a population life-time in the excited state of the order of  $T_1^* \sim 100 \mu\text{s}$ .

## 1.4 Hyperfine Splitting

The levels within a  $J$ -multiplet show an additional hyperfine splitting, which results from the interaction between 4f-electrons and the nuclear spin of the Pr ions ( $I = 5/2$ ) as well as the interaction of the nuclear spin with the surrounding crystal field. The crystal field levels split up into three, twofold degenerated, states, which are labeled with the quantum number  $m_I$  to  $|\pm 5/2\rangle$ ,  $|\pm 3/2\rangle$  and  $|\pm 1/2\rangle$  (see figure 1.1 (right) and figure 1.2). Praseodymium has an even number of electrons ( $N=2$ ), which is why the electronic levels are singlet states. In the crystal field, this leads to a vanishing angular momentum  $J$  in first order. Consequently, the coupling  $\vec{I} \cdot \vec{J}$  vanishes in first order and the resulting hyperfine splitting is only of the order of  $\sim 10 \text{ MHz}$ .

The second contribution to the hyperfine splitting is the interaction between the electronic nuclear quadrupole moment of the Pr ions and the inhomogeneous crystal field caused by all surrounding charge carriers. This interaction is of similar order as the second order hyperfine splitting and both contributions are summarized in an effective quadrupole Hamiltonian  $\hat{H}_Q$  [39].

In the presence of an external, static magnetic field, the hyperfine levels further split into Zeeman levels. However, the Zeeman levels are not of significant importance to any of the experiments presented in this thesis and thus the relevant hyperfine splitting is only determined by the effective quadrupole interaction.

The hyperfine structure (HFS) includes all relevant transitions for this work.

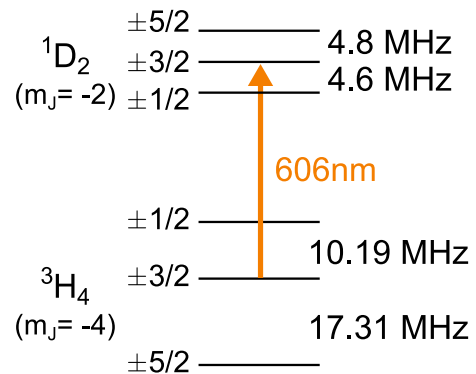


Figure 1.2: Relevant hyperfine splitting in PrYSO.

More precisely, all experiments are performed within the hyperfine levels of the lowest crystal field states  ${}^3\text{H}_4(-4)$  and  ${}^1\text{D}_2(-2)$ . Note that whenever (optical or RF) information is stored in Pr:YSO in the presented work it is encoded in a coherent superposition or in a population distribution within the ground state HFS levels of  ${}^3\text{H}_4(-4)$ . All optical fields couple the HFS levels in the  $|{}^3\text{H}_4(-4)\rangle \leftrightarrow |{}^1\text{D}_2(-2)\rangle$  transition.

Table 1.1 gives the experimentally determined relative oscillator strength for all nine possible transitions between ground and optically excited states [40]. From the table it is obvious that Pr:YSO provides an effective four and two level system (colored slots).

Table 1.1: Relative oscillator strength  $f$  between the hyperfine levels of electronic ground state  ${}^3\text{H}_4(-4)$  and optically excited state  ${}^1\text{D}_2(-2)$  in Pr:YSO according to [40].

${}^3\text{H}_4(-4) \backslash {}^1\text{D}_2(-2)$	$ \pm \frac{1}{2}\rangle$	$ \pm \frac{3}{2}\rangle$	$ \pm \frac{5}{2}\rangle$
$ \pm \frac{1}{2}\rangle$	$f = 0,55$	$f = 0,38$	$f = 0,07$
$ \pm \frac{3}{2}\rangle$	$f = 0,4$	$f = 0,6$	$f = 0,01$
$ \pm \frac{5}{2}\rangle$	$f = 0,05$	$f = 0,02$	$f = 0,93$

The hyperfine levels, especially those of the ground state, provide advantages for the presented experiments (the quantities of interest for the hyperfine states are summarized in table 1.2). First of all, the ground state hyperfine levels exhibit rather long population relaxation times. This is advantageous for all experiments that demand long term stable population distributions, as will be discussed in chapter 5. Note that the relaxation time  $T_1(|1\rangle \leftrightarrow |2\rangle)$  is about a magnitude smaller than  $T_1(|2\rangle \leftrightarrow |3\rangle)$ , as was determined by our own quantitative measurements (see Appendix A). The population relaxation time defines an upper, theoretical limit for the decoherence time. However, the latter is also determined by other interactions and has been measured to be  $T_2 \approx 500 \mu\text{s}$  in good agreement with other experiments [41]. Next, the energy difference between the hyperfine levels is rather small, i.e., the transition frequency is in the range of  $\sim 10 \text{ MHz}$ . This enables direct control of coherent superpositions or population distributions in the HFS via RF magnetic fields.

Table 1.2: Relevant spectroscopic quantities of the ground and excited state HFS levels.

Ground state $^3H_4(-4)$	
Population relaxation times (at $T = 4\text{K}$ )	$T_1( 1\rangle \leftrightarrow  2\rangle) = 8.7\text{ s}$ $T_1( 2\rangle \leftrightarrow  3\rangle) = 109.5\text{ s}$
Decoherence time	$T_2 \approx 500\ \mu\text{s}$
Homogeneous broadening HFS transitions	$\Gamma_h^{\text{HFS}} \approx 650\text{ Hz}$ [41]
Inhomogeneous broadening HFS transitions	$\Gamma_{\text{inh}}^{\text{HFS}}( 1\rangle \leftrightarrow  2\rangle) \approx 40\text{ kHz}$ $\Gamma_{\text{inh}}^{\text{HFS}}( 2\rangle \leftrightarrow  3\rangle) \approx 80\text{ kHz}$
Excited state $^1D_2(-2)$	
Population life-time	$T_1^* = 164\ \mu\text{s}$ [38]
Decoherence time	$T_2^* \approx 111\ \mu\text{s}$ [38]
Homogeneous broadening optical transition	$\Gamma_h^{\text{opt}} \approx 2.8\text{ kHz}$ [38]
Inhomogeneous broadening optical transition	$\Gamma_{\text{inh}}^{\text{opt}} \approx 7\text{ GHz}$

## 1.5 Homogeneous and Inhomogeneous Broadening

Transitions within the 4f shell of rare-earth-ion-doped solids show a rather narrow linewidth. The homogeneous portion of the linewidth  $\Gamma_h$  of a transition is given by  $\Gamma_h = (\pi T_2)^{-1}$ . As mentioned above, the decoherence time  $T_2$  has a theoretical maximum set by the population decay time  $T_1$  of  $T_2 = 2T_1$ . In addition to population decay, also other effects contribute to decoherence [34, 38].

The first is the spin-ion contribution  $\Gamma_{\text{spin-ion}}$  that results from an interaction between the Pr ion and fluctuating spins in its environment. A second contribution is given by ion-ion interaction which produces a shift of the transition frequency in the presence of a neighbouring, excited Pr ion through dipole-dipole interaction. The last contribution to homogeneous broadening is phononic interaction with the electrons. This directly affects population relaxation in which the excitation of phonons causes relaxation of population to lower crystal field levels. Absorption of phonons excites electrons to higher crystal field levels. Phononic interaction can be reduced by cooling the crystal to cryogenic temperatures below 5 K. The resulting homogeneous linewidth for the relevant optical transition in Pr:YSO is  $\Gamma_h^{\text{opt}} \approx 2.8\text{ kHz}$  [38]. The homogeneous linewidth for the  $^3H_4(-4)$  hyperfine transitions is  $\Gamma_h^{\text{HFS}} \approx 650\text{ Hz}$  [41].

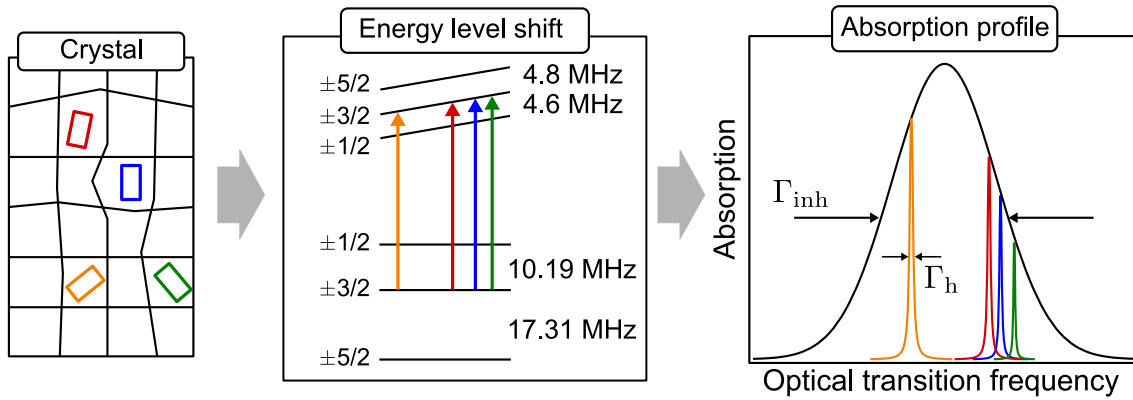


Figure 1.3: Origin of static inhomogeneous broadening. (Right) Differently located praseodymium dopants (colored rectangles) experience a heterogeneous crystal field which causes a varying Stark shift for the (optical) transition frequency between the hyperfine levels (central box). (Right) A variety of transitions (each homogeneously broadened with  $\Gamma_h$ ) gives the inhomogeneously broadened optical line with a width  $\Gamma_{inh}$ .

## Inhomogeneous Broadening

The observed spectral lines in REIDCs usually exhibit a larger linewidth than expected from the homogeneous linewidth. This is due to inhomogeneous broadening which originates from a crystal environment that varies from site to site. Hence ions at different locations experience different crystal fields as indicated in figure 1.3 (left side). The difference of environments is mainly due to crystal defects such as vacancies, chemical impurities or mechanical stress, e.g., due to the doping itself. Consequently, the inhomogeneous broadening also depends strongly on the dopant concentration, similar to the homogeneous linewidth. Therefore, usually low dopant concentrations  $\ll 1\%$  are used. Different crystal fields yield a slightly different level shift of the crystal-field states. Thus, the transition frequency varies and we observe a broadening of the measured transition (see figure 1.3 center and right side). All ions with the same, i.e., non-distinguishable transition frequency are labeled as one frequency *ensemble*.

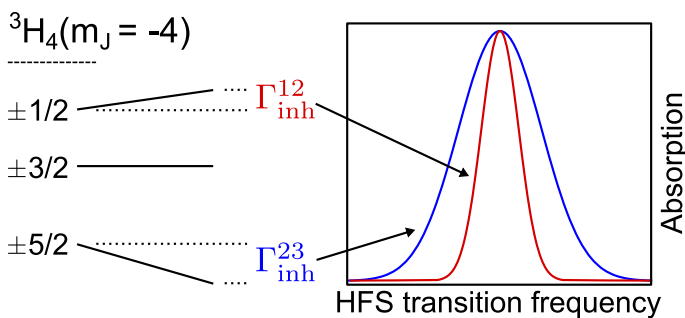


Figure 1.4: Inhomogeneous broadening of the ground state hyperfine transitions.

Note that not only the optical transition is inhomogeneously broadened, as indicated in figure 1.3. The RF transitions within the hyperfine states also exhibit inhomogeneous broadening, caused by the same effects as the broadening of the optical transition (see figure 1.4). The respective frequency shift in the optical, as well as in the two RF transitions, is correlated. Thus the deviation

of optical or RF transition frequencies from the center of the corresponding inhomogeneous line happens with the same ratio in each individual ion or ensemble,



respectively [42], i.e.,  $\Gamma_{\text{inh}}^{\text{HFS}-1} / \Gamma_{\text{inh}}^{\text{HFS}-2} = \text{const}$  etc.

So far, this section introduced the inhomogeneous broadening as an effect that causes a static shift of transition frequencies due to the inhomogeneous crystal field. However, there is also a dynamic broadening mechanism, which is caused by spin-ion interaction of surrounding Y spins with a Pr ion. If a stochastic Y spin flip occurs, it causes an uncorrelated, sudden shift of the transition frequency of the Pr ion via magnetic dipole-dipole interaction. Thus, the ion resonance is moved spectrally within the inhomogeneous line. Spin flips are therefore a source of dynamical, temporally varying, inhomogeneous broadening, known as *spectral diffusion* [33, 43, 44]. Note that the impact of spectral diffusion also depends on various crystal parameters such as dopant concentration, i.e., the distance between interacting ions or the magnitude of nuclear spin moments. For a crystal with identical parameters as the crystal used during this thesis, spectral diffusion causes frequency shifts in the range of  $\sim 100$  Hz [25].

Both optical and HFS inhomogeneous broadening, as indicated in table 1.2, play a significant role for this work. The inhomogeneous optical broadening necessitates an optical preparation in order to address only defined ensembles, as otherwise, a single-frequency laser-beam would always couple to nine different transitions (see chapter 4.4.5). Inhomogeneous HFS broadening has an even higher impact because it affects the efficiency of RF pulses acting on the ground state HFS transitions. Indeed, a central part of this work relies on the application of such RF pulses to enhance efficiency and storage duration for (optical) information storage. Consequently, some effort of this work also focuses on minimizing the influence of  $\Gamma_{\text{inh}}^{\text{HFS}}$ .

## Chapter 2

### Solid-State-Laser System

The preceding chapter introduced the storage medium PrYSO with its relevant optical transition at  $\lambda = 606$  nm. This chapter describes a solid-state-laser system to provide this radiation. It was set up as an alternative to an already existing ring dye laser system with the motivation to replace the latter because of its high maintenance requirements. Furthermore, dye lasers require quite complex optical resonators to guarantee single longitudinal mode operation with a reasonable frequency linewidth. Therefore, dye lasers are typically unsuitable in non-laboratory environments, making real life applications rather difficult.

The alternative laser system presented in this chapter operates on the basis of two frequency-mixing processes in an all solid state approach similar to a system described by Bosenberg et al. [22]. In contrast to the approach in [22], our laser system also allows for coarse tuning the output wavelength.

It was developed in collaboration with the company Aculight and is based on a commercially available, tunable continuous wave (cw) optical parametric oscillator, which has proven to be most robust, e.g., able to operate under helicopter flight conditions. Light storage experiments require the system to provide high cw output power ( $\sim 1$  W) and narrow frequency linewidth in the range of  $\Delta\nu \approx 100$  kHz. In order to fulfill the latter requirement, we complement the laser setup with a Pound-Drever-Hall frequency stabilization.

This chapter is arranged as follows. First, it overviews the basic idea of our laser system. The next section discusses second-order frequency-mixing processes, the very relevant issue of phase matching and the basics of frequency stabilization. The subsequent sections describe the experimental setup and present an experimental characterization of the free-running and frequency-stabilized laser system.

#### 2.1 Overview

The laser system consists of an all solid-state fiber-laser system serving as a pump source for two frequency-mixing processes in a nonlinear medium. This nonlinear medium is the key feature of our laser system. It is a lithium niobate crystal which converts pump radiation at  $\lambda_p = 1064$  nm into visible radiation at  $\lambda_{\text{vis}} = 606$  nm. The frequency conversion happens in two steps, optical parametric oscillation (OPO) and single pass sum-frequency generation (SFG), both are second-order ( $\chi^{(2)}$ ) nonlinear processes. Figure 2.1 sketches this basic idea. In the OPO, a pump photon with energy  $\hbar\omega_p$  is split by difference-frequency generation into two photons obeying energy conservation  $\hbar\omega_p = \hbar\omega_s + \hbar\omega_i$ . These photons are called

*signal* and *idler* and here they have wavelengths of  $2\pi c/\omega_s = \lambda_s = 1407$  nm and  $2\pi c/\omega_i = \lambda_i = 4365$  nm. In the subsequent SFG section, the signal photon is mixed with a pump photon to a visible output at  $2\pi c/\omega_{\text{vis}} = \lambda_{\text{vis}} = 606$  nm according to the sum-frequency relation  $\hbar\omega_{\text{vis}} = \hbar\omega_p + \hbar\omega_s$ . However, any pair of photons obeying energy conservation could theoretically be generated in these two frequency-mixing processes. This enables a broad possible output wavelength spectrum from a single device. However, besides conservation of energy, photons must also obey conservation of momentum, which is not only dependent on the wavelength but also on the wavelength dependent refractive index. If the corresponding momenta are not equal, the contributing beams propagate with different phase velocities through the crystal and interfere destructively after a certain distance. Hence, no macroscopic wave can be built up and there will not be any notable output radiation. In our approach we use *quasi phase matching* (QPM) [45, 46] in order to compensate the phase velocity mismatch for specific wavelengths out of the broad possible spectrum.

QPM is based on periodic poling [47, 48], which is established by dividing the crystal into small sections that exhibit an alternating sign of the nonlinear susceptibility  $\chi^{(2)}$ . Periodic poling compensates a given phase mismatch when the poling period is properly chosen. Allowing a phase mismatch and compensating it with a proper section length also allows the implementation of several mixing processes on a single crystal by changing the poling period. In our setup both OPO and SFG are phase matched in consecutive sections on the crystal. Moreover, the poling period varies perpendicularly to the beam direction, allowing for coarse tuning of the wavelength depending on the pump beam position within the crystal. Phase matching is presented in section 2.3. Usually, nonlinear processes require quite high powers to run efficiently and generate notable output. Therefore, we use a powerful pump source, providing continuous wave pump radiation with a power up to  $P_p = 16$  W. In addition, the crystal is placed inside an optical cavity, resonant for the signal wave generated in the OPO process. Due to the resulting high intra-cavity signal power, also the single-pass SFG runs efficiently.

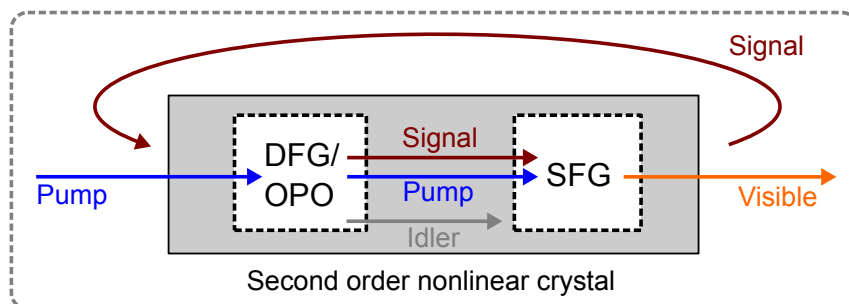


Figure 2.1: A nonlinear crystal converts photons of a pump source (not shown) in a two step process via difference-frequency generation (DFG) and sum-frequency generation (SFG) into desired, visible photons. A cavity guides the signal beam back into the crystal, thus the DFG acts as optical parametric oscillation (OPO).

## 2.2 Sum- and Difference-Frequency Mixing

Frequency mixing occurs when a medium reacts non linearly to one or many incident electric fields  $\vec{E}(\omega, z, t)$ . A convenient way to describe this response is given by the polarization  $\vec{P}$  of a nonlinear medium, where  $\vec{P}$  itself acts as a source of a new electric field driven by the incident fields. In this section, only a brief summary with the most important equations to describe sum- and difference-frequency generation (which is the basis for optical parametric oscillation) will be given. A detailed description of frequency mixing processes can be found in, e.g., [46].

The polarization in a lossless medium can be expressed in the form of a power series

$$\vec{P}(z, t) = \epsilon_0 \chi^{(1)} \sum_n \vec{E}(\omega_n, z, t) + \epsilon_0 \sum_{j,k} \sum_{nm} \chi_{ijk}^{(2)} E_j(\omega_n, z, t) E_k(\omega_m, z, t) \vec{e}_i + \text{HO} \quad (2.1)$$

where  $\epsilon_0$  is the dielectric constant in vacuum,  $\chi^{(1)}$  is the linear susceptibility tensor,  $\chi^{(2)}$  is the second-order nonlinear susceptibility tensor with entries  $\chi_{ijk}^{(2)}$ . The indices  $ijk$  refer to Cartesian coordinates.  $\vec{E}(\omega_n, z, t)$  are the electric field components with angular frequency  $\omega_n$  interacting with the nonlinear medium. In our case all propagate along the  $z$ -direction and have the form

$$\vec{E}(\omega_n, z, t) = \vec{A}_n \cdot \exp^{-i(\omega_n t - k_n z)} + c.c. \quad (2.2)$$

with wave vectors  $k_n = (2\pi n(\omega_n))/\lambda_n$  with the refractive index  $n$  and amplitudes  $\vec{A}_n$ . For simplicity we assume that all electric field components have the same linear polarization, i.e., all  $\vec{A}_n$  are pointing in the same direction and all beams have a fixed, equal propagation direction. Thus all electric fields and the polarization are taken as scalar quantities. Under the condition of a lossless medium (i.e., all frequencies  $\omega_n$  are far away from resonances), and fixed propagation and polarization vectors for the electric fields, it is possible to write the entries of  $\chi^{(2)}$  in the contracted notation with an effective nonlinear coupling constant  $d_{\text{eff}} = (1/2)\chi^{(2)}$  [46, 49]. Note that also the susceptibility is frequency dependent and  $d_{\text{eff}} = d_{\text{eff}}(\omega_1, \omega_2, \dots)$  is a function of the frequencies involved in the mixing process. Sum-frequency generation (SFG) and optical parametric oscillation (OPO), which is based on difference-frequency generation (DFG) are second-order processes. Therefore only the second term of equation (2.1) will be considered in this chapter. Both, SFG and DFG require two incident electric field components  $E_1$  and  $E_2$  and hence, the second-order polarization  $P^{(2)}(t)$  at any location in the medium, e.g.,  $z = 0$  reads

$$\begin{aligned} P^{(2)}(t) &= 2\epsilon_0 d_{\text{eff}} \left( A_1 e^{-i\omega_1 t} + A_2 e^{-i\omega_2 t} + c.c. \right)^2 \\ &= 2\epsilon_0 \left[ 2d_{\text{eff}}(\omega_1) |A_1|^2 + 2d_{\text{eff}}(\omega_2) |A_2|^2 \right. \\ &\quad \left. + \underbrace{d_{\text{eff}}(\omega_1, 2\omega_1) A_1^2 e^{-i2\omega_1 t}}_{\text{SHG}} + \underbrace{d_{\text{eff}}(\omega_2, 2\omega_2) A_2^2 e^{-i2\omega_2 t}}_{\text{SHG}} \right. \\ &\quad \left. + \underbrace{2d_{\text{eff}}(\omega_1, \omega_2, \omega_1 + \omega_2) A_1 A_2 e^{-i(\omega_1 + \omega_2)t}}_{\text{SFG}} + \underbrace{2d_{\text{eff}}(\omega_1, \omega_2, \omega_1 - \omega_2) A_1 A_2^* e^{-i(\omega_1 - \omega_2)t}}_{\text{DFG}} + c.c. \right] \end{aligned} \quad (2.3)$$

Note that in the further description we omit the frequency dependence of  $d_{\text{eff}}$ . The second-order polarization exhibits non oscillating terms, known as optical rectification. All other terms oscillate with either twice the original frequencies, which is known as second-harmonic generation (SHG) or with sum- and difference-frequency of two incident spectral components  $\omega_1$  and  $\omega_2$ . The latter two consequently describe SFG and DFG in a nonlinear medium.

Equation (2.3) shows how new frequencies are generated within a nonlinear medium at a single position, i.e.,  $z = 0$ . Thus, SFG and DFG provide tools for the generation of in principle any new frequency  $\omega_3$ , just depending on the two input frequencies  $\omega_1$  and  $\omega_2$ . However, equation (2.3) is only valid for a single position along the propagation direction. In order to build up a macroscopic output beam, it is inevitable to include the spatial phase evolution along the entire interaction length within the medium, given by the spatial phase factor  $\exp(ikz)$ . The spatial evolution of all contributing beams is described by the wave equation, derived from the Maxwell equations and reads

$$\frac{d^2}{dz^2}E_j - \frac{n_j^2}{c_0^2} \frac{\partial^2 E_j}{\partial t^2} = \frac{1}{\epsilon_0 c_0^2} \frac{\partial^2 P_j^{NL}}{\partial t^2} \quad (2.4)$$

Equation (2.4) describes how the nonlinear polarization  $P_j^{NL}$  acts as a source for an electric field  $E_j$  with the specific frequency component  $\omega_j$ . It is valid for every frequency component  $j$  of the electric field separately. Equation (2.3) already contains the information about which nonlinear polarization term generates a certain frequency and thus we can directly use  $E_j$  and  $P_j^{(2)}$  for the required processes, i.e., SFG or DFG. In the case of SFG we find

$$E_j = E_3 = A_3 e^{-i(\omega_3 t - k_3 z)} \quad (2.5)$$

and

$$P_j^{(2)} = P_3^{(2)} = 4\epsilon_0 d_{\text{eff}} A_1 A_2 e^{i(k_1 + k_2)z} e^{-i(\omega_1 + \omega_2)t} = 4\epsilon_0 d_{\text{eff}} A_1 A_2 e^{i(k_1 + k_2)z} e^{-i\omega_3 t} \quad (2.6)$$

The wave equation (2.4) along the  $z$ -direction then reads

$$\begin{aligned} & \left( \frac{d^2 A_3}{dz^2} + 2ik_3 \frac{dA_3}{dz} - k_3^2 A_3 + \frac{n_3^2 \omega_3^2 A_3}{c_0^2} \right) e^{-i(\omega_3 t - k_3 z)} + c.c. \\ & = \frac{-4d_{\text{eff}} \omega_3^2}{c_0^2} A_1 A_2 e^{-i(\omega_3 t - (k_1 + k_2)z)} + c.c. \end{aligned} \quad (2.7)$$

In the case of a slowly varying amplitude  $A_3$ , one finds  $(d^2 A_3)/(dz^2) \ll 2ik_3(dA_3)/(dz)$ . We thus can neglect the term  $(d^2 A_3)/(dz^2)$ . Since  $k_3^2 = n_3^2 \omega_3^2 / c_0^2$ , the wave equation finally simplifies to

$$\frac{dA_3}{dz} = \frac{2id_{\text{eff}} \omega_3^2}{k_3 c_0^2} A_1 A_2 e^{i\Delta k z} \quad (2.8)$$

with the wave vector mismatch  $\Delta k = k_1 + k_2 - k_3$ . Equation (2.8) thus describes the spatial evolution of the third, i.e., the generated wave amplitude  $A_3$  during a frequency mixing process. It grows proportionally with the nonlinear coupling constant  $d_{\text{eff}}$  and the amplitudes of the two incident fields  $A_1$  and  $A_2$ . However, the spatial phase factor  $\exp(i\Delta k)$  determines, whether a macroscopic output beam is generated or not. This is the well-known phase matching condition for nonlinear frequency mixing processes.

The wave vector mismatch  $\Delta k$  is not necessarily zero, because it depends on the individual indices of refraction for each wavelength via  $k_i = (2\pi n_i)/\lambda_i$ , which are typically different for different wavelength. Equation (2.8) reveals that the amplitude  $A_3$  is then oscillating along the z-direction. Hence, no macroscopic output beam will built up due to destructive interference of the partial beams after  $\Delta kz > \pi$ . Additional phase matching is thus mandatory to generate efficient output, which will be described in section 2.3.

In our laser system we want to convert a pump beam with frequency  $\omega_p$  into visible output at frequency  $\omega_{\text{vis}}$ . The first frequency mixing process we use is DFG between a pump, signal and idler wave. The corresponding coupled wave equations of the three waves read similar to (2.8)

$$\begin{aligned}\frac{dA_S}{dz} &= \frac{2id_{\text{eff}}\omega_S^2}{k_S c_0^2} A_P A_I^* e^{-i\Delta kz} \\ \frac{dA_P}{dz} &= \frac{2id_{\text{eff}}\omega_P^2}{k_P c_0^2} A_I A_S e^{-i\Delta kz} \\ \frac{dA_I}{dz} &= \frac{2id_{\text{eff}}\omega_I^2}{k_I c_0^2} A_P A_S^* e^{-i\Delta kz}\end{aligned}\tag{2.9}$$

These equations describe the following situation. Once a signal beam co-propagates with the pump beam through the medium, pump photons are converted into signal and idler photons via difference-frequency generation. The generated idler photons themselves will again cause an energy transfer from the pump field to the signal field and consequently both field amplitudes will increase. This is called *optical parametric amplification* (OPA). If the medium is placed inside a cavity, which is resonant for the signal beam, every round-trip causes OPA of the signal beam which is the desired OPO process to generate a strong signal wave. Also an idler wave will built up during this process. Note that the process of amplification reverses, once a large energy fraction of the pump field was transferred to the signal and idler fields, which are now acting as pump beams themselves. In a long medium, the amplitudes of pump, signal and idler would consequently oscillate.

In the next step, the generated signal wave and the residual pump wave are frequency-mixed in single pass SFG to generate the visible output. In equation (2.8), which we derived explicitly for SFG, the relevant frequencies are then  $\omega_1 = \omega_p$ ,  $\omega_2 = \omega_s$  and  $\omega_3 = \omega_{\text{vis}}$ . The wave equations for SFG describing the spatial

amplitude evolution of all three coupled waves read

$$\begin{aligned}
 \frac{dA_{\text{vis}}}{dz} &= \frac{2id_{\text{eff}}\omega_{\text{vis}}^2}{k_{\text{vis}}c_0^2}A_{\text{p}}A_{\text{s}}e^{i\Delta kz} \\
 \frac{dA_{\text{p}}}{dz} &= \frac{2id_{\text{eff}}\omega_{\text{p}}^2}{k_{\text{p}}c_0^2}A_{\text{vis}}A_{\text{s}}^*e^{-i\Delta kz} \\
 \frac{dA_{\text{s}}}{dz} &= \frac{2id_{\text{eff}}\omega_{\text{s}}^2}{k_{\text{s}}c_0^2}A_{\text{vis}}A_{\text{p}}^*e^{-i\Delta kz}
 \end{aligned} \tag{2.10}$$

Similar to DFG, the magnitude  $A_{\text{vis}}$  of the visible electric field will increase and the pump and signal field will decrease at the same time. However, the efficiency of this process depends on the phase mismatch  $\Delta k$ .

Concluding this section, second-order frequency mixing is a way to generate a desired output wavelength from a broad spectral regime given by energy conservation. In our case, pump and signal wavelength define the SFG visible output wavelength. However, phase matching is a crucial issue for the efficiency of frequency mixing and it will be described in the next section.

## 2.3 Quasi Phase Matching

The equations (2.9) and (2.10) contain spatial phase factors which depend on the quantity  $\Delta k = k_{\text{p}} - k_{\text{s}} - k_{\text{l}}$  for the OPO and  $\Delta k = k_{\text{p}} + k_{\text{s}} - k_{\text{vis}}$  for the SFG. If  $\Delta k$  is non-zero, phase mismatch between the participating beams occurs and suppresses a macroscopic output. Figure 2.2 shows a simulation of the absolute value of  $A_{\text{vis}}$  with respect to the crystal length for different spatial phase factors and rephasing techniques. Let us first consider the two limiting cases: The black, dashed line shows the signal for perfect phase matching, i.e.,  $\Delta k = 0$ . The amplitude is linearly increasing as expected from equation (2.8). The red, solid line on the other hand shows the signal for  $\Delta k \neq 0$ , i.e., individual beams with different phase velocities. The amplitude is oscillating along the propagation direction and no output beam builds up. Hence, it is crucial to set  $\Delta k = 0$  or alternatively compensate  $\Delta k \neq 0$  by a phase matching technique. Two different options exist to satisfy this phase matching condition.

The first way of phase matching relies on equalizing the refractive indices for all corresponding beams. Thereby we adjust the phase velocities of the participating beams to be equal in the nonlinear medium. In a birefringent material, this is achieved by a specific choice of the propagation direction with respect to the optical axis. Typically this is done by varying the angle of incidence in the material and is known as critical phase matching [46].

Noncritical phase matching on the other hand relies on the temperature dependence of the refractive index. This dependence can be different for different wavelengths [46] and sometimes allows a temperature, which yields equal refractive indices for individual wavelengths. Even though both options theoretically yield  $\Delta k = 0$  and a corresponding maximum output, they have practical drawbacks. Critical phase matching often suffers from spatial walk-offs for individual

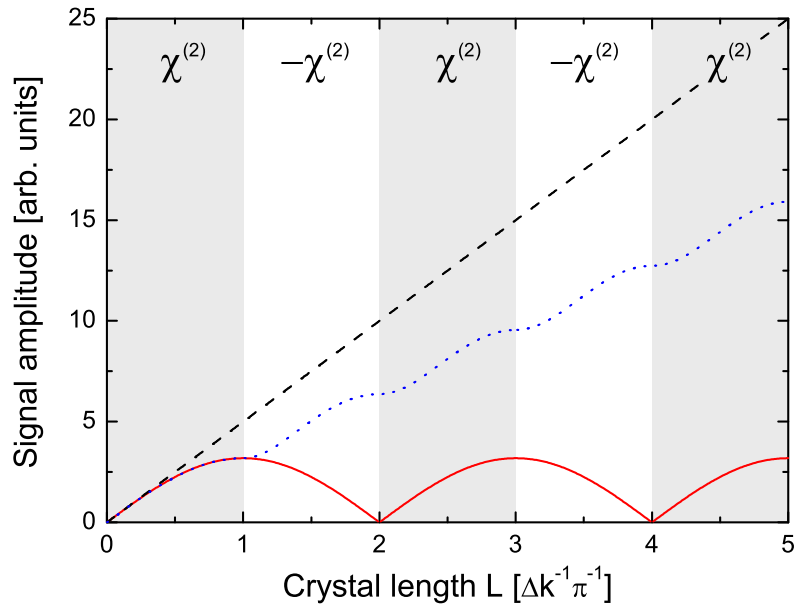


Figure 2.2: Amplitude of a desired output field generated along the crystal length for perfect phase matching (black, dashed line), non phase matched case (red, solid line) and in the case of QPM (blue, dotted line). The gray/white pattern in the graph represents periodically poled regions in a nonlinear crystal with alternating sign for the susceptibility  $\chi^{(2)}$ .

beams which reduce their interaction region. Walk-offs limit also the crystal length when the generated beams shall still overlap after the mixing process. Temperature based phase matching typically avoids the walk-off problem, but the required temperatures are often quite different from room temperature, which can challenge the setup. In addition, material related limits do not allow arbitrary high or low temperatures and thus noncritical phase matching usually covers only a limited output wavelength range.

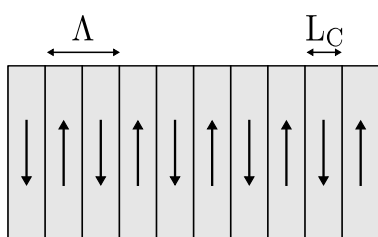


Figure 2.3: Schematic illustration of a periodically poled crystal with poling period  $\Lambda$  and coherence length  $L_C$ . All beams propagate perpendicular to the grating.

A second, alternative way to phase match nonlinear processes is quasi phase matching (QPM) [45, 46]. In QPM the phase mismatch  $\Delta k$  is allowed to be non-zero, but periodic poling of the nonlinear medium compensates this phase mismatch. QPM was actually proposed before critical and noncritical phase matching. However, periodic poling requires the manipulation of well defined regions in the crystal on a  $\mu\text{m}$  scale with high electric fields. This became technically possible only in the last three decades [47], making QPM a recent but more and more common phase matching technique. Periodic poling can be implemented in ferroelectric materials. An external voltage is used to invert one of the crystal axis in predefined regions in the crystal. Thereby, the second order susceptibility  $\chi^{(2)}$  and the nonlinear coupling constant  $d_{\text{eff}}$ , respectively, change their sign, which is known as ferroelectric domain inversion. Domains of inverted and not inverted axis are typically produced such that they periodically alternate



along the propagation direction of the beams and consequently the sign of  $d_{\text{eff}}$  changes periodically as well (see figure 2.3 and 2.2). The coherence length  $L_C$  describes the length of a single poled domain and is connected to the poling period by  $\Lambda = 2L_C$ . In order to describe the poling structure we define a corresponding poling wave vector  $k_{\text{pol}} = 2\pi/\Lambda$ . The coupling constant is then a function of the propagation z-direction

$$d(z) = d_{\text{eff}} \text{sign} [\cos(k_{\text{pol}}z)] \quad (2.11)$$

It is useful to express  $d(z)$  as a Fourier series

$$d(z) = d_{\text{eff}} \sum_{m=-\infty}^{\infty} (2/m\pi) \sin(m\pi/2) e^{ik_{\text{pol},m}z} \quad (2.12)$$

where  $k_{\text{pol},m} = 2\pi m/\Lambda$  and the whole expression is valid for the poling illustrated in figure 2.3, i.e., every poling region has the same length  $L_C$ . It is straight forward to show that the (minus) first order Fourier component is the dominant contribution to the new coupling constant with  $d_Q = (2/\pi)d_{\text{eff}}$ . Inserting the z-dependent first order coupling constant  $d_Q$  in equations (2.10) and assuming that only this particular Fourier component is dominant for the coupling, the wave equations for SFG transform into

$$\begin{aligned} \frac{dA_{\text{vis}}}{dz} &= \frac{2id_Q\omega_{\text{vis}}^2}{k_{\text{vis}}c_0^2} A_{\text{p}}A_{\text{s}} e^{i(\Delta k + k_{\text{pol}})z} \\ \frac{dA_{\text{p}}}{dz} &= \frac{2id_Q\omega_{\text{p}}^2}{k_{\text{p}}c_0^2} A_{\text{vis}}A_{\text{s}}^* e^{-i(\Delta k - k_{\text{pol}})z} \\ \frac{dA_{\text{s}}}{dz} &= \frac{2id_Q\omega_{\text{s}}^2}{k_{\text{s}}c_0^2} A_{\text{vis}}A_{\text{p}}^* e^{-i(\Delta k - k_{\text{pol}})z} \end{aligned} \quad (2.13)$$

Thus, phase matching for the visible output  $A_{\text{vis}}$  is achieved when  $\Delta k + k_{\text{pol}} = 0$ . This is the case when the phase mismatch  $\Delta kz$  after one coherence length  $L_C$  is  $\Delta kL_C = \pi$ . Then, the minus first order contribution becomes  $k_{\text{pol}} = -\pi/L_C = -\Delta k$  and the overall phase mismatch becomes 0. The coherence length, e.g., for SFG is in this case

$$L_C = \frac{\pi}{\Delta k} = \frac{\pi}{k_{\text{p}} + k_{\text{s}} - k_{\text{vis}}} = \frac{1}{2} \left( \frac{\lambda_{\text{p}}}{n_{\text{p}}} + \frac{\lambda_{\text{s}}}{n_{\text{s}}} - \frac{\lambda_{\text{vis}}}{n_{\text{vis}}} \right) \quad (2.14)$$

The blue, dotted line in figure 2.2 shows a simulation for the visible signal along the crystal position with QPM. The gray areas in the graph represent crystal regions with a reversed susceptibility in comparison to the white regions, i.e., they show the periodic poling in the crystal. Qualitatively speaking, QPM reverses the phase mismatch and thus avoids destructive interference, i.e., a phase mismatch  $\Delta kL > \pi$  for interaction length  $L > L_C$ . The amplitude can consequently increase with increasing crystal length, but with a reduced coupling coefficient by a factor of  $2/\pi$  compared to the perfectly phase matched case  $\Delta k = 0$ .

Equation (2.14) shows that the coherence length  $L_C$  defines the output wavelength via the phase matching condition. It is only a function of the vacuum wavelength as well as the temperature and wavelength dependent refractive index of the medium. The refractive index is also a function of the propagation direction through the medium in case of birefringence. The Sellmeier equation [50] is typically used to calculate the refractive index and the corresponding coherence length for periodic poling. The Sellmeier equation is an empirically derived equation and exists in slightly varying forms. These differ in terms of added temperature dependence or a higher accuracy for a certain spectral regime. An example for the Sellmeier equation with experimentally determined parameters for MgO:LN is given in [51]. For this laser system, all necessary crystal parameters for QPM were calculated using a software (*SNLO*, AS Photonics).

The advantages of QPM are the following. First, QPM allows any initial wave vector mismatch  $\Delta k$ , which is mainly defined by the corresponding refractive indices. Therefore there is no need to change the latter to achieve phase matching, i.e., no non-zero angle of incidence has to be chosen which avoids a possible beam walk-off. Thus the interaction region is extended to the entire crystal length. QPM enables a free choice of the propagation direction and the corresponding nonlinear coupling coefficients. This is probably the most beneficial point, considering that the highest couplings, which require equally polarized beams [46], cannot be addressed by critical phase matching but with QPM. Note that the coupling coefficient is reduced by a factor of  $2/\pi$  in QPM. Nevertheless, the choice of higher coupling coefficients combined with a large interaction region enables typically more efficient output compared to the use of other phase matching techniques. Disadvantages of QPM are related to the fabrication of poling structures. To date, proper poling works only for rather thin crystals with a thickness  $< 1\text{mm}$ . This leads to a small aperture of the crystal and requires beams with rather small diameters. The resulting high electric fields can cause crystal damage, strongly depending on the wavelength and intensity. The latter can become quite high when pulsed laser fields are used for frequency conversion. Some examples of damage thresholds are listed in [52].

## 2.4 Experimental Setup

This section provides an overview of the experimental realization of the OPO-SFG laser system with the specially designed nonlinear medium. It also presents a description of the frequency stabilization unit including a short introduction on Pound-Drever-Hall frequency stabilization.

### 2.4.1 Design of the Nonlinear Crystal

The previous section overviewed the concept of frequency generation by means of a pump laser driven, nonlinear medium. It also introduced the concept of quasi phase matching, which eventually enables efficient output of a desired wavelength. The nonlinear medium used in this laser system is a periodically poled

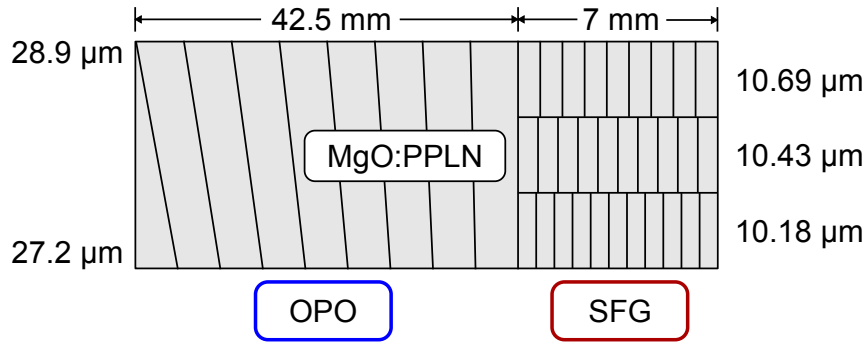


Figure 2.4: Schematic view of the magnesium oxide doped, periodically poled lithium niobate crystal (MgO:PPLN). Left and right numbers indicate the poling period for the OPO section (total length 42.5 mm) and SFG section (7 mm), respectively.

lithium niobate crystal (PPLN) with dimensions  $50 \times 12 \times 0.5$  mm [53]. Lithium niobate is a widely used synthetic crystal with relatively high nonlinear coupling coefficients (e.g.,  $d_{\text{eff}} = d_{33} = 25$  pm/V for SHG with  $\lambda_p = 1064$  nm [54]). Its transmission window ranges from about 400 nm to 5000 nm, enabling a wide range of possible output wavelength and applications (see e.g., [52]). However, the absorption coefficient increases steadily from 3%/cm to 30%/cm in the wavelength range between 3900 nm to 4400 nm.

In addition, the PPLN crystal is doped with 5% magnesium oxide (MgO) to reduce electron mobility in the crystal. In the presence of high and enduring electromagnetic fields (especially in the visible regime), electrons would otherwise leave the beam interaction zone, forming a space-charge region which changes the index of refraction. This photo refractive effect typically happens on a time scale of hours [55] and eventually leads to a performance breakdown of the laser system, because the phase matching condition is no longer fulfilled. In order to avoid unwanted reflections, the crystal's surfaces are anti-reflection coated as indicated in table 2.1).

Our crystal contains two main sections, one to phase match optical parametric oscillation and another to phase match sum-frequency generation. Figure 2.4 illustrates the corresponding crystal design.

The OPO section has a length of 42.5 mm. It exhibits a fanned poling structure, i.e., a continuously varying poling period along the crystal height, perpendicular to the propagation direction of all beams. For the OPO section the poling period changes from  $\Lambda = 27.2 \mu\text{m}$  to  $\Lambda = 28.9 \mu\text{m}$ . The fan-out structure provides

Table 2.1: Reflectivity of the PPLN crystal surfaces for the relevant spectral components.

Wavelength range [nm]	Reflectivity
604-610	$R < 1.5\%$
1380-1460	$R < 0.2\%$
1064	$R < 1\%$
3900-4600	$R < 3\%$

tunability for signal and idler output wavelengths depending on the propagation height of the pump beam through the crystal. Possible output is in the range of  $\lambda_s \approx 1386 \text{ nm}$  ( $\lambda_i \approx 4580 \text{ nm}$ ) to  $\lambda_s \approx 1463 \text{ nm}$  ( $\lambda_i \approx 3901 \text{ nm}$ ), depending on crystal height and temperature between  $40^\circ\text{C}$  and  $150^\circ\text{C}$ . Both a higher crystal temperature as well as a larger poling period increase the signal wavelength.

The second stage has a length of 7 mm and contains three tracks with different poling periods in order to phase match SFG of pump and signal radiation. Thereby, we design each track to match the signal output of the preceding OPO section. The tracks have poling periods of  $\Lambda_1 = 10.18 \mu\text{m}$ ,  $\Lambda_2 = 10.43 \mu\text{m}$  and  $\Lambda_3 = 10.69 \mu\text{m}$ , respectively. We chose three tracks instead of a fan-out structure to ensure at least some visible output in case of a calculation error for the poling periods. If a double fan-out structure would contain an incorrect poling period in one of the fans, at no crystal height the phase matching conditions of both sections would fit together. None or only little output would be the result. Thus the choice of three tracks corrects for possible errors. In combination with temperature tuning and the broad bandwidth of QPM of the order of 100 GHz, our design still permits tuning of the visible output. The predicted output wavelength from the SFG stage are wavelengths between  $\lambda_{\text{vis}} \approx 601 \text{ nm}$  and  $\lambda_{\text{vis}} \approx 616 \text{ nm}$ . However, we note that these are theoretical values. Crystal absorption especially above 4000 nm as well as a limited temperature control to a range between  $25^\circ\text{C}$  and  $70^\circ\text{C}$  reduce the range of possible output wavelength. The experimental results on the tuning range are shown and discussed in section 2.5.2.

In order to generate output at a wavelength of  $\lambda_{\text{vis}} = 606 \text{ nm}$  for our specific experiments in PrYSO, we use SFG track no. 2. At this crystal height, the OPO section generates a signal wave at  $\lambda_s = 1407 \text{ nm}$ . Pump wave and signal wave mix to  $\lambda_{\text{vis}} = 606 \text{ nm}$  in the SFG track when the crystal temperature is  $T_C \approx 30^\circ\text{C}$ .

Note that we chose the OPO section to precede the SFG section. However, previous work about the stage order suggests enhanced output stability with a reversed order of OPO and SFG stages [22, 56]. The laser system nevertheless shows good and stable output performance (see the experimental results in section 2.5). Thus we decided not to change the setup and leave this as a subject of future work.

## 2.4.2 The OPO-SFG Setup

The experimental setup of the OPO-SFG is based on a commercially available cw-OPO (Lockheed Martin Aculight, Argos Model 2400 SF-15). In our approach we replace the original crystal designed for output in the mid-infrared region with our OPO-SFG crystal. In addition we expand the system with a frequency stabilization unit. Figure 2.5 shows the schematic setup including all relevant components of our laser system. We consider first the upper dashed box, describing the OPO-SFG setup. We use an all-solid-state fiber-laser system to provide the required pump radiation at  $\lambda_p = 1064 \text{ nm}$ . It consists of a seed fiber laser (NKT Photonics, Koheras AdjustiK Y10) and a fiber amplifier (IPG, YAR-15K-LP-SF) providing radiation with a maximum output power of  $P_p = 16 \text{ W}$ . The amplified output radiation has a nominal frequency noise of  $\Delta\nu_p < 100 \text{ kHz}$  on a timescale of 50 ms. The seed fiber

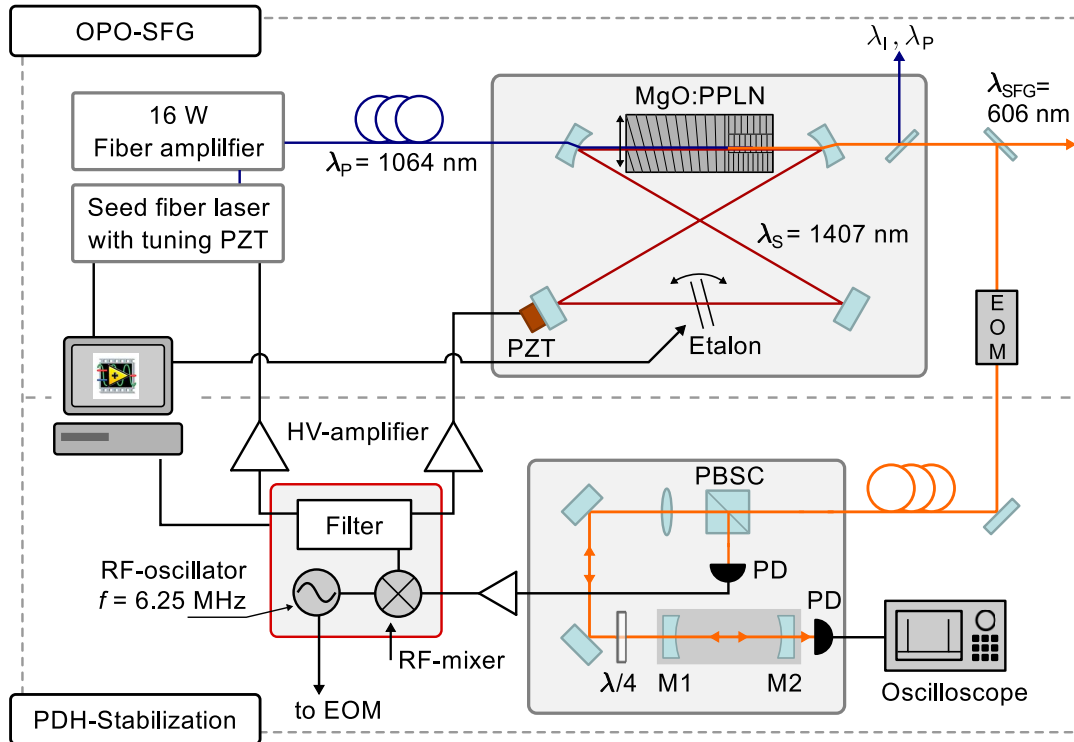


Figure 2.5: (Upper dashed box) Schematic setup of the OPO-SFG laser system. (Lower dashed box) Schematic setup of the Pound-Drever-Hall frequency stabilization. PZT are piezo-electric transducers, EOM is an electro-optic modulator, M1 and M2 are mirrors with a reflectivity of  $R = 99.9\%$  for 606 nm, RF stands for radio frequency, HV for high voltage, PD are photodiodes, PBSC a polarizing beam splitter cube. Black lines are electronic connections, colored lines represent laser light.

laser contains a piezo electric transducer (PZT) allowing for continuous pump wavelength tuning in the range of 100 GHz.

A polarization maintaining fiber guides the linearly polarized pump radiation to the OPO-SFG crystal. The latter is embedded in a bow-tie ring cavity consisting of two curved mirrors with radii of curvature  $r = 100 \text{ mm}$  and two planar mirrors. The curved mirrors focus the pump beam to a  $1/e^2$  diameter  $d = 130 \mu\text{m}$  in the center of the crystal. The optical cavity is singly resonant for the signal beam of the OPO process and has a free spectral range of  $\Delta\nu_{\text{FSR}} = 750 \text{ MHz}$ . The mirror reflectivities are  $R_s \approx 99.9\%$  for the signal beam and  $R_{I,P} < 5\%$  for the idler and pump beams. Note that the mirrors are not anti-reflection coated for the visible output. This causes power loss for the SFG output in the range of 20 – 30%.

The crystal is placed inside an oven that permits adjustment of the crystal's temperature between surrounding temperature and  $70^\circ\text{C}$  via heating. A single adjustment screw allows to alter the crystal position inside the cavity as indicated by the arrow in figure 2.5. This allows to change the pump beam position within the crystal and the poling period for QPM, respectively.

The optical cavity is made of a monolithic block with the mirrors attached to it. In order to stabilize the temperature of the cavity block, we use a Peltier element driven with a current of  $\pm 5 \text{ A}$  for cooling or heating. The temperature stability

is around  $0.01^{\circ}\text{C}$  when using a  $10\text{ k}\Omega$  semi-conductor temperature sensor and a commercially available temperature controller (Wavelength Electronics, PTC5K-CH 5A). An additional  $250\text{ }\mu\text{m}$  thick, fused silica low finesse etalon with a free spectral range of  $400\text{ GHz}$  prevents longitudinal multi-mode operation of the cavity. The tilt angle of the etalon ( $-4^{\circ}$  to  $4^{\circ}$ ) selects the desired output mode of the signal beam. One of the planar mirrors is mounted on a PZT (Physik Instrumente, P-010.00H). This allows fine tuning the cavity's resonance frequency in a range of some  $100\text{ MHz}$ . A pair of dichroic mirrors separates the output beams after the cavity, i.e., pump, signal, idler from the visible output. A single mode fiber finally guides the visible SFG output to the experiment. A small fraction of the visible SFG output serves to monitor the laser power and wavelength. A Pound-Drever-Hall frequency stabilization uses another fraction of the visible output to frequency stabilize the SFG output frequency (see figure 2.5 lower dashed box and explanations in section 2.4.3). An external Fabry Perot resonator (Sirah, Eagle Eye) serves to measure the laser frequency linewidth on a timescale of  $100\text{ ms}$  during laser operation.

All monitored data is stored on a computer. The latter also provides control over all components of the laser system except the PZTs in the seed laser and the OPO cavity. In addition, a home-made program on the computer allows for automatic turn-on and turn-off of the laser system for a manually preset output wavelength. This degree of automation provides an easy to use laser system, even to an unexperienced user, once the laser system has been set up and adjusted according to all requirements.

### 2.4.3 Pound-Drever-Hall Frequency Stabilization

The frequency deviation of the visible output on the relevant time scale for our experiments ( $\sim 100\text{ ms}$ ) should be as small as possible and at a maximum of the order of  $\Delta\nu = 100\text{ kHz}$ . We thus extend the laser system with a Pound-Drever-Hall (PDH) frequency stabilization [57]. This stabilization technique yields an error signal which is almost insensitive to power fluctuations. Furthermore, it provides a strong and fast response to phase and frequency fluctuations. This chapter gives description of the experimental implementation (see figure 2.5, lower dashed box) as well as a brief introduction into PDH stabilization [58].

The standard approach for frequency stabilization is to compare the actual laser frequency to a reference. The deviation from the latter serves to correct the laser frequency accordingly. Thus, frequency stabilization necessarily contains two parts. The first one is a reference and the second is a method to translate the frequency deviation into an error signal used for frequency correction. A reference frequency may be, e.g., a delayed fraction of the laser beam itself, i.e., a memory of the laser beam's frequency of a former time. However, delaying a laser beam is typically limited to short timescales in the  $\mu\text{s}$  range and drifts on longer timescales are hard to compensate. Thus it is more common to use an absolute frequency reference such as an atomic transition or an optical cavity. The latter is used in this setup. The PDH reference cavity is embedded in the stabilization

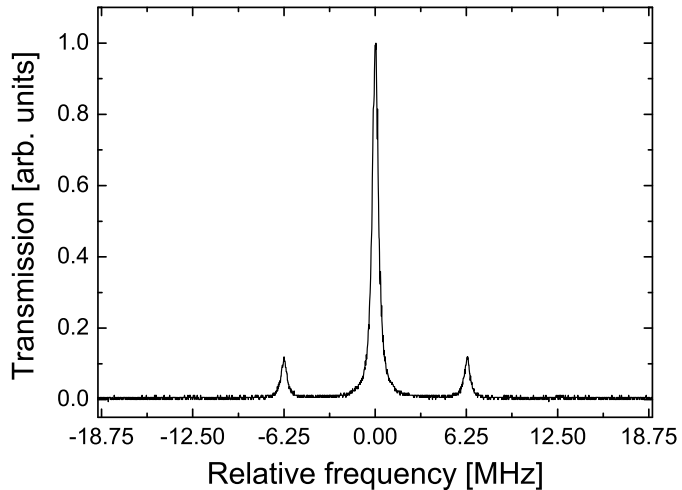


Figure 2.6: Frequency dependent transmission through the PDH cavity for a phase modulated laser beam. The two sidebands are frequency shifted by the phase modulation frequency, i.e., 6.25 MHz from the carrier frequency.

unit as depicted in figure 2.5 (gray part in the lower dashed box). Our cavity is a Fabry-Perot cavity, consisting of two mirrors M1 and M2 with equal reflectivity  $r$  for the electric field (or  $R = r^2$  for the reflected power), and a free spectral range of  $\Delta\nu_{\text{FSR}} = c/2L$ , where  $L$  is the cavity length.

A fraction of the SFG output is guided through an electro-optical phase modulator (EOM) driven with a frequency of  $\omega_{\text{EOM}} = 2\pi \times 6.25$  MHz. A locking unit (Toptica, Digilock 110) generates the modulation frequency in combination with an amplifier (Minicircuits, ZHL-3A). Note that the EOM is included in an LC resonance circuit for the modulation frequency. The EOM modulates the phase of the incident laser field  $E_{\text{inc}}$  with angular frequency  $\omega_L$ , which becomes

$$\begin{aligned} E_{\text{inc}}(t) &= E_0 e^{-i(\omega_L t + \beta \sin(\omega_{\text{EOM}} t))} \\ &\approx E_0 \left( J_0(\beta) e^{-i\omega_L t} + J_1(\beta) e^{-i(\omega_L + \omega_{\text{EOM}})t} - J_1(\beta) e^{-i(\omega_L - \omega_{\text{EOM}})t} \right) \end{aligned} \quad (2.15)$$

Here,  $\beta$  is the modulation depth, i.e., the amplitude of phase modulation, and  $J_0$  and  $J_1$  are the zero and first order Bessel functions. The phase modulation of the laser field causes the appearance of side bands with frequencies  $\omega_L \pm \omega_{\text{EOM}}$ . Figure 2.6 shows the transmission through the PDH cavity when the frequency of the laser is scanned. The phase modulated laser beam consists of a carrier frequency in the center and two side bands symmetrically shifted from the carrier by  $\omega_{\text{EOM}}/2\pi$ , the phase modulation frequency. A single mode fiber guides the modulated beam to the stabilization unit. After the fiber, the beam has a spatial Gaussian beam profile. In combination with a lens, this enables efficient coupling the  $\text{TEM}_{00}$  Gaussian mode of the PDH cavity. Figure 2.7 shows a full FSR of the reference cavity, where only the  $\text{TEM}_{00}$  mode is observable, indicating a very good coupling to the cavity.

PDH stabilization uses the reflected beam of the cavity. It consists of two parts, the promptly reflected beam  $E_{\text{pr}}$ , and the cavity's leakage beam  $E_{\text{leak}}$ . For a single

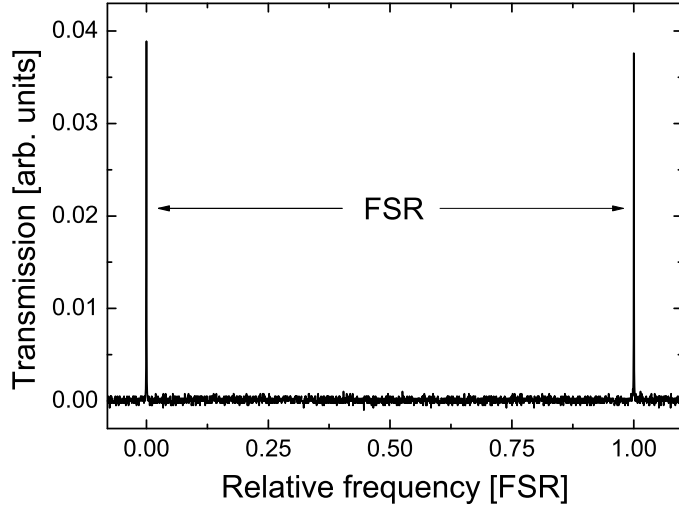


Figure 2.7: Frequency dependent transmission of the OPO-SFG output through the PDH reference cavity. The spectral distance of both transmission maxima corresponds to the free spectral range (FSR) of the cavity.

frequency component, the reflected beam reads

$$\begin{aligned}
 E_{\text{refl}}(k) &= E_{\text{pr}}(k) - E_{\text{leak}}(k) = E_0 r e^{-i\omega_L t} - E_0 e^{-i(\omega_L t - 2kL)} (1 - r^2) r \sum_{m=0}^{\infty} (r^2 e^{2ikL})^m \\
 &= E_0 \frac{r - (1 - r^2) r e^{2ikL}}{1 - r^2 e^{2ikL}} e^{-i\omega_L t} = E_0 \frac{r (e^{2ikL} - 1)}{1 - r^2 e^{2ikL}} e^{-i\omega_L t}
 \end{aligned} \tag{2.16}$$

Note that the reflection on the first cavity mirror causes a  $\pi$  phase shift for the promptly reflected beam (indicated by the minus sign between the two fields). When  $kL$  is replaced by  $\omega/(2\Delta\nu_{\text{FSR}})$ , one obtains the Airy function for the reflected beam of a Fabry-Perot cavity

$$F(\omega_L) \equiv \frac{E_{\text{refl}}}{E_{\text{inc}}} = \frac{r (e^{i\omega_L/\Delta\nu_{\text{FSR}}} - 1)}{1 - r^2 e^{i\omega_L/\Delta\nu_{\text{FSR}}}} \tag{2.17}$$

In the experimental setup, a quarter-wave plate and a polarizing beam splitter cube (PBSC) separate the incident and the reflected beam. A photodiode (electronic workshop TU Darmstadt, bandwidth  $\sim 1$  GHz) detects the power  $P_{\text{refl}}$  of the reflected beam as indicated in figure 2.8. The detected signal reads

$$\begin{aligned}
 P_{\text{refl}} &= |E_{\text{refl}}|^2 = P_C |F(\omega_L)|^2 + P_S (|F(\omega_L + \omega_{\text{EOM}})|^2 + |F(\omega_L - \omega_{\text{EOM}})|^2) \\
 &\quad + 2\sqrt{P_C P_S} \left( \right. \\
 &\quad \quad \mathbf{Re} [F(\omega_L) F^*(\omega_L + \omega_{\text{EOM}}) - F^*(\omega_L) F(\omega_L - \omega_{\text{EOM}})] \mathbf{cos}(\omega_{\text{EOM}} t) \\
 &\quad \quad \left. + \mathbf{Im} [F(\omega_L) F^*(\omega_L + \omega_{\text{EOM}}) - F^*(\omega_L) F(\omega_L - \omega_{\text{EOM}})] \mathbf{sin}(\omega_{\text{EOM}} t) \right) \\
 &\quad + \text{higher frequency terms}
 \end{aligned} \tag{2.18}$$

The first two summands in equation (2.18) represent the total power in the carrier and the sidebands, respectively. In case of weak sideband modulation, they are



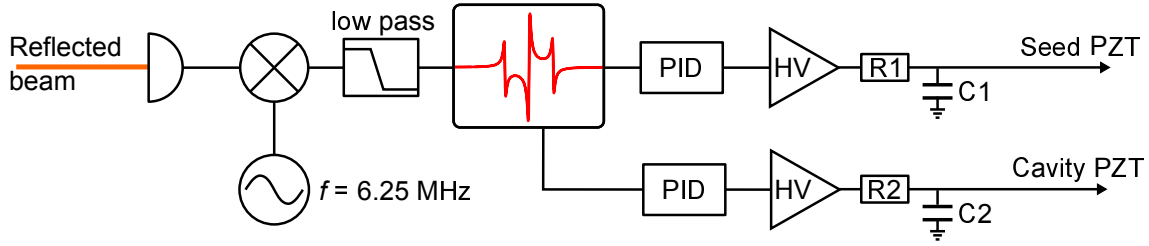


Figure 2.8: Schematic setup of the locking loop. A photodiode detects the reflected beam. The electronic signal is processed by an electronic mixer and a low pass. The obtained error signal is sent to each PZT in the laser system via a PID controller, a high voltage (HV) PZT driver and an additional low pass filter. C are capacitors, R are resistors with values  $C_1 = 5.1 \text{ nF}$ ,  $R_1 = 3.1 \Omega$ ,  $C_2 = 33 \text{ nF}$ ,  $R_2 = 4.8 \Omega$ .

approximately given by  $P_C = J_0^2 P_0$  and  $P_S = J_1^2 P_0$ , with the total initial beam power of  $P_0$ . These waves oscillate too fast to detect them on a photodiode, thus they appear constant in the above equation. The next two summands oscillate with the phase modulation frequency  $\omega_{\text{EOM}}$  which arises from the interference between carrier and sidebands. An electronic mixer (Toptica, Digilock 110) demodulates the detected signal with a local oscillator frequency  $\omega_{\text{LO}} = \omega_{\text{EOM}}$  and an adjustable relative phase  $\phi_{\text{LO}}$ . Since the two frequencies are equal, the demodulated signal has a constant term as well as a term oscillating with  $2\omega_{\text{EOM}}$ . After a low pass filter, only the constant terms contribute to the signal which consists of two parts

$$\begin{aligned}
 (1) : & 2\sqrt{P_C P_S} \text{Re} [F(\omega_L)F^*(\omega_L + \omega_{\text{EOM}}) - F^*(\omega_L)F(\omega_L - \omega_{\text{EOM}})] \cos(\phi_{\text{LO}}) \\
 (2) : & 2\sqrt{P_C P_S} \text{Im} [F(\omega_L)F^*(\omega_L + \omega_{\text{EOM}}) - F^*(\omega_L)F(\omega_L - \omega_{\text{EOM}})] \sin(\phi_{\text{LO}})
 \end{aligned} \tag{2.19}$$

Equation (2.19)-(2) represents the PDH error signal. The choice of the relative phase  $\phi_{\text{LO}}$  selects the corresponding part via the cosine and sine term. The error signal is of the form shown in figure 2.9. Note that we obtain this error signal, if the modulation frequency is larger than the cavity transmission width, i.e., in case of fast modulation. Figure 2.9 shows both experimental data and a simulation of the above given equation (2.19)-(2). The simulation only includes the mirror reflectivity  $r$  (defining also the Airy function  $F$ ) of our cavity. The good agreement between experimental data and simulation indicates that our cavity is well aligned and no additional losses occur. Thus solely the mirror reflectivity defines the cavity finesse. The PDH error signal exhibits a strong response, i.e., a steep slope near cavity resonance. This region is called the tight-locking region and allows for fast corrections to small phase or frequency deviations. The error signal close to the cavity resonance is in good approximation linearly dependent on the inverse reference cavity linewidth  $\Delta\nu_{\text{Cav}}^{-1}$  [58], which is defined by means of the finesse  $\mathcal{F}$  with

$$\Delta\nu_{\text{Cav}} = \Delta\nu_{\text{FSR}}/\mathcal{F} \quad \text{with} \quad \mathcal{F} = \frac{\pi r}{1 - r^2}. \tag{2.20}$$

Hence, we find a steeper tight-locking slope with higher cavity finesse. In other words, the cavity linewidth defines the width of the tight-locking region. Ideally,

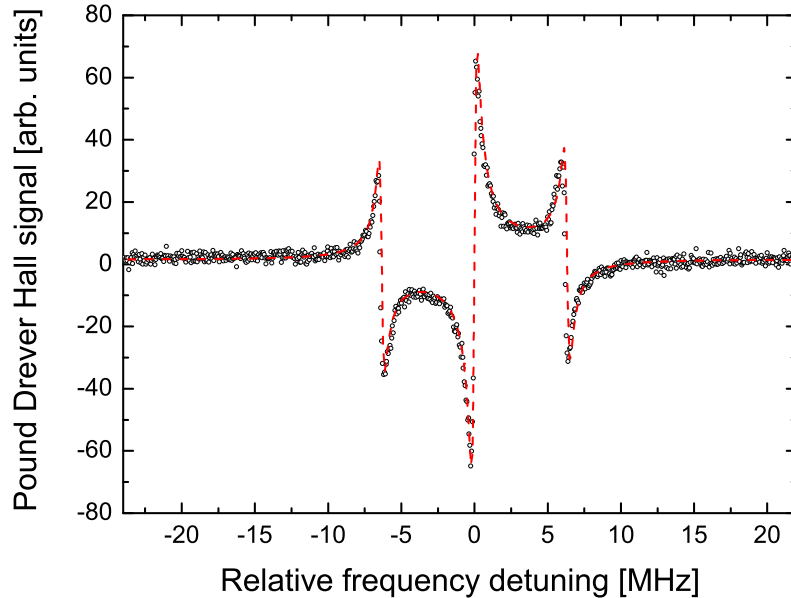


Figure 2.9: Pound-Drever-Hall error signal generated with the setup described in section 2.4.3 vs. relative frequency detuning (black, hollow circles). The zero frequency corresponds to the cavity resonance. The red, dashed line shows a simulation of the error signal for our specific cavity configuration.

the laser frequency is kept within the tight-locking region all the time. Consequently, the finesse of the cavity sets a theoretical minimum for frequency deviations, i.e., the possible quality of the frequency lock. However, the PDH error signal consists not only of the tight-locking region. The overall correction bandwidth for frequency deviations beyond the latter is given by twice the modulation frequency. Once the laser frequency moves out of the tight-locking region but within the correction bandwidth, it is automatically guided back to the latter.

Drever and Hall et al. give a qualitative idea on how this error correction works [57]. The beam inside the cavity acts as a phase memory. The cavity resonance on the other hand serves as a frequency reference. The phase memory lasts for a time given by the cavity life-time which is defined by the finesse. On resonance, the leakage (memory) beam and the promptly reflected beam (containing the actual laser frequency and phase information) interfere destructively to a minimum value for the totally reflected beam as given in equation (2.16). If a sudden phase change occurs, the cavity will not immediately respond, as the intra-cavity beam still possesses the old phase of the laser radiation. Hence, the interference changes and the error signal changes its value from zero to a non-zero correction value. If the phase fluctuations are small or there is a drift in the laser frequency, the cavity follows this change only within its linewidth  $\Delta\nu_{\text{Cav}}$  and thus acts as a frequency reference.

### Locking Loop

The next step in frequency stabilization is to feed back the error signal to the available frequency controls in the laser. In our case these are the PZTs inside

the seed fiber laser and in the optical OPO cavity. Figure 2.8 schematically shows our complete locking loop and section 2.5.4 shows experimental data describing the loop characteristics. After the generation of a PDH error signal, appropriate filtering and amplification of the error signal is necessary to avoid unstable locking or a too weak response. Unstable locking is typically related to resonances within the locking loop. Here, PZT resonances cause an exclusively large gain at certain frequencies which leads to an extreme oscillatory response of the locking loop and eventually prohibits stable laser operation. In our setup, we use a commercially available locking unit to generate the modulation frequency, the local oscillator frequency and a low pass filter to generate the error signal. We use the internal proportional-integral-differential (PID) controller of the locking unit to process the error signal such that it shows minimum deviations from zero during the laser operation, i.e., the laser frequency is locked in the tight locking region. However, PZTs are capacitors from the electronic point of view. In combination with their corresponding high voltage (HV) PZT drivers (represented by the triangles labeled HV in figure 2.8) they form oscillator circuits. These have resonance frequencies of 3.8 kHz, 24.5 kHz and 67 kHz for the seed PZT and 13.5 kHz for the OPO cavity PZT (see also section 2.5.4). We observe these resonances even in case of an open locking loop, thus they cannot be suppressed with the PID controller in the locking unit. For this reason we put additional low-pass filters after each PZT driver to suppress the residual resonances. The low-passes have nominal cut-off frequencies of  $f_{LP} = 3.1$  kHz (seed PZT) and  $f_{LP} = 4.8$  kHz (OPO cavity PZT). Section 2.5.4 provides a detailed analysis of the spectral response of our locking loop.

### Reference Cavity

This paragraph gives a short overview of our reference cavity, which is based on a Fabry-Perot resonator with parameters as indicated in table 2.2. The cavity consists of two plano-concave mirrors, with a high reflectivity for the visible SFG output wavelength on the curved side. The two mirrors are mounted on a spacer made from ultra-low expansion (ULE) glass (JapanCell, Clearceram Z-HS). This reduces thermal expansion of the cavity length and minimizes long-term, temperature dependent laser frequency drifts. Figure 2.10 shows a 3D image of the cavity and its enclosure. The cavity is housed inside a gilded copper box, which itself is mounted

Table 2.2: Relevant parameters of the reference cavity.

Cavity length	$l = 145$ mm
Mirror radius of curvature	$-1000$ mm
Mirror reflectivity ( $\lambda = 606$ nm)	$R = r^2 = 99.9\%$ on curved side
Free spectral range	$\Delta\nu_{FSR} = 1033$ MHz
Cavity transmission linewidth	$\Delta\nu_{Cav} = 330$ kHz
Finesse	$\mathcal{F} = 3140$
$1/e^2$ beam waist on mirrors	$w_0 = 232$ $\mu$ m
$1/e^2$ beam waist in the cavity center	$w_0 = 223$ $\mu$ m

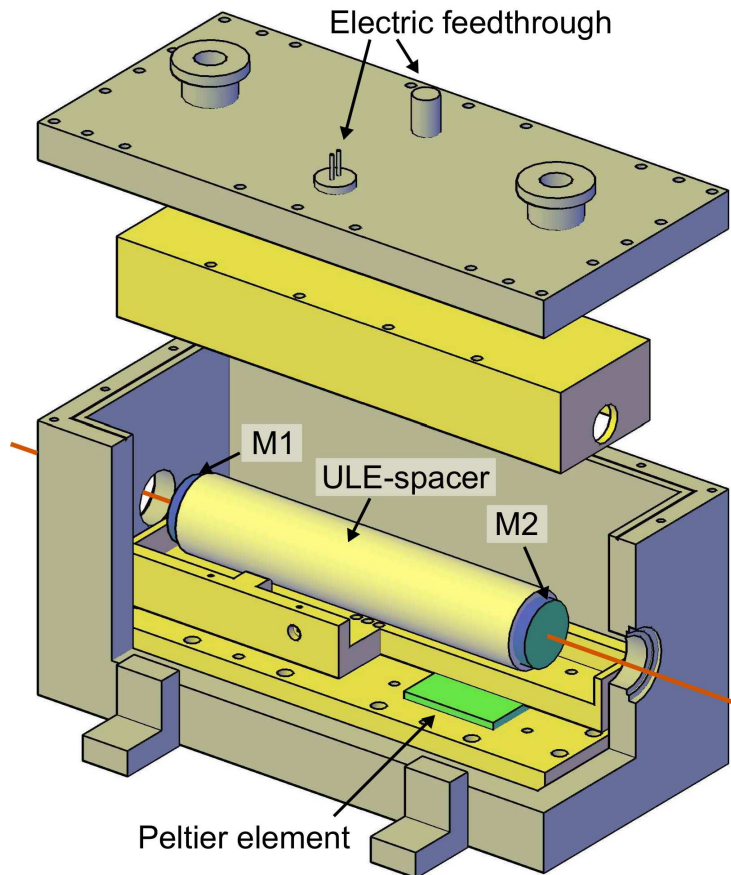


Figure 2.10: Pound-Drever-Hall reference cavity with mirrors M1 and M2 mounted on an ultra-low expansion (ULE) glass spacer, housed in a vacuum chamber (gray). The orange lines indicate the laser beam. Yellow parts show gilded copper parts used to mount the reference cavity. Two Peltier elements (only one is shown) provide temperature control of the reference cavity.

on two Peltier elements (PE). The PEs are driven with a  $\pm 5$  A current from a temperature control unit (Wavelength Electronics, PTC5K-CH 5A) and serve to stabilize the temperature of the cavity enclosure and consequently the cavity itself to  $T \approx 23 \pm 0.01^\circ\text{C}$ . Note that Clearceram Z-HS has a nonlinear coefficient of thermal expansion, which exhibits zero first order temperature dependence at this specific temperature. A closable aluminum chamber with an optical access to the cavity and electric feed-throughs for temperature control surrounds all mentioned parts. It also enables a vacuum with a pressure of  $p \approx 10^{-3}$  mbar. Thus the housing shields the reference cavity from air pressure fluctuations as well as environmental temperature fluctuations. In addition, the whole PDH setup (except from the EOM) is placed on a solid aluminum plate, which is mounted on a rubber carpet for vibrational isolation. The setup thus provides a stable, relatively high finesse reference cavity for the PDH stabilization.

## 2.5 Experimental Results

The following section presents an experimental characterization of the OPO-SFG laser system operation. It starts with an overview on the free-running system and then summarizes the most important aspects about the frequency stabilized laser operation.

### 2.5.1 Operation at 606 nm

The experiments in PrYSO require laser radiation at  $\lambda_{\text{vis}} = 605,98 \text{ nm}$  and the OPO-SFG laser system was mainly designed to work for this specific wavelength. The OPO-SFG provides stable, single longitudinal mode output with a maximum output power of  $P_{\text{vis}} = 1.3 \text{ W}$  at a pump power of  $P_{\text{p}} = 11.3 \text{ W}$ . To the best of our knowledge, this is the highest up to date output power for experiments in PrYSO from an all solid-state-laser source. Note that this is also the best possible result we obtained with our laser system for this very specific wavelength.

In this case, the pump depletion is around 50% and the pump power threshold for visible output is  $P_{\text{p}} = 8 \text{ W}$ . This rather high value originates from idler absorption in the crystal ( $\sim 30\%/ \text{cm}$ ). Furthermore, the SFG stage acts as an additional loss mechanism for the signal beam. In combination, both effects suppress efficient OPO below this high threshold pump power. However we do not require such a high amount of visible power and operate the OPO-SFG with an average output power of  $P_{\text{vis}} \sim 1.1 \text{ W}$  at a pump power of  $P_{\text{p}} = 11.7 \text{ W}$ . This mode of operation is easy to realign if necessary and has proved to be stable on ultra-long time scales as shown in section 2.5.3. Easy realignment includes rather soft constraints for the pump beam propagation height through the crystal, temperature and etalon angle in order to obtain this desired output mode. Specifically, we run the OPO-SFG system at a crystal temperature of  $T = 32.4^\circ \text{C}$ , i.e., at almost room temperature, with an etalon angle of around  $0^\circ$ .

Note that the OPO process and the SFG both take place inside the optical cavity. The SFG is a single-pass process, but benefits from the high intra-cavity signal power. The signal beam leakage through one of the optical cavity mirrors ( $R_{\text{S}} = 99.9\%$ ) is  $\approx 1 \text{ mW}$ , yielding  $P_{\text{S}} \sim 1 \text{ W}$  intra-cavity signal power. Figure 2.11 shows the monitored SFG output power on the timescale of one second. From the data we deduce a relative *root-mean-square* (rms) noise value of  $\Delta P_{\text{rms}}/P < 1\%$  and a typical peak to peak deviation of  $\Delta P_{\text{pp}}/P < 10\%$ .

The frequency linewidth of the free-running laser system measured on a time scale of 100 ms ranges between  $100 \text{ kHz} < \Delta\nu \ll 1 \text{ MHz}$ . Although this is already a relatively good result, which proves robust and stable operation of our laser system, light storage experiments in PrYSO require constant narrow frequency linewidth in the range of  $\sim 100 \text{ kHz}$ . Therefore, additional stabilization is necessary, which is shown and discussed in section 2.5.4.

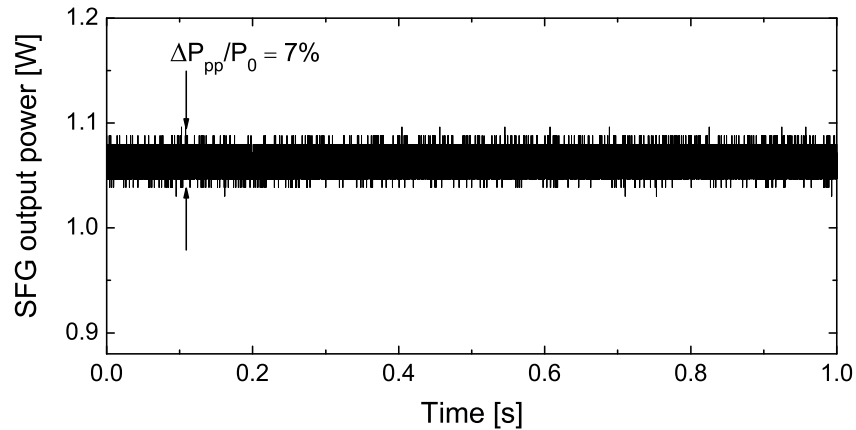


Figure 2.11: SFG output power, recorded during the time of one second in order to determine power deviations on short timescales.  $\Delta P_{pp}$  is the peak to peak deviation,  $P_0$  is the average power in the measurement. The data were recorded with a sampling rate of 100 kHz.

## 2.5.2 Tuning the SFG Output Wavelength

The optical transition in the Pr ions is inhomogeneously broadened (see chapter 1.5). In order to cover the full linewidth, it is crucial to tune the visible output from the OPO-SFG laser system. The OPO-SFG offers a variety of tuning mechanisms for coarse, intermediate and fine tuning of the output wavelength in the visible regime.

Coarse tuning is achieved by choosing a pump beam propagation height through the crystal (see figure 2.5). Thereby, we define the phase matching condition for the signal beam in the OPO process and the visible output in the SFG process. However, the QPM bandwidth is quite large and of the order of a few 100 GHz. This might cause longitudinal multi-mode operation in the OPO process, as the optical OPO cavity has a free spectral range of only 750 MHz. The additional low-finesse etalon in the OPO cavity selects one of the frequency modes of the OPO cavity. The etalon tilt angle thus enables intermediate tuning within the QPM bandwidth. Once the etalon is set, the PZT mounted mirror in the OPO cavity provides additional, continuous fine tuning of the signal wavelength in a range of a few 100 MHz within the transmission peak of the low finesse etalon. The latter two mechanisms affect only the signal wavelength, which is converted directly to the visible output in the SFG track. In addition, the OPO-SFG system enables also direct tuning of the visible output without changing the OPO cavity. The seed fiber laser contains a PZT attached to its fiber that enables fine tuning of the pump wavelength in the range of 100 GHz. The pump wavelength does not change the signal wave, if the OPO cavity is kept with fixed parameters (the unused idler wavelength compensates the pump frequency change). However, in the SFG stage of the crystal, the visible wavelength does change with the pump wavelength. Tuning the pump wave is thus a direct way to tune the SFG output. It is actually the preferred tuning mechanism, once the laser system is set to a certain OPO cavity configuration.

Figure 2.12 shows experimental data on the tuning performance of our laser

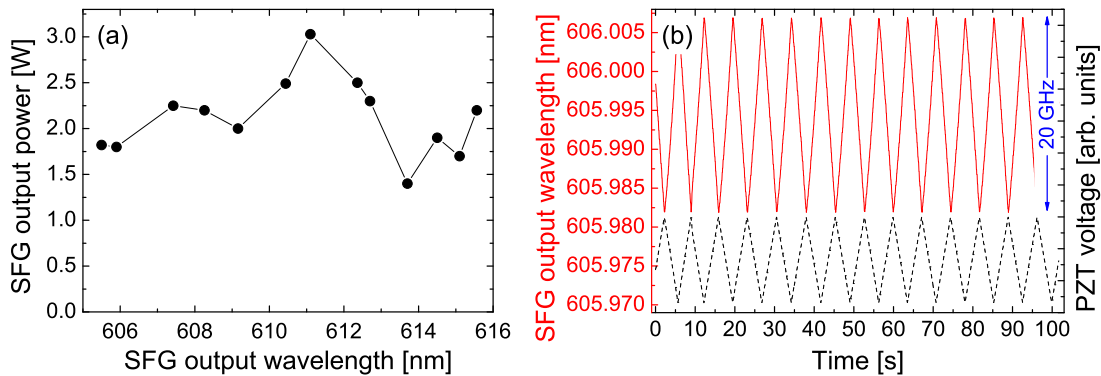


Figure 2.12: (a) SFG output power for different SFG output wavelength at  $P_p = 15$  W pump power. (b) Variation of the SFG output wavelength (red, solid, line) with temporal variation of the seed fiber laser PZT voltage (black, dashed line).

system. Graph (a) shows the SFG output power when we tune the SFG output wavelength within the maximum possible range. For each data point, we optimized the crystal temperature, beam propagation height through the crystal, as well as the etalon angle and the PZT voltages to maximize the output power. The pump power was always  $P_p = 15$  W. The measurement shows a broad spectrum of possible output wavelength from  $\lambda_{\text{vis}} = 605$  nm to  $\lambda_{\text{vis}} = 616$  nm. The output power is well above 1 W for all wavelengths. Note that the possible wavelength range is slightly smaller than expected due to idler absorption and the limited temperature control range as discussed in section 2.4.1. Additionally, the output power varies depending on the SFG output wavelength. The main reason is the significant idler absorption above 4000 nm. This causes thermal lensing and dephasing, reducing the OPO and SFG efficiency [59]. In addition, the crystal shows enhanced OH-absorption at a signal wavelength of  $\lambda_s \approx 1450$  nm. Another reason for the observed oscillations is the heterogeneous QPM acceptance bandwidth due to the three discrete SFG poling periods. A fan-out structure would yield a more homogeneous acceptance profile and consequently lower oscillations in output power.

Finally, the mirrors of the OPO cavity are not anti-reflection coated for the visible output. Therefore, they cause power losses as well as a weak etalon effect inside the OPO cavity. All these factors cause oscillations of the output efficiency, even though the performance of the laser system is still very high in terms of tuning range and cw SFG output power. The visible output has a spatial  $\text{TEM}_{00}$  profile with an  $M^2$  of 1.05 in x-direction and 1.10 in y-direction (measured with a beam profiler for a wavelength of 611 nm).

Graph (b) in figure 2.12 shows the SFG output wavelength during a temporal variation of the seed PZT voltage. The seed PZT causes a change of the pump and SFG wavelength, respectively. The SFG output wavelength clearly follows the modulation applied to the PZT in a continuous tuning range of  $\Delta\nu = 20$  GHz. This is already sufficient to cover the inhomogeneous linewidth in PrYSO of about 7 GHz.

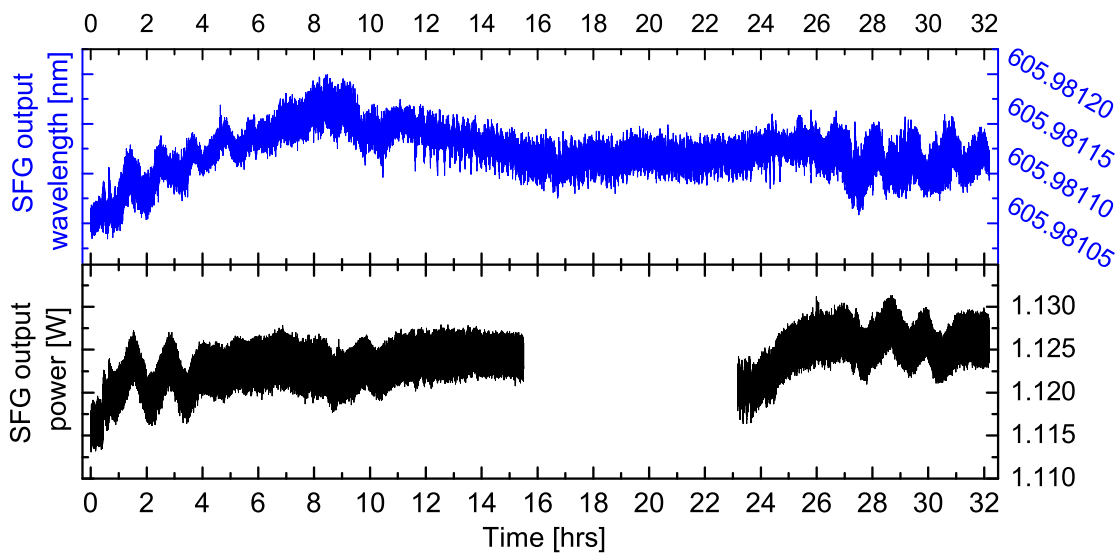


Figure 2.13: (Upper, blue graph) SFG output wavelength and (lower, black graph) SFG output power, monitored over the period of more than a day. The missing data in the power measurement between hour 16 and hour 23 are due to an interrupted computer - analog/digital converter connection. The wavelength recording is not affected.

### 2.5.3 Long-Term Operation

In order to investigate the long-term behaviour of our laser system we perform a measurement of SFG output power and wavelength over the period of multiple hours. Figure 2.13 shows the result of this measurement. Both quantities stay without instabilities for more than 30 hours. Note that the missing data for the output power are due to an interrupted connection between the computer and the analog to digital converter for the power detecting photodiode. During the whole measurement, the laser system was frequency stabilized with the PDH stabilization. It provided a wavelength of  $\lambda_{\text{vis}} = 605.981 \text{ nm}$  with an average power of  $P_{\text{vis}} = 1.12 \text{ W}$  at a pump power  $P_p = 11.7 \text{ W}$ , i.e., the OPO-SFG was set to a standard configuration used for experiments in PrYSO. From the long-term graph, we extract a maximum peak to peak wavelength deviation of  $\Delta\lambda_{\text{vis}} = 0.15 \text{ pm}$ , which corresponds to a frequency deviation of  $\Delta\nu_{\text{vis}} \approx 120 \text{ MHz}$ . The long-term (rms) power deviation was  $\Delta P_{\text{vis}}/P_{\text{vis}} < 2\%$  for 30 hours. As the laser system was stabilized all the time, the wavelength deviation originates from a slow deviation of the reference cavity length in the PDH stabilization due to temperature fluctuations. However, ULE has a maximum coefficient of thermal expansion of  $0.2 \cdot 10^{-7}/^\circ\text{C}$ . The measured wavelength deviation would thus correspond to a temperature drift of  $\sim 12^\circ\text{C}$ . On the other hand, the cavity mirrors exhibit a larger coefficient of thermal expansion ( $\sim 0.5 \cdot 10^{-6}/^\circ\text{C}$ ). If we neglect induced mechanical stress due to the different thermal expansion of ULE and the mirror substrate (NBK-7) and a corresponding change of the cavity length, the wavelength deviation corresponds to a temperature drift of roughly  $0.5^\circ\text{C}$ . This is most likely the case, because the temperature controller itself is not temperature stabilized. This results in a slightly worse temperature control accuracy, which is responsible for this rather



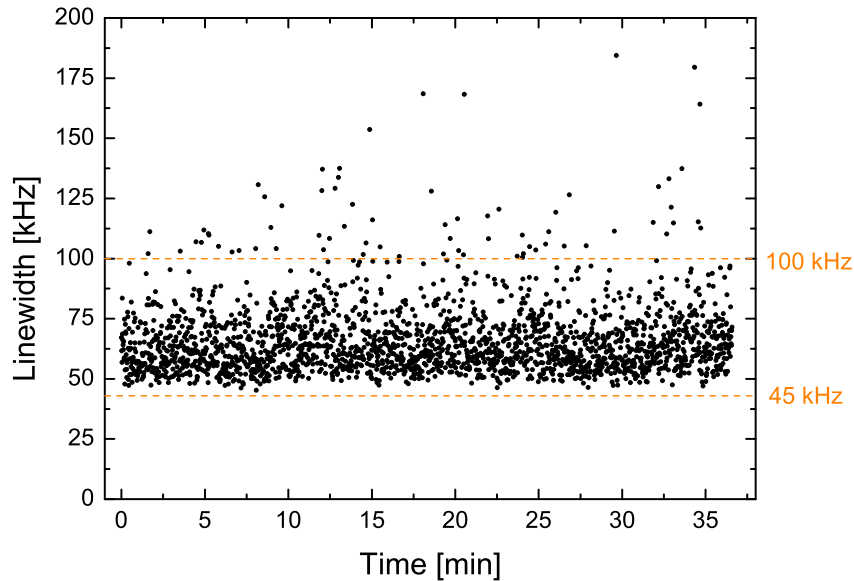


Figure 2.14: Series of frequency linewidth measurements of the visible SFG output, determined from the transmission through a low finesse cavity. Each data point represents the linewidth measured on a time scale of 100 ms with a measurement bandwidth of 75 kHz.

small temperature and wavelength drift, respectively. The results show nevertheless a superior performance in terms of stability, making the OPO-SFG suitable for experiments on ultra-long time scales.

#### 2.5.4 Frequency-Stabilized Operation

We extend the OPO-SFG laser system with a PDH frequency stabilization, described in detail in section 2.4.3. With active PDH, the OPO-SFG output frequency is stabilized to an average value of  $\Delta\nu = 60^{+20}_{-10}$  kHz. We measure this linewidth on a time scale of 100 ms with a commercially available low finesse Fabry-Perot cavity ( $\mathcal{F} \approx 100$ , Sirah, Eagle Eye). Its time-resolved side-of-fringe transmission is monitored to calculate the rms frequency deviation as well as the power spectral density of the laser frequency noise. In a first step, the cavity is scanned over a full FSR to detect the maximum transmission as well as the Airy function. In a second step, the cavity is scanned to half the transmission maximum, i.e., to the side of a transmission fringe. Now, the cavity length is kept fixed and the time-dependent transmission through the cavity is monitored. If we neglect power jitter and vibrational influence, the transmission signal depends only on the frequency jitter of the laser radiation within the transmission window of the Fabry-Perot cavity.

Figure 2.14 shows a series of these linewidth measurements for about half an hour. The lowest obtained linewidth is  $\Delta\nu \approx 45$  kHz and the majority of data points lies below  $\Delta\nu = 100$  kHz. The deviation from measurement to measurement could originate from power jitter of the OPO-SFG ( $< 10\%$  peak to peak noise) or the influence of vibrations on the Fabry-Perot cavity. However, even a power noise correction did not change the measured linewidth. This indicates a slightly fluctuating frequency noise due to an unknown, but most likely vibra-

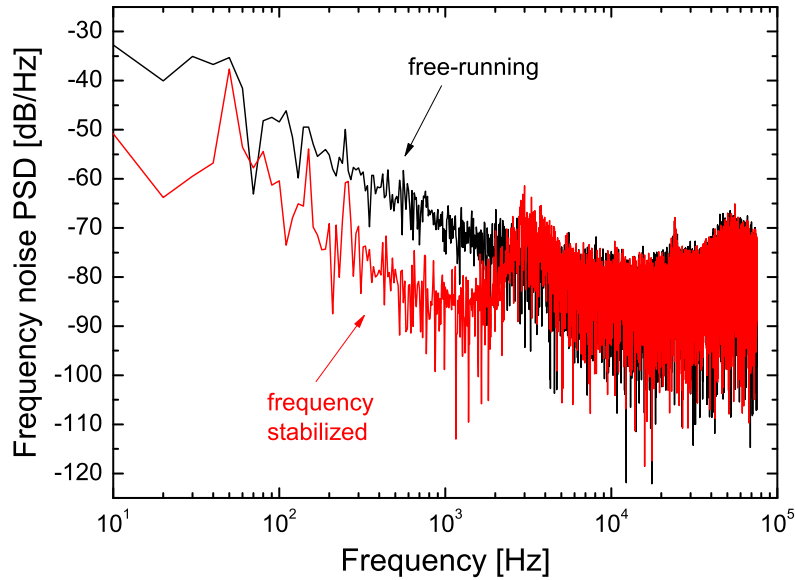


Figure 2.15: Power spectral density (PSD) calculated from the time-resolved transmission through a low finesse cavity in case of frequency stabilized (red line) and free-running OPO-SFG laser system (black line). Note that the figure does not show absolute units on the y-axis and allows only for a relative comparison of the two curves.

tionally caused reason. Vibrations could thereby act either on the Fabry-Perot cavity or on the laser itself. In order to rule out strong frequency linewidth fluctuations of the laser, we determined the linewidth in a spectral hole burning experiment in PrYSO. Therefore we prepare a spectrally isolated absorption line within the inhomogeneous optical transition of PrYSO and measure its width (at this stage, it is not necessary to understand the complete preparation sequence, which is described in the context of light storage in chapter 4.4.5). The spectral width of an absorption line depends on the homogeneous linewidth, residual saturation broadening, the Fourier bandwidth of the preparation and probe pulses as well as the laser frequency linewidth. A typical measurement is given in Appendix B with all relevant spectroscopic parameters. The measurement yields a frequency linewidth of  $\Delta\nu = 114$  kHz. However, the linewidth does not change, e.g., for a single shot measurement and for 128 averages. This rules out strong fluctuations of the frequency noise. The slightly higher noise obtained from the spectral hole burning measurement is most likely due to interactions of the praseodymium ions with their environment during the experiment. However, the exact reason for this line broadening is not known, but has been observed during other experiments as well.

### Spectral Analysis of Frequency Noise

The frequency linewidth is an important quantity to characterize a laser system. In addition, the analysis of the spectral components of the frequency noise can provide essential additional information. They reveal information on the perturbations of laser operation and help to improve locking the laser by adjusting the locking loop accordingly. Besides a more detailed description of our laser system,

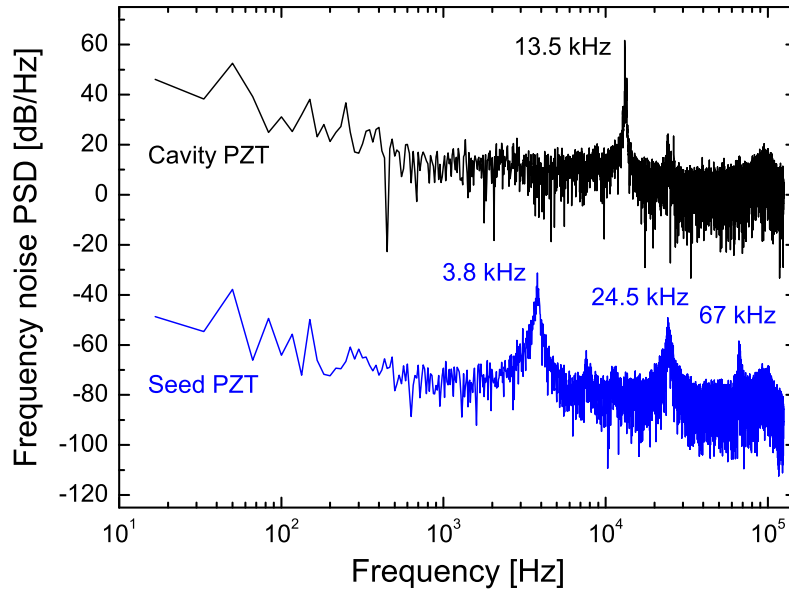


Figure 2.16: Power spectral density (PSD) calculated from the time-resolved transmission through a low finesse cavity. The black line shows the PSD when the cavity PZT is driven with an increased gain. The blue curve shows the PSD when the seed PZT gain is increased.

the goal of this section is to provide a foundation for future optimization of the laser performance by means of the frequency noise spectrum.

The spectral components are calculated by a Fourier transform of the time-resolved transmission through the Fabry-Perot cavity. From the obtained spectrum, we can deduce a frequency-selective noise power. This quantity is called power spectral density (PSD) and can also be used to measure the laser linewidth. Figure 2.15 shows the PSD for frequencies between 10 Hz and 75 kHz in a case when the laser is running freely (black curve) and when it is frequency stabilized (red curve). The data reveal that mainly spectral components below 5 kHz contribute to the frequency noise. This is an important information, because it justifies the use of PZTs only, which are slow noise correctors in the lower kHz regime. Thus no additional, faster correctors are required (as it is usually the case for dye lasers). When the laser runs frequency stabilized, the PSD drops for slow frequencies and the linewidth decreases. However, it is evident from the PSD that further frequency stabilization is possible, as the PSD does not drop to the noise level (given by the noise floor above  $\sim 10$  kHz). But when we increase the gain of the error signal, which is fed to the PZTs, resonances appear and significantly disturb the lock. Note that we already adjusted the PID controller and included low-pass filters (see figure 2.8) in order to suppress resonances. However, they rise again for higher gain. Figure 2.16 shows the PSD when we exclude the low-pass filter between one of the PZTs and its corresponding HV driver. If we increase the gain for this specific PZT, pronounced, single frequency noise components arise in the PSD, showing the specific PZT resonances. We can identify resonances at 3.8 kHz, 24.5 kHz and 67 kHz for the seed PZT (lower, blue curve). The cavity PZT (upper black curve) exhibits a single pronounced resonance at 13.5 kHz. After putting back the low-pass filters we detect the PSD given in figure 2.15, showing only a

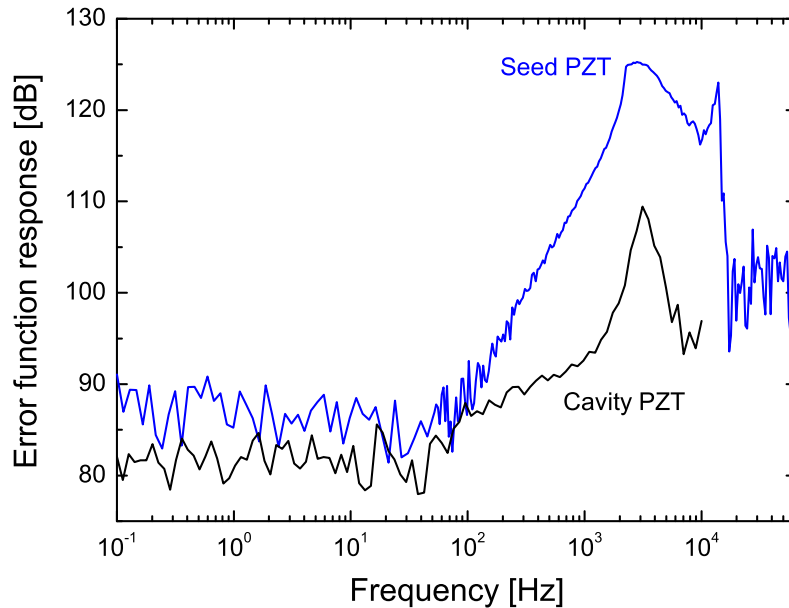


Figure 2.17: Response of the locking loop to spectral noise components. The blue curve describes the response when the seed PZT inserts the noise, the black curve describes the response when the cavity PZT inserts the noise. Note that the bandwidth of the cavity PZT output channel in our locking module is limited to 10 kHz.

small, residual resonance around 2 – 3 kHz, i.e., one of the seed resonances. Even though, the locking loop could be further improved by selectively suppressing the residual resonances to enable more gain at lower frequencies, our locking loop already provides a stable lock with improved frequency stability.

In order to measure the correction bandwidth of the whole adjusted locking loop, it is useful to record a loop response function. This includes all elements contributing to frequency stabilization, i.e., all filters and the PZTs. It measures the response of the locking loop to a certain noise frequency component. Unlike the PSD, it does not show the influence of real noise on the laser system. It rather provides information independent from a noisy environment. A response function is recorded by creating artificial, single frequency noise that is sent into the system by one of the PZTs. At the same time, the reaction of the PDH error signal is measured. If the frequency noise component is immediately compensated by the locking loop, hardly any deviation in the error signal will be measured. This is the case when the loop is able to compensate for this specific spectral disturbance. In case of failing compensation, the error signal indicates a deviation from the frequency reference, mirrored by an increasing response function value. Figure 2.17 shows the response function for the stabilized laser system when all components are included in the locking loop. The blue curve shows the error function response when the seed PZT is used to send the disturbance into the system. The black curve shows the same quantity when the cavity PZT inserts the noise. The data indicates that noise up to 200 Hz is fully compensated by the current locking loop. Note that this bandwidth refers to a 3dB level above detection noise. The compensation for spectral noise components above 200 Hz becomes worse because

several low-pass filters limit the error function response transmitted to the PZTs in the laser system. The data also exhibit some of the PZT resonances of the PZTs, indicated by the peak response in figure 2.17. Although the 3dB bandwidth of the locking loop is limited to 200Hz, it is sufficient in our environment to compensate for a large part of frequency noise and to provide a stable operation of the OPO-SFG laser system.

## 2.6 Conclusion

We set up an all solid-state-laser source based on an OPO and an intra-cavity SFG process. The laser system uses a single PPLN crystal, divided into sections with appropriate poling periods for quasi phase matching of OPO and SFG. The OPO-SFG system provides visible cw radiation in a range between  $\lambda_{\text{vis}} = 605 \text{ nm}$  and  $\lambda_{\text{vis}} = 616 \text{ nm}$  with an output power  $P_{\text{vis}} > 1 \text{ W}$  in the entire wavelength range. In particular we use the OPO-SFG for coherent manipulations in PrYSO at  $\lambda_{\text{vis}} = 606 \text{ nm}$ . We extended the laser system with a PDH frequency stabilization and yield a frequency jitter of  $\Delta\nu = 60_{-10}^{+20} \text{ kHz}$  on a time scale of 100 ms.

In comparison to a previously used dye laser, the OPO-SFG laser system requires less maintenance and performs more robust against external temperature fluctuations and vibrational noise. It performs slightly better in terms of frequency stability and the two systems are comparable in terms of output power. The dye laser on the other hand provides a larger tuning range.

Our laser system uses a PPLN crystal which provides a large transmission range, high non-linearity and the implementation of several frequency mixing processes on single crystals via different periodic poling sections. However, periodic poling limits the thickness of PPLN to values in the range of 1 mm. This requires exact beam alignment of focused beams. As PPLN has cw damage thresholds in the range of  $200 \text{ kW/cm}^2$  to  $500 \text{ kW/cm}^2$  ( $\lambda = 500 \text{ nm} - \lambda = 1500 \text{ nm}$ ), PPLN allows only low- to mid-power applications.

Our specific OPO-SFG system could be further improved by a revised crystal design. The order of OPO and SFG stage should be reversed, which has been suggested to yield higher efficiency and output stability. In addition we operate the SFG stage with three discrete poling periods for QPM whereas the OPO section consists of a fanned poling structure. A double-fanned structure and the use of OPO cavity mirrors with anti-reflection coating for the visible output could help to partially suppress the large power fluctuations for different output wavelength and help to tune the OPO-SFG more easily to arbitrary wavelength within its output spectrum.

## Chapter 3

# Coherent Light-Atom Interaction

This chapter introduces the basics of coherent light-atom interactions. In contrast to incoherent interaction, these enable a variety of atomic manipulations that go beyond rate-equation-like behaviour. Coherent interactions are the basis for all light storage experiments presented in this thesis. In particular they are the basis for the here investigated techniques that serve to prolong storage duration and enhance storage efficiency (see chapters 4 and 5).

This chapter highlights some fundamentals of light-atom interaction in order to introduce the most important quantities and correlations. It first discusses the interaction with a two-state system in order to overview basic population dynamics driven by a coherent light field [60]. The manipulation of population distributions or atomic state superpositions is the key mechanism for all experiments presented in this thesis. The interaction can be easily expanded to a three-state system, which eventually enables light storage by means of electromagnetically induced transparency, the light storage technique used during this work.

### 3.1 Interaction with a Two-State System

In order to describe coherent interactions, we treat the driving field in a classical way and the atom as a quantum system, a simplification known as the semi-classical approach. In this chapter we consider only the interaction between a two-state system and an electric radiation field as the interaction with a magnetic field is analogous. We consider a two-state system as illustrated in figure 3.1, with two energy levels  $|1\rangle$  and  $|2\rangle$  that have energies  $\epsilon_1$  and  $\epsilon_2$ . The temporal evolution of this system is given by the time-dependent Schrödinger equation (TDSE)

$$i\hbar \frac{d}{dt} |\psi(t)\rangle = \hat{H}(t) |\psi(t)\rangle \quad (3.1)$$

where

$$|\psi(t)\rangle = c_1(t)|1\rangle + c_2(t)|2\rangle \quad (3.2)$$

represents the wave function of the entire system with probability amplitudes  $c_i(t)$  for the system to be in state  $|i\rangle$ . The Hamiltonian  $\hat{H}$  describes the system and consists of the Hamiltonian  $\hat{H}_0$  of the unperturbed two-state system as well as  $\hat{H}_I(t)$ , the Hamiltonian describing the time dependent interaction between an electric field

$$\vec{E}(t) = \frac{1}{2} \vec{\mathcal{E}}_0(t) (e^{-i\omega t} + e^{+i\omega t}) \quad (3.3)$$

and the two-state system. The electric field oscillates with the angular frequency  $\omega$  and has a real amplitude  $\mathcal{E}_0(t)$ . The full Hamiltonian  $\hat{H}$  reads

$$\hat{H}(t) = \hat{H}_0 + \hat{H}_1(t) = \begin{pmatrix} E_1 & 0 \\ 0 & E_2 \end{pmatrix} + \begin{pmatrix} 0 & -\vec{\mu}_{12}\vec{E}(t) \\ -\vec{\mu}_{21}\vec{E}(t) & 0 \end{pmatrix} = \begin{pmatrix} E_1 & -\vec{\mu}_{12}\vec{E}(t) \\ -\vec{\mu}_{21}\vec{E}(t) & E_2 \end{pmatrix} \quad (3.4)$$

with the dipole transition moment  $\vec{\mu}_{ij} = \vec{\mu}_{ji}^*$  and the interaction energy  $\vec{\mu}_{ij}\vec{E}(t)$ . Note that the electric field  $\vec{E}(t)$  depends only on time and the spatial phase is negligible because its wavelength is typically longer than the atom extent. When the Hamiltonian is written in Dirac notation by appropriate setting of a phase for the probability amplitudes  $c_i(t)$ , it reads [60]

$$\hat{H}_{\text{Dirac}}(t) = -\frac{\hbar}{2} \begin{pmatrix} \Delta & \Omega_{12}(t)(1 + e^{i2\omega t}) \\ \Omega_{12}(t)^*(1 + e^{-i2\omega t}) & -\Delta \end{pmatrix} \quad (3.5)$$

with detuning  $\Delta = \omega - \omega_0$  of the light field from the resonance frequency  $\omega_0$  and

$$\Omega_{ij}(t) = \frac{\vec{\mu}_{ij}\vec{\mathcal{E}}_0(t)}{\hbar} \quad (3.6)$$

$\Omega_{ij}(t)$  is called the Rabi frequency and represents the interaction strength between a driving electric field and an atomic transition. Note that  $\Omega(t)$ ,  $\Delta(t)$  as well as  $\dot{\Omega}(t)$  are usually much smaller than the carrier frequency  $\omega$  of the electric field and thus we can apply the *rotating wave approximation* (RWA), which further simplifies the total Hamiltonian to

$$\hat{H}_{\text{RWA}}(t) = -\frac{\hbar}{2} \begin{pmatrix} \Delta & \Omega_{12}(t) \\ \Omega_{12}(t)^* & -\Delta \end{pmatrix} \quad (3.7)$$

### 3.1.1 Rabi Oscillations and Pulse Area

In case of a resonant driving field, the Rabi frequency (3.6) is a parameter that describes both interaction strength and population dynamics in a two-state system. If we assume the entire population to be in state  $|1\rangle$  initially, the solution of the TDSE with the RWA Hamiltonian describes oscillations of the entire population between states  $|1\rangle$  and  $|2\rangle$ . The oscillation frequency is the Rabi frequency and the population dynamics are termed Rabi oscillations. The final state of the system is in this case solely defined by the pulse area  $\mathcal{A}$ , which is defined by the duration  $\tau$  of the interaction and the Rabi frequency. The pulse area reads

$$\mathcal{A} = \int_0^\tau \Omega dt \quad (3.8)$$

After a pulse that has an area of  $\mathcal{A} = \pi$ , the population is entirely transferred from state  $|1\rangle$  to state  $|2\rangle$ . A pulse area of  $\mathcal{A} = 2\pi$  takes the system to state  $|2\rangle$

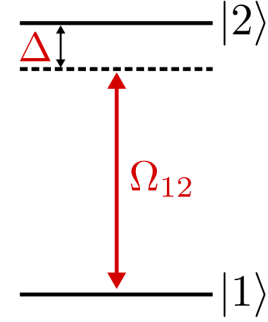


Figure 3.1: Atomic two-state system with driving field  $\Omega_{12}$  and detuning  $\Delta$ .

and back to state  $|1\rangle$ . The corresponding pulses are called  $\pi$  and  $2\pi$  pulses. A pulse with area  $0 < \mathcal{A} < \pi$  does not transfer the full population to a single state, but creates a superposition of states  $|1\rangle$  and  $|2\rangle$ . This superposition is called atomic coherence. The two complex probability amplitudes  $c_1$  and  $c_2$  define the amplitude and the phase of the coherence as  $c_1 c_2^*$ . The maximum possible magnitude of the coherence is  $1/2$ , a value that occurs along with equal populations after a  $\pi/2$  pulse.

In this basic example the Rabi frequency defines the velocity of changes in the two-state system. If the driving field has a detuning  $\Delta$  and Rabi frequency and detuning are time-dependent, the evolution of the system becomes more complex. The evolution velocity is now determined by the effective Rabi frequency

$$\Omega_{\text{eff}}(t) = \sqrt{\Omega^2(t) + \Delta^2(t)} \quad (3.9)$$

The pulse area on the other hand is not sufficient anymore in order to describe the entire evolution of a system. Looking again at population oscillations, a detuned field causes an oscillation with the effective Rabi frequency. After a pulse area of  $\mathcal{A} = \pi$  the population transfer does reach a maximum. However, the population in state  $|2\rangle$  is not the entire population which initially was in state  $|1\rangle$ . A detuned driving field transfers only a fraction  $\Omega^2/\Omega_{\text{eff}}^2$  of the population to state  $|2\rangle$ . The temporal evolution of the probability amplitudes  $c_i$  becomes even more complex when the initial state of the system is a superposition of states  $|1\rangle$  and  $|2\rangle$  and all parameters are time-dependent (see, e.g., chapter 4.2).

### 3.1.2 Description of Macroscopic Systems

The preceding description referred to a single two-state system. However, in general and in the specific case of Pr:YSO, an applied field interacts with a manifold of atomic systems. In such situations the probability amplitudes of a single system are not sufficient to describe the dynamics of the whole medium. Instead, all measured quantities, like population distributions or coherent superpositions, are averaged values involving many contributing systems.

In this case, the density matrix formalism offers a simpler and unified approach in order to describe two cases, a single and also a macroscopic system. The density matrix  $\hat{\rho}$  is calculated from the probability amplitudes  $c_j$  that, when squared absolutely, give the probability of finding a single system in state  $|\psi_j\rangle$ . It reads

$$\hat{\rho} = \sum_{i,j} c_i c_j^* |\psi_i\rangle \langle \psi_j| \equiv \sum_{i,j} \rho_{ij} \quad (3.10)$$

In a macroscopic system, the density matrix elements  $\rho_{ij}$  are calculated from the sum of all contributing systems  $m$

$$\rho_{ij} = \sum_m p_m c_i c_j^* |\psi_i\rangle \langle \psi_j| \quad (3.11)$$

where  $p_m$  are the normalized weightings for each system. The physical meaning of the diagonal entries  $\rho_{jj}$  is the probability to find population in the  $j$ th state of the



macroscopic system. Off-diagonal entries  $\rho_{ij}$  represent coherences between states  $|i\rangle$  and  $|j\rangle$ . In this thesis, we write coherences in the form  $\rho_{ij} = |\rho_{ij}| \exp(i\gamma)$ , where  $|\rho_{ij}|$  is the amplitude and  $\gamma$  the phase of the coherence. Note that we choose the coherence to have a zero phase when it consists only of an imaginary part. However, this choice facilitates illustration and explanation, but is without any restriction to general validity of theoretical descriptions given in this thesis.

In macroscopic systems the density matrix gives the information on the overall population distribution and the overall coherence. The temporal evolution of the density matrix is given by the Liouville-von-Neumann equation

$$i\hbar \frac{d}{dt} \hat{\rho} = [\hat{H}, \hat{\rho}] + i\hbar \hat{D} \quad (3.12)$$

where the Hamilton operator in our case would be  $\hat{H} = \hat{H}_{\text{RWA}}$ . In order to include decay mechanisms, which act on populations (relaxation or decay) or on coherences (decoherence), the density matrix formalism uses the dissipator  $\hat{D}$ , whose diagonal elements are

$$D_{nn} = -\rho_{nn} \sum_k \Gamma_{nk} + \rho_{jj} \sum_j \Gamma_{jn} \quad (3.13)$$

where  $\Gamma_{ij}$  are phenomenological population decay rates from state  $|i\rangle$  to  $|j\rangle$ . Its off-diagonal elements are defined to be

$$D_{ij} = -\rho_{ij} \gamma_{ij} \quad (3.14)$$

where  $i \neq j$  and  $\gamma_{ij}$  are phenomenological decoherence rates defined by the decoherence time  $T_2 = 1/\gamma$ . Equation (3.14) contains a quite general expression for the decoherence rates  $\gamma_{ij}$ , which typically include population relaxation but also other decoherence mechanisms which do not affect populations. Note that we define a coherence with a phase and an amplitude. In PrYSO a fluctuating crystal environment influences the phase and its evolution of individual coherences. Whenever multiple coherences are prepared this leads to interference phenomena that potentially decrease the overall coherence while individual coherences may still exist. Those effects are as well included in the decoherence rates  $\gamma_{ij}$ . Note that in order to describe decoherence and population relaxation with a dissipator both of these processes must have Markovian character [60]. As a simple example, the two-state system dissipator (with all population in state  $|1\rangle$  being the thermal equilibrium) is

$$\hat{D} = \begin{pmatrix} \frac{1}{T_1} \rho_{22} & -\frac{1}{T_2} \rho_{12} \\ -\frac{1}{T_2} \rho_{21} & -\frac{1}{T_1} \rho_{22} \end{pmatrix} \quad (3.15)$$

with  $T_1$ , the population life-time and  $T_2$ , the decoherence time. Simulations shown in this thesis are based either on the TDSE or the density matrix formalism.

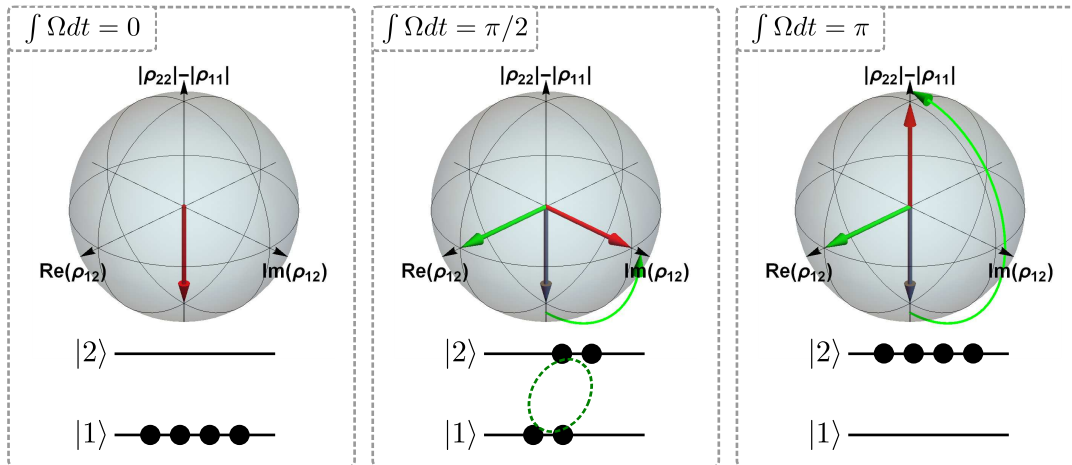


Figure 3.2: Coherent driving of a two-state system depicted in the Bloch picture and by the population in the two states  $|1\rangle$  and  $|2\rangle$ . The Bloch vector is depicted in red, torque vector in green and the gray vector represents the initial state before the interaction starts. (Left) All population is in state  $|1\rangle$ . (Center) The system is driven to a maximum superposition of both states by a pulsed driving field with pulse area  $\mathcal{A} = \pi/2$ . (Right) All population is transferred from state  $|1\rangle$  to state  $|2\rangle$  by a  $\pi$  pulse.

### Bloch Sphere Picture

We saw in the last sections that interactions of a coherent driving field with a two-state system are suitable to manipulate populations and to create atomic coherences. The Bloch sphere represents an instructive method to display the behaviour of a driven two-state system (see figure 3.2). In this picture the position of the Bloch vector  $\vec{r}$  represents the current state of the system. It is defined as

$$\vec{r} = (2\text{Re}[\rho_{12}], 2\text{Im}[\rho_{12}], |\rho_{22}| - |\rho_{11}|) \quad (3.16)$$

Note that the Bloch sphere usually depicts the Bloch vector in a rotating frame with the (central) frequency of the (inhomogeneously broadened) transition  $|1\rangle \leftrightarrow |2\rangle$ . The z-component of the Bloch vector represents the population difference between state  $|1\rangle$  and  $|2\rangle$ . Figure 3.2 (left) shows the Bloch vector when the population is in state  $|1\rangle$  only, i.e.,  $\vec{r}$  points in the -z direction. The x- and y-components of  $\vec{r}$  represent real and imaginary part of the coherence  $\rho_{12}$ , i.e., they show coherent superpositions of the two involved states. The phase of the coherence  $\gamma$  is

$$\gamma = \arctan\left(\frac{\text{Im}[\rho_{12}]}{\text{Re}[\rho_{12}]}\right) \quad (3.17)$$

As an important consequence, the phase of a coherence can be deduced directly from the projection of the Bloch vector on the equatorial plane of the Bloch sphere. This fact enables an easy identification of phase changes, relative phases between two Bloch vectors or visualization of interference phenomena between several Bloch vectors or coherences, respectively.

The Bloch sphere is especially useful to see the influence of a driving field on the two-state system or the Bloch vector  $\vec{r}$ , respectively. The driving field is

represented by a torque vector (green arrow in figure 3.2)

$$\vec{T} = (\text{Re}[\Omega], \text{Im}[\Omega], \Delta) \quad (3.18)$$

This vector controls the motion of the Bloch vector via the TDSE, translated into the Bloch sphere picture as a torque equation

$$\dot{\vec{r}} = \vec{T} \times \vec{r} \quad (3.19)$$

Note that also the driving field possesses a phase relative to the rotating frame of the Bloch sphere, i.e., the phase and frequency of the atomic coherence. The phase is defined with respect to the first interaction pulse. In our case, a resonant driving field has a zero phase when its torque vector points into the  $\text{Re}[\rho_{12}]$  direction of the Bloch sphere. Whenever we depict the torque vector in a Bloch sphere, we use a vector which is normalized to unit length.

Figure 3.2 (center and right) also shows two common cases of resonant pulsed fields with a pulse area of  $\mathcal{A} = \pi/2$  and  $\mathcal{A} = \pi$ . As seen on the Bloch sphere, the  $\pi/2$  pulse drives the system to a maximum coherent superposition  $\rho_{12} = i/2$ , i.e., the Bloch vector lies in the  $xy$ -plane. The  $\pi$  pulse inverts the population.

## 3.2 Interaction with a Three-State System

The above description for a two-state system is an important but basic scenario for the interaction between electromagnetic fields and an atomic system. The extension to the interaction between two radiation fields and a three-state system has many similarities to the two-state case. Figure 3.3 illustrates an example of a three-state system in  $\Lambda$ -configuration, i.e., two metastable ground states  $|1\rangle$  and  $|2\rangle$  and one excited state  $|3\rangle$  as well as a probe field  $E_p(t)$  and a control field  $E_c(t)$  with Rabi frequencies  $\Omega_p(t)$  and  $\Omega_c(t)$  and detunings  $\Delta_p(t)$  and  $\Delta_c(t)$ , respectively. Furthermore, the transition between the two ground states will be dipole forbidden. The three-state Hamilton operator in the rotating wave approximation reads

$$\hat{H}_{\text{RWA}}^{3\text{LS}} = -\frac{\hbar}{2} \begin{pmatrix} 0 & 0 & \Omega_p(t) \\ 0 & -2(\Delta_p(t) - \Delta_c(t)) & \Omega_c^* \\ \Omega_p^*(t) & \Omega_c & -2\Delta_p(t) \end{pmatrix} \quad (3.20)$$

Diagonalizing  $\hat{H}_{\text{RWA}}^{3\text{LS}}$  in the case of two photon resonance  $\Delta_p(t) = \Delta_c(t) \equiv \Delta$  yields the new eigenfunctions

$$\begin{aligned} |\psi_0\rangle &= \cos\Theta|1\rangle - \sin\Theta|2\rangle \\ |\psi_+\rangle &= \sin\Theta\sin\phi|1\rangle + \cos\Theta\sin\phi|2\rangle + \cos\phi|3\rangle \\ |\psi_-\rangle &= \sin\Theta\cos\phi|1\rangle + \cos\Theta\cos\phi|2\rangle - \sin\phi|3\rangle \end{aligned} \quad (3.21)$$

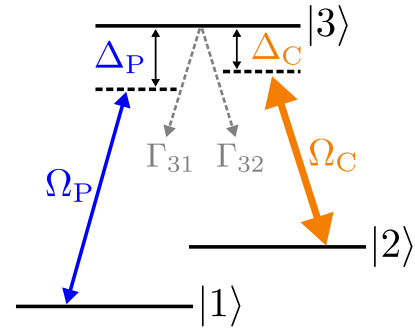


Figure 3.3: Atomic three-state system with a weak probe field  $\Omega_p$  and a strong control field  $\Omega_c$ . Their respective detunings are  $\Delta_p$  and  $\Delta_c$ .  $\Gamma_{31}$  and  $\Gamma_{32}$  are decay rates from the excited state  $|3\rangle$  to the two metastable ground states  $|1\rangle$  and  $|2\rangle$ .

These formulas define instantaneous eigenfunctions, for a specific time  $t$ . The mixing angles  $\Theta$  and  $\phi$  are defined by

$$\sin\Theta = \frac{\Omega_p(t)}{\sqrt{\Omega_c^2(t) + \Omega_p^2(t)}} \quad \text{and} \quad \cos\Theta = \frac{\Omega_c(t)}{\sqrt{\Omega_c^2(t) + \Omega_p^2(t)}} \quad \rightarrow \quad \tan\Theta = \frac{\Omega_p(t)}{\Omega_c(t)} \quad (3.22)$$

and

$$\tan 2\phi = \frac{\sqrt{\Omega_p^2(t) + \Omega_c^2(t)}}{\Delta} \quad (3.23)$$

The instantaneous eigenfunctions exhibit an interesting feature, i.e.,  $|\psi_0\rangle$  does not contain a contribution of the bare state  $|3\rangle$ , the only state which is usually subject to radiative decay. Thus  $|\psi_0\rangle$  is non radiative and called *dark state*. Because of the contribution of state  $|3\rangle$  to states  $|\psi_{\pm}\rangle$  these are called *bright states*. The dark state only contains the metastable states  $|1\rangle$  and  $|2\rangle$  in a superposition defined by the mixing angle  $\Theta$ , depending only on the ratio between control and probe Rabi frequency. Hence the dark state enables the preparation of a superposition of two ground states, i.e., an atomic coherence in the  $|1\rangle \leftrightarrow |2\rangle$  transition.

### 3.2.1 EIT-Based Light Storage

In this thesis we use a storage protocol that stores a weak probe light pulse on the transition  $|1\rangle \leftrightarrow |3\rangle$  by means of a much stronger control field on the transition  $|2\rangle \leftrightarrow |3\rangle$ , i.e.,  $\Omega_p \ll \Omega_c$ . With the latter condition and all population in state  $|1\rangle$  initially, the system is only in the dark state  $|\psi_0\rangle$  because the bright states become superpositions of empty states  $|2\rangle$  and  $|3\rangle$ . Our goal is to store the weak probe pulse in a persistent atomic ground state coherence  $\rho_{12}$  via the dark state, which includes the two ground states. In particular, the ground state coherence  $\rho_{12}$  is defined by equation (3.21) as  $\rho_{12} = c_1 c_2^* = \cos\Theta \sin\Theta$ . In case of a strong control pulse, we find  $c_1 = \cos\Theta \approx 1$  and the coherence

$$\rho_{12} \approx c_2^* = \sin\Theta \approx \frac{\Omega_p}{\Omega_c} \quad (3.24)$$

depends linearly on the probe Rabi frequency. Thus the dark state enables the preparation of an atomic ground state coherence that is proportional to the probe field as long as the latter is weak compared to the control field.

However, the storage protocol does not solely rely on transferring light to a superposition of atomic states but as well on a modification of absorption and dispersion properties of the medium. In presence of the strong control field the conditions under which a pulsed probe beam propagates through the medium change substantially. In particular the absorption for the probe beam vanishes, which is termed *electromagnetically induced transparency* (EIT) [9]. The first order susceptibility  $\chi^{(1)}$  exhibits all important features that are relevant to understand EIT and EIT-based light storage. It is calculated from the expectation value of the atomic polarization  $\vec{P}(t) = \epsilon_0 \chi^{(1)} \vec{E}_{13} = N \vec{\mu}_{13} \rho_{13}$ , which depends on the coherence on the probe transition  $\rho_{13}$  ( $N$  is the particle number density). The coherence can

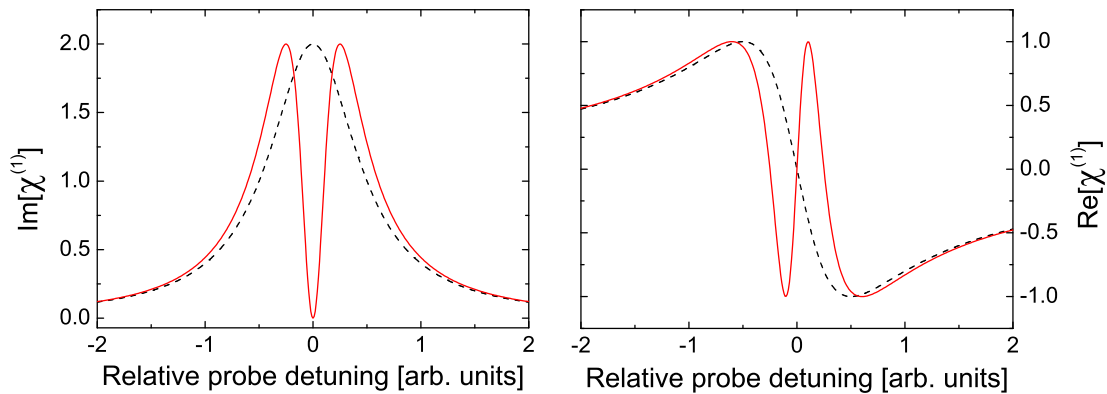


Figure 3.4: (Left) Simulation of the imaginary part, (right) real part of the linear susceptibility versus the probe detuning from resonance of the  $|1\rangle \leftrightarrow |3\rangle$ . The black, dashed lines show the susceptibility without a control field. The red, solid line shows the susceptibility in presence of a strong control field.

be calculated from the density matrix to determine the linear susceptibility. A detailed calculation and analysis of EIT and its applications can be found in [10] and references therein. This thesis will discuss only the relevant results to understand EIT-based light storage. The first order susceptibility  $\chi^{(1)}$  contains absorption and dispersion properties for a weak probe beam. In the case of weak polarizability, the absorption coefficient  $\alpha$  and the dispersive part of the refractive index  $\text{Re}[n]$  are calculated to be [61]

$$\alpha = \frac{2\pi}{\lambda} \text{Im}[\chi^{(1)}] \quad \text{Re}[n] = 1 + \frac{\text{Re}[\chi^{(1)}]}{2} \quad (3.25)$$

Figure 3.4 (left) shows the absorption spectrum for a weak probe beam when no strong control field is interacting with the medium (black, dashed line) and in the presence of a strong control field (red, solid line). When the control field is present, the resonant absorption for the probe beam vanishes entirely. It allows lossless transmission of the probe beam through an originally opaque medium. This specific effect is termed EIT. Furthermore, the original absorption line splits into two lines, whose center-to-center distance is proportional to the control Rabi frequency  $\Omega_C$ . This splitting is known as *Autler-Townes splitting*. Even in case of a small Autler-Townes splitting, the absorption on resonance vanishes as long as the condition  $|\Omega_C|^2 \gg \gamma_{13}\gamma_{12}$ , where  $\gamma_{ij}$  are decoherence rates, holds true. However, zero absorption indicates also an interference phenomenon to be responsible for EIT. The system was prepared to be in the dark state  $|\psi_0\rangle = |1\rangle$  initially. The probe beam couples this state to the excited state  $|3\rangle$ , which is involved in the two bright states. Coupling states  $|1\rangle$  and  $|3\rangle$  thus involves two possible transitions,  $|\psi_0\rangle \leftrightarrow |\psi_+\rangle$  and  $|\psi_0\rangle \leftrightarrow |\psi_-\rangle$ . The two possible interaction paths interfere destructively and the probe beam absorption vanishes on resonance. In the case of a strong control field and a negligible decoherence rate  $\gamma_{12} \rightarrow 0$  between the two metastable ground states  $|1\rangle$  and  $|2\rangle$ , the angular-frequency full width half

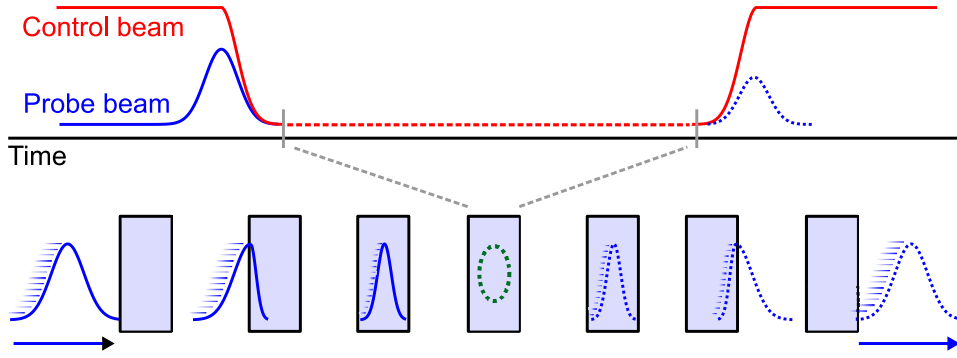


Figure 3.5: (Upper row) Temporal sequence of EIT-based light storage. Red line depicts the control beam, the blue line depicts the probe beam. The blue dashed part represents the read out probe pulse. (Lower row) A probe pulse propagating through the PrYSO crystal under EIT conditions, i.e., in presence of a strong control beam. As soon as the pulse enters the medium, it is slowed down and compressed. When the control and probe beam are shut off simultaneously, the probe beam is converted into a persistent atomic coherence (green dashed circle). After turning on the control beam again, the atomic coherence is converted back into the probe pulse.

maximum (FWHM) of the EIT window  $\Gamma_{\text{EIT}}$  is given by the expression [10]

$$2\pi \times \Gamma_{\text{EIT}} = \frac{\Omega_C^2}{\sqrt{\Gamma_{31}\gamma_{13}}} \frac{1}{\sqrt{\alpha L}} \quad (3.26)$$

with the medium length  $L$ , the decoherence rate  $\gamma_{13}$  and the population decay rate  $\Gamma_{31}$  on the probe transition (as defined in section 3.1.2). Consequently, a large control Rabi frequency yields a large EIT window width. When the probe field is pulsed, a broad window enables lossless propagation of spectrally broader pulses.

Figure 3.4 (right) shows the dispersive part of the refractive index for the probe beam with respect to its detuning from resonance. Again, the spectrum exhibits a significant change in presence of a control field (red, solid line). Especially around (two-photon) resonance, the dispersion's derivative becomes positive. The group velocity of a pulse is also affected by the dispersion. On two-photon resonance it is given by [10]

$$v_{\text{gr}} = \frac{c}{n + \omega_p(dn/d\omega_p)} = \frac{c}{1 + \alpha c \frac{\Gamma_{31}}{\Omega_C^2}} \quad (3.27)$$

For low control Rabi frequency (or a narrow EIT window), the group velocity of a pulse inside the medium is proportional to  $v_{\text{gr}} \sim (\Omega_C^2/\alpha)$  and thus slower than in vacuum. This phenomenon is known as *slow light* [13]. It leads to the compression of a pulse inside the medium which depends on the steepness of the dispersion slope (or the square of the control Rabi frequency). In the limiting case of a zero control field, the group velocity tends to zero, termed *stopped light*.

The goal of EIT-based light storage is to compress a probe pulse such that it spatially fits inside the medium. In addition, equations (3.21) and (3.22) show

that the presence of both, control and probe field creates a coherent superposition of the metastable states  $|1\rangle$  and  $|2\rangle$ , a coherence, which is proportional to the probe Rabi frequency (for weak probe fields). If both, the control and probe field are turned off simultaneously while maintaining their ratio, the mixing angle  $\Theta$ , i.e., the atomic coherence, does not change. The removal of the control field  $\Omega_C \rightarrow 0$  also causes the group velocity (3.27) of the probe pulse to approach zero. Thus, a localized atomic coherence persists in the medium after the storage process. Note that the probe light field is completely transferred into an atomic coherence and hence this process is different from *stationary light*, where the probe pulse is still present in the medium but has a zero group velocity [62]. Figure 3.5 shows the temporal sequence for the control and probe beam in a light storage experiment. It also sketches the probe pulse, propagating through the storage medium under EIT conditions (lower row). To retrieve the light field from the atomic coherence, the control field is turned on again, the storage process is reversed and the probe pulse propagates without loss through the medium under EIT conditions. EIT-based light storage thus enables on demand read out of the probe field.

This section only discussed the very basics of EIT-based light storage. It does not contain a discussion of all parameters or effects that influence the storage process. These include pulse propagation, pulse shaping, the influence of optical depth or readout directions and the ratio between probe and control Rabi frequency. A detailed discussion on the topic of storage efficiency is given in, e.g., [7, 10, 63] and references therein. The listed citations also give an alternative description of the discussed light-matter interaction by means of a quasi particle, the so-called *dark state polariton*. However, for this thesis the storage process itself does not play a significant role. This work deals with the prolongation of the storage time of atomic coherences and with the enhancement of read-out efficiency after a certain storage duration. The efficiency is reduced by effects like dephasing, decoherence and population decay, as will be discussed in the following section.

### 3.2.2 Limitations of Storage Duration

The storage duration of atomic coherences is limited by the coherence life-time, i.e., the decoherence time  $T_2$ . Numerous effects contribute to decoherence in PrYSO.

Population relaxation is a first source of decoherence. It takes a system back to a pure state or an incoherent superposition of two states after a characteristic time  $T_1$ . In PrYSO, population relaxation occurs via radiative decay and the interaction with unsuppressed phonons (we operate the experiment at cryogenic temperatures to decrease the probability for phonon excitation). In the case of population relaxation only, the maximum coherence life-time  $T_2$  is given by  $T_2 = 2T_1$ .

However, light storage in PrYSO drives a collective excitation of coherences, i.e., not only a single system is driven to a coherent superposition of two states, but a manifold of systems carries coherences at the same time. Also storing a single photon would result in a collective excitation, because many systems absorb the

photon with an unknown probability. In PrYSO, a light pulse is always stored in a variety of individual coherences, i.e., in a large number of Pr ions within the crystal. Each coherence has a certain magnitude and a phase  $\gamma$ , the latter evolving in time with  $\gamma = \omega_0 t$ , where  $\omega_0$  is the transition frequency of the two levels that carry the coherence. The fact that each individual coherence carries a phase permits loss of the overall coherence via interference as soon as individual phases change unequally.

Inhomogeneous broadening is a first source of such unequal phase evolution. Inhomogeneously broadened transitions provide a continuous variety of transition frequencies. Hence we find a continuous variety of individual phase evolutions. After some time  $t$ , individual coherences have different phases. This process is called dephasing and leads to destructive interference within the collective excitation. Dephasing usually leads to a fast loss of the overall coherence and inhibits information storage on long time scales. Nevertheless, it is a deterministic and therefore reversible process that can easily be compensated. Chapter 4 presents a technique for efficient *rephasing* of atomic coherences in order to enable efficient read-out of stored light, even on time scales beyond the dephasing time.

Stochastic yttrium spin flips in the PrYSO host crystal are an additional source that induce phase changes. Spin flips cause a change in the transition frequency of neighbouring Pr ions via dipole-dipole interaction. Hence they randomly change the phase evolution for a single coherence (see also the comments on spectral diffusion in chapter 1). As this is a non deterministic process, simple rephasing is not enough to compensate the effect of random phase changes. However, a variety of techniques exist to compensate for such type of decoherence, i.e., to decouple a system from the influence of its environment. One way is dynamical decoupling [28, 29], which uses a series of pulsed electromagnetic fields to minimize the effect of decoherence. Static decoupling on the other hand uses DC fields, applied to the storage medium to suppress the sources of decoherence as well as to minimize their effect [25–27]. Both types of decoupling are currently intensively investigated and with their combination, ultra-long light storage times up to minutes have been achieved in rare-earth-ion-doped crystals [26]. Storage times up to hours have been achieved for atomic coherences prepared by RF  $\pi/2$  pulses [27]. In the case of perfect decoupling, the decoherence time eventually approaches its theoretical limit, defined by twice the population relaxation time. However, the application of DC and AC fields usually implies a large technological effort, making an experiment bulky and susceptible to errors.

Chapter 5 of this thesis presents a novel, alternative way to preserve an atomic coherence and achieve ultra-long storage times without the need for complex technical efforts. The technique relies on reversible mapping of a coherence onto a persistent population distribution and back after a storage time, which is only limited by population relaxation and completely insensitive to decoherence.



## Chapter 4

# Adiabatic Rephasing of Atomic Coherences

Data storage in atomic coherences in inhomogeneously broadened media typically leads to a loss of the total coherence after very short storage durations. In PrYSO, a stored light signal vanishes after approximately  $10 - 20 \mu\text{s}$ . The reason is dephasing, i.e., a different phase evolution of individual coherences leading to destructive interference (see section 4.1). On the other hand, dephasing is fully reversible and can be compensated by the application of a  $\pi$  pulse, which is known as a spin echo or Hahn echo [64]. However,  $\pi$  pulses require a tightly defined pulse area, which makes the spin echo efficiency sensitive to errors or fluctuations of experimental parameters. Adiabatic interactions on the other hand are a class of coherent interactions, which allow the control of quantum systems without such strict requirements for experimental parameters. One specific adiabatic interaction is *rapid adiabatic passage* (RAP), which performs similar to a  $\pi$  pulse for population inversion [23]. Therefore, RAP and other adiabatic pulses have been extensively studied with respect to their ability of rephasing, in particular in NMR [24, 65–67]. Recently, RAP was also tested for rephasing with RF induced atomic coherences in the rare-earth ion doped solid Thulium:YAG [68–70].

This thesis presents an experimental realization of RAP, used for rephasing of atomic coherences prepared in an EIT-based light storage experiment in PrYSO. In addition to previous work, we provide a detailed, systematic experimental analysis about the performance of RAP under imperfect conditions and compare it to rephasing by  $\pi$  pulses under the same conditions. This chapter starts with a theoretical introduction of dephasing and rephasing of atomic coherences. It presents the class of adiabatic interactions and discusses RAP in the context of population transfer and rephasing. After a description of the experimental implementation of light storage and RAP, the chapter presents the experimental results obtained with RAP and  $\pi$  pulse based rephasing.

## 4.1 Dephasing and Rephasing

Storing information in atomic coherences in an inhomogeneously broadened medium leads to dephasing. Dephasing is the simultaneous phase evolution of individual coherences  $\rho_{ij}$  with the phase factor  $\exp(i\omega_{ij}t)$ , where  $\omega_{ij}$  is the angular frequency of the transitions carrying atomic coherences. After an evolution time  $t$ , the individual coherences within the inhomogeneous line have non-equal phases due to different transition frequencies  $\omega_{ij}$ . After a characteristic time  $\tau_{\text{deph}}$ , this phase evolution leads to complete destructive interference between individual coherences and prevents the read-out of a macroscopic coherence. The dephasing

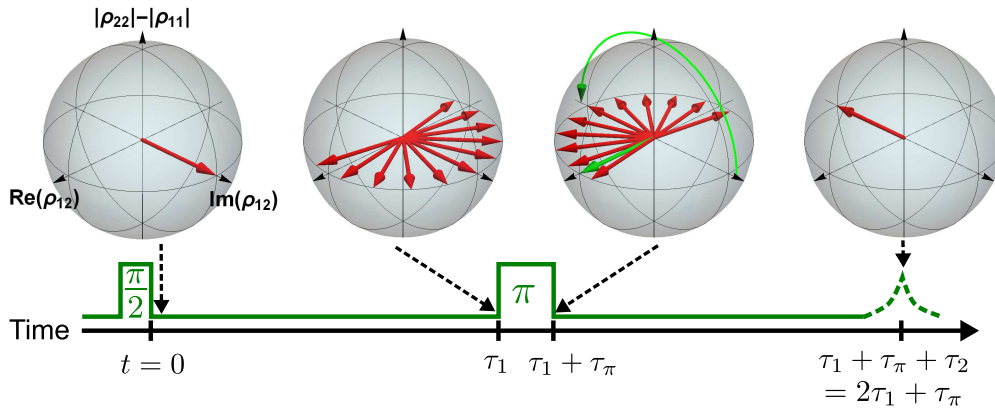


Figure 4.1: Bloch sphere illustration of a rephasing process of atomic coherences in an inhomogeneously broadened transition, driven by a  $\pi$  pulse. Each Bloch vector (red) represents a two-state system with an individual transition frequency  $\omega_{ij}$ . The torque vector of the driving field is shown in green color. Each Bloch sphere shows a snapshot during a dephasing and rephasing process for moments in time as indicated on the time line.

time  $\tau_{\text{deph}}$  is obtained from the Fourier transformed shape of the inhomogeneous transition. In case of a Gaussian shape with a full width half maximum (FWHM)  $\Gamma_{\text{inh}}$ , the dephasing time is  $\tau_{\text{deph}} = 1/(\pi\Gamma_{\text{inh}})$ .

However, dephasing is fully reversible provided that the phase evolution is constant, i.e., every system that carries a coherence has a temporally constant transition frequency  $\omega_{ij}$ . The most common technique to reverse dephasing is the Hahn echo [64] or spin echo, which is explained in an easy way by the dynamics of the Bloch vector. Figure 4.1 shows a series of Bloch spheres, each a snapshot during a dephasing and rephasing process. First, a  $\pi/2$  pulse creates an atomic coherence in an inhomogeneously broadened transition which drives all Bloch vectors to the xy-plane with an initial phase of  $\gamma = 0^\circ$ . Note that the phase  $\gamma$  is defined by the phase of the driving field, as described in the previous chapter. Now, the coherences follow a free evolution and the Bloch vectors fan out on the Bloch sphere, caused by their different transition frequencies with respect to the rotating frame of the Bloch sphere, i.e., the center frequency of the inhomogeneous line. After a waiting time  $\tau_1$ , a  $\pi$  pulse (with the same phase as the initial  $\pi/2$  pulse) flips the Bloch vectors by  $180^\circ$  around the torque vector axis to the other side of the Bloch sphere. As the phases still evolve with the same speed as before, the coherences start to rephase. After a total time  $2\tau_1 + \tau_\pi$ , all Bloch vectors point into the same direction, i.e., all coherences are in phase and interfere constructively. This revival of the macroscopic coherence is called spin echo. Note that the overall phase of the macroscopic coherence was shifted by  $180^\circ$  during the rephasing process, but a second rephasing pulse can be used to restore the original phase.

This simple rephasing experiment shows that dephasing is a reversible process, as long as the phase evolution is constant in time for all individual coherences. This is necessary because the Bloch vectors need to rotate back their phase during the time after the  $\pi$  pulse by exactly the amount they have collected before the

rephasing  $\pi$  pulse during the time  $\tau_1$ . Furthermore, rephasing relies on a  $\pi$  flip of Bloch vectors around the torque vector axis. In the above example, we chose the flip axis to be aligned with the  $\text{Re}[\rho_{12}]$  axis, i.e., the relative phase between rephasing  $\pi$  pulse and the initial  $\pi/2$  pulse was zero. In fact, every rotation axis in the  $xy$ -plane of the Bloch sphere could be used to rephase coherences by a single  $\pi$  pulse, whereat the choice of the rotation axis, i.e., the phase of the rephasing  $\pi$  pulse, defines the phase of the spin echo. The application of a second, identical  $\pi$  pulse restores the initial phase.

### 4.1.1 Limitations of $\pi$ Pulse Based Rephasing

Rephasing by  $\pi$  pulses is the most simple way to rephase coherences in an inhomogeneously broadened transition. However, the use of these pulses relies on resonant interaction and the strict requirement of a pulse area  $\mathcal{A} = \pi$ . In inhomogeneously broadened media, rephasing pulses need to be spectrally broad enough to cover all detuned two-level systems in order to guarantee resonant interaction with all transitions. In practice, this requires pulses with a sufficiently high Rabi frequency at short pulse durations. If the rephasing pulse is detuned from resonance, the pulse area is calculated from the effective Rabi frequency. Thus, the pulse area changes with the detuning and can never be perfectly adjusted for all systems at the same time. The error, i.e., the angle between a restored Bloch vector in an experiment and the ideally rephased Bloch vector scales with  $(\Delta/\Omega)^2$  for a rectangular shaped pulse [68]. Thus, a  $\pi$  pulse can never be perfect, unless its Rabi frequency is very high compared to the inhomogeneous broadening. However, the Rabi frequency is limited due to available driving field power. Another possible reason for imperfect rephasing is an inaccurate setting of pulse parameters to achieve the correct pulse area. This can result from unknown experimental influences or technical limitations such as discretisation in digital control parameters. In the worst case, the pulse parameters are subject to noise and the pulse area requirement is only manageable up to a certain limit.

As rephasing of atomic coherences is the basis for efficient and long-lasting coherence storage and thus also for light storage experiments, it is inevitable to design pulses that overcome the above mentioned difficulties of simple  $\pi$  pulses. This problem becomes even more important when not only one, but up to thousands of pulses are used in dynamical decoupling sequences in order to compensate for decoherence [28, 29]. Then, even very small errors add up and inhibit efficient rephasing and storage, respectively. Adiabatic pulses on the other hand offer a robust and efficient approach to rephasing, which is independent on pulse parameter fluctuations in a wider range, as discussed in the next section.

## 4.2 Adiabatic Interaction with a Two-State System

So far, we described coherent interactions in a two-state system in the basis of states  $|1\rangle$  and  $|2\rangle$ . Equivalent to our considerations for a driven three-state system

(see chapter 3.2), these states are no longer eigenstates when a driving field interacts with the two-state system. This is indicated by the off-diagonal entries of the Hamilton operator given in equation (3.7). Taking every instant of time  $t$  as a constant parameter, the new, *instantaneous* eigenvalues  $\epsilon_{\pm}$  and eigenfunctions  $|\psi_{\pm}\rangle$  of the two-state system are obtained from the diagonalized Hamiltonian to [60]

$$\begin{aligned} |\psi_{+}\rangle &= \sin\beta|1\rangle + \cos\beta|2\rangle \\ |\psi_{-}\rangle &= -\cos\beta|1\rangle + \sin\beta|2\rangle \end{aligned} \quad (4.1)$$

and

$$\begin{aligned} \epsilon_{+} &= \frac{\hbar}{2}\sqrt{\Omega^2 + \Delta^2} \\ \epsilon_{-} &= -\frac{\hbar}{2}\sqrt{\Omega^2 + \Delta^2} \end{aligned} \quad (4.2)$$

where the mixing angle  $\beta$  is defined by

$$\tan\beta = \frac{\Delta}{\Omega} + \sqrt{1 + \frac{\Delta^2}{\Omega^2}} \quad (4.3)$$

The new Hamiltonian is diagonal in the basis of the instantaneous eigenfunctions for any instant of time  $t$ . However, when temporal evolution is taken into account, i.e., when  $\Omega$ ,  $\Delta$  and consequently  $\beta$  become functions of time, a coupling between the two eigenfunctions appears and the Hamilton operator reads [23, 60]

$$\hat{H} = \begin{pmatrix} \epsilon_{+} & -i\hbar\dot{\beta}(t) \\ i\hbar\dot{\beta}(t) & \epsilon_{-} \end{pmatrix} \quad (4.4)$$

This coupling is negligible, provided that

$$|i\hbar\dot{\beta}(t)| \ll |\epsilon_{+} - \epsilon_{-}| \quad (4.5)$$

If condition (4.5) is fulfilled, there is no coupling between the two instantaneous eigenstates. Therefore, the system will stay in the state it was initially prepared, as long as  $\beta$  changes slowly enough in time, which is why these states are called *adiabatic* states, whereas the original states  $|1\rangle$  and  $|2\rangle$  are often called *diabatic* states. Condition (4.5) is called *adiabaticity criterion*, which transforms with equation (4.2) and (4.3) into

$$1 \gg \frac{1}{2} \left| \frac{\dot{\Omega}(t)\Delta(t) - \Omega(t)\dot{\Delta}(t)}{(\Omega^2(t) + \Delta^2(t))^{3/2}} \right| \quad (4.6)$$

This condition signifies that the coupling between two adiabatic states is negligible, if the temporal change of  $\Delta$  or  $\Omega$  is slow compared to the effective Rabi frequency  $\Omega_{\text{eff}}^2 = \Omega^2 + \Delta^2$ . We consider a pulse with a linear chirp rate  $r = \Delta_{\text{max}}/\tau_{\text{D}}$ , where  $\tau_{\text{D}}$  is the pulse duration of the driving field and  $\Delta_{\text{max}}$  is the symmetric chirp

range around resonance. When the pulse is resonant and has a Rabi frequency  $\Omega_{\max}$ , condition (4.6) reduces to a lower boundary for the adiabaticity criterion

$$\frac{\Omega_{\max}^2}{r} \gg 1 \quad (4.7)$$

Note that each adiabatic state in (4.1) involves the two diabatic states and following a single adiabatic state under a slowly varying mixing angle  $\beta$  exhibits some interesting features, because  $\beta$  also defines to which fraction the diabatic states contribute to the adiabatic state. As an important consequence, it is possible to transfer a system from state  $|1\rangle$  to state  $|2\rangle$  via a single adiabatic state. Note that the transfer is not accomplished via diabatic coupling, i.e., Rabi oscillations during a specific time. The transfer happens by slowly varying the mixing angle  $\beta$ , induced by varying  $\Delta$  and  $\Omega$ , respectively. Adiabatic and diabatic evolution of a system can be considered as two limiting cases. Diabatic interaction enables fast control of the system with the requirement of well defined pulse parameters. Adiabatic coupling on the other hand is slow, but allows a loose definition of parameters in certain limits imposed by condition (4.6).

If the system is prepared in a superposition of adiabatic states, their relative phase evolution has to be taken into account. The temporal evolution of these phases just depends on the eigenenergies  $\epsilon_{\pm}$  and a superposition state  $|\psi(t)\rangle$  reads

$$|\psi(t)\rangle = c_+ e^{-\frac{i}{\hbar}\epsilon_+ t} |\psi_+\rangle + c_- e^{-\frac{i}{\hbar}\epsilon_- t} |\psi_-\rangle \quad (4.8)$$

with the probability amplitudes  $c_{\pm}$ .

### 4.2.1 Rapid Adiabatic Passage

The previous section introduced adiabatic interactions, i.e., the coupling of a two-state system, when the driving field varies its parameters slowly with time compared to its effective Rabi frequency. A common adiabatic technique is *rapid adiabatic passage* (RAP), which enables efficient population transfer between two diabatic states [23, 71], as well as rephasing of atomic coherences [68–70]. In order to describe the properties of rapid adiabatic passage, we first consider population transfer.

We assume our system to be in the diabatic state  $|1\rangle$ . A pulsed interaction field is present which has a positive linear chirp rate  $r$ , i.e., the detuning  $\Delta(t)$  changes linearly from  $-\Delta_{\max}/2$  to  $+\Delta_{\max}/2$  across resonance. The temporal distribution of the Rabi frequency  $\Omega(t)$  is Gaussian shaped (see figure 4.2, lower graph). Initially the Rabi frequency  $\Omega$  is zero and the detuning is  $\Delta(t) = -\Delta_{\max}/2$ . Consequently,  $\beta = 0$  and the system is only in state  $|\psi_-\rangle = |1\rangle$ . As the system is in a single adiabatic state, we can neglect the relative phase between the two adiabatic states as given in equation (4.8). We assume that the Gaussian envelope of the Rabi frequency varies slowly enough in time to fulfill condition (4.6). Figure 4.2 (upper graph) shows the temporal shape of the (unitless) Rabi frequency  $\Omega = 1$  and the

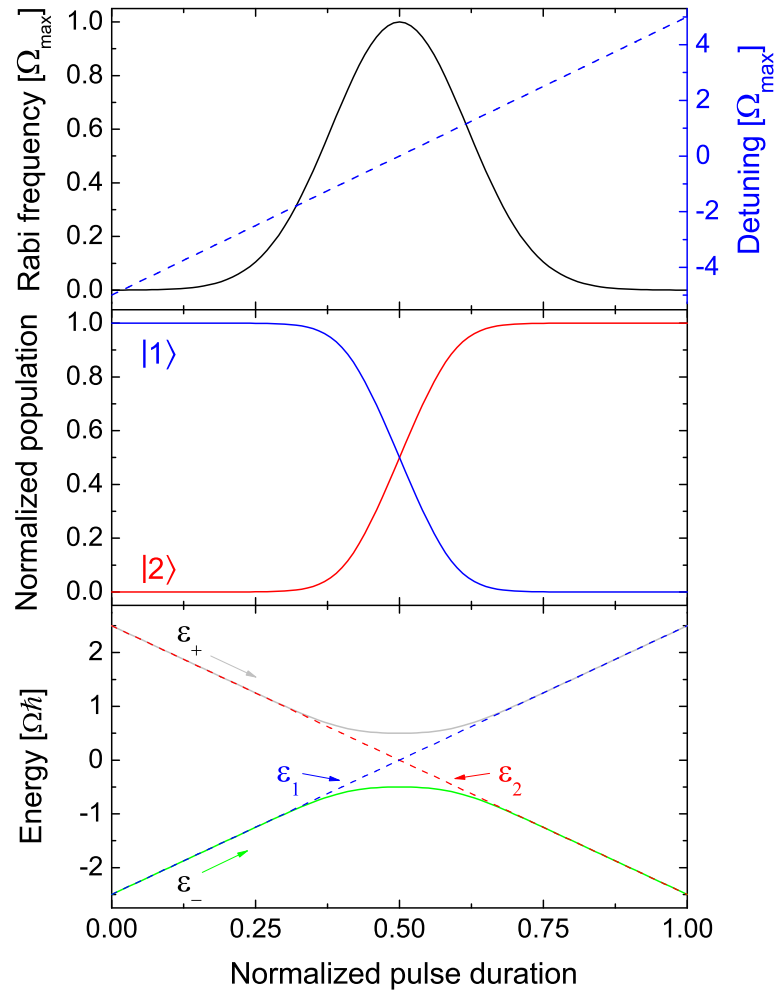


Figure 4.2: (Upper graph) Rabi frequency and detuning of a RAP pulse. (Center graph) Simulation of the population in the diabatic states  $|1\rangle$  and  $|2\rangle$  during this specific RAP pulse. (Lower graph) Energies  $\epsilon$  of diabatic and adiabatic states during the RAP pulse.

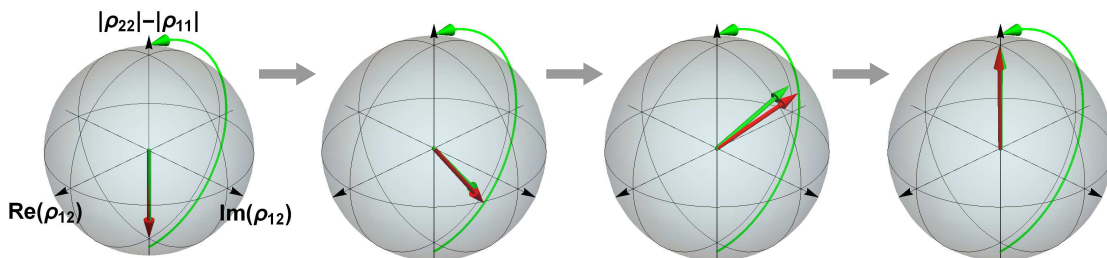


Figure 4.3: Bloch vector simulation of population inversion between states  $|1\rangle$  and  $|2\rangle$  driven by a RAP pulse as shown in figure 4.2. The Bloch vector is depicted in red, the torque vector is depicted in green.

total chirp range  $\Delta_{\max} = 10 \times \Omega$ . The center graph shows the population distribution among states  $|1\rangle$  and  $|2\rangle$  and the lower graph shows the development of adiabatic eigenenergies as well as the energies of the diabatic states during the RAP pulse. The simulation shows that RAP drives a complete, smooth population transfer from state  $|1\rangle$  to state  $|2\rangle$ . The adiabatic following of state  $|\psi_{-}\rangle$  guarantees that the system stays in exactly this specific state. However, in contrast to the beginning of the pulse, the detuning is positive at the end of the pulse and the Rabi frequency is again zero. Thus,  $|\psi_{-}\rangle$  is equivalent to state  $|2\rangle$  at the end of RAP. During the interaction, no oscillations, i.e., a typical indicator of diabatic coupling, occur and consequently, the system follows only one eigenenergy, i.e.,  $\epsilon_{-}$  (corresponding to the eigenstate  $|\psi_{-}\rangle$ ), initially equal to the energy of state  $|1\rangle$  and at the end to the energy of state  $|2\rangle$  (see figure 4.2, lower graph).

It is convenient to consider population transfer by a RAP pulse on the Bloch sphere. Figure 4.3 shows a sequence of snapshots during a RAP pulse acting on a two-state system. Note that we use all parameters as in the above described scenario. The Bloch vector points in the  $-z$  direction, i.e., all population is in state  $|1\rangle$ . So does the torque vector at the beginning of the interaction, because  $\Delta$  is negative but  $\Omega \rightarrow 0$ . During RAP, the torque vector moves to the north pole of the Bloch sphere and the Bloch vector follows this trajectory according to equation (3.19). However, the Bloch vector can only follow exactly to the north pole, if the torque vector changes its position slowly enough, i.e., adiabatically. If the adiabaticity condition holds true, the system ends up in state  $|2\rangle$ , i.e., RAP has driven a population inversion.

It is important to note that the transfer was achieved by varying the mixing angle  $\beta$  slowly in time. However, the change of the value of  $\beta$  during the interaction is not tied to any strict conditions. In fact, the change happens under rather loose conditions as long as it is adiabatic and the initial and final state is well defined. In particular, RAP works for an inhomogeneously broadened system, if the initial detuning is large for all transitions.

According to the above considerations, RAP pulses should have a large initial and final detuning compared to the initial and final Rabi frequency. The square of the Rabi frequency close to resonance should be high enough compared to the chirp rate. In addition, both parameters shall vary slowly, i.e., adiabatically in time. The exact values of  $\Omega$  and  $\Delta$  are not of importance. These loose conditions make RAP pulses quite robust against fluctuations or potential wrong settings of experimental parameters.

### 4.3 Rephasing by Rapid Adiabatic Passage

The last chapter discussed population inversion by a RAP pulse and showed that a RAP pulse inverts a system similar like a  $\pi$  pulse (compare figures 4.3 and 3.2). Rephasing of atomic coherences likewise relies on a  $\pi$  flip of a two-state system. However, in rephasing, the behaviour of RAP and  $\pi$  pulses is different, which results from different initial and final positions and trajectories of the respective torque vector during the pulse.

We will first discuss the effect of a single RAP pulse applied to an atomic coherence to understand benefits and disadvantages from the result. Figure 4.4 shows the corresponding Bloch vectors in an inhomogeneously broadened ensemble carrying the atomic coherences, as well as their trajectories during a single RAP rephasing pulse. Note that the blue vector represents the ensemble, whose transition frequency is resonant with the center frequency of the inhomogeneous line. The red vectors are the Bloch vectors which are detuned from this resonance. Initially, the system is prepared in a maximum coherent superposition of the two diabatic states, i.e.,  $\rho_{12} = i/2$ . Note that we assume  $\gamma = 0$  and thus all Bloch vectors point along the  $\text{Im}[\rho_{12}]$  axis of the Bloch sphere.

For the simulation we use the same RAP pulse as for the population inversion, i.e., a pulse with Gaussian shaped temporal evolution of the Rabi frequency and with a linear, positive chirp rate (compare figure 4.2, upper graph). The inhomogeneously broadened ensemble has an assumed rectangular shape and a width equal to the Rabi frequency  $\Gamma_{\text{inh}} = \Omega$ .

First, the system evolves freely for a time  $\tau_1$ , leading to dephasing of the Bloch vectors (figure 4.4, (1)). After the time  $\tau_1$ , we simulate the influence of a RAP pulse (figure 4.4 (2)). The torque vector initially points to the south pole of the Bloch sphere. In contrast to the previous example of population transfer, the Bloch vectors have only a perpendicular component to the torque vector and according to equation (3.19), they start to rotate around the z-axis, i.e., the direction of the torque vector (depicted by the green arrow in figure 4.4 (2)). This rotation includes also the resonant ensemble (depicted by the blue Bloch vector). The rotation speed is dependent on the effective Rabi frequency and thus depends on the individual detuning of a system within the inhomogeneously broadened line or the corresponding transition frequency, respectively. This is why each ensemble that carries a coherence performs a different rotation on the Bloch sphere, dependent on its spectral position in the inhomogeneous line.

As the RAP pulse temporally progresses, the torque vector moves to the north pole of the Bloch sphere. The Bloch vectors follow this movement accompanied by the above described rotation in a plane, whose surface normal is defined by the torque vector. At the end of the RAP pulse, the Bloch vectors have been subject to two types of transformation. They have undergone a  $\pi$  pulse like flip on the Bloch sphere, which is superposed with an additional rotation around the torque vector axis. During the latter, each Bloch vector accumulates a distinct, individual phase until the end of the pulse, which depends on the RAP pulse area, or in other words, the number of rotations on the Bloch sphere around the torque vector axis. However, the RAP pulse exhibits a different detuning (and effective Rabi frequency) for individual ensembles within the inhomogeneous line. Thus their individual phases after RAP are different as well.

This can be seen best for the blue Bloch vector, representing the central ensemble in the inhomogeneous linewidth. Before the RAP pulse, it had a phase  $\gamma = 0^\circ$ , however, after the pulse, it has a non-zero phase and points in a different direction on the Bloch sphere (compare figure 4.4 (1) and (3)). In the subsequent, free temporal evolution (see figure 4.4 (3)), this vector will not move its position, because



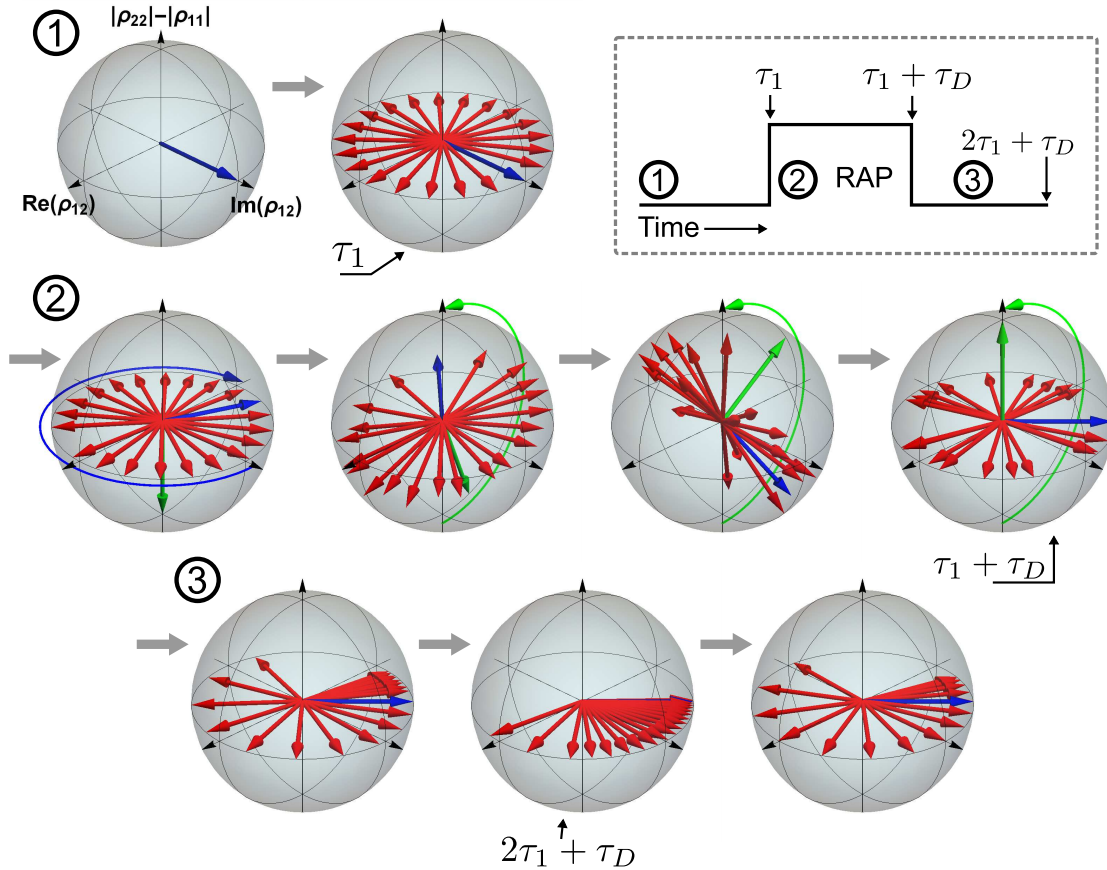


Figure 4.4: Simulation of Bloch vectors (red) for an inhomogeneously broadened transition carrying atomic coherences. The temporal sequence is shown in the gray dashed box. (1) The coherences dephase during free evolution. (2) A RAP pulse with duration  $\tau_D$  acts on the systems. (3) A second period of free evolution for time  $\tau_1$ . The blue vector represents the central ensemble in the inhomogeneous line. The torque vector is depicted in green color. Parameters for the simulation are the same as in section 4.2.

it is the resonant Bloch vector for the Bloch sphere. Here, we can already identify the problem with a single RAP pulse acting on atomic coherences, i.e., the Bloch vectors have collected a distinct phase and do not point in the same direction as initially and thus imperfect or no rephasing occurs. After the free evolution for a time  $\tau_1$  after the RAP pulse, the Bloch vectors reach a minimum deviation, but still, they point into different directions, i.e., they still possess a phase distribution collected during the RAP pulse. Indeed, the influence of free evolution has been reversed, but the RAP pulse itself introduced an additional, transition frequency dependent dephasing.

Winter et al. [68] give an analytical calculation of the phase after a single RAP pulse which shows the dependency on the pulse area  $\mathcal{A}$ , and the (constant) phase  $\phi$  of the driving field of the RAP pulse. Just like a  $\pi$  pulse, the phase of the rephasing RAP pulse defines an axis for the  $\pi$  flip. It thus contributes to the phase after a single RAP. For a coherence in the  $j$ th ensemble in the inhomogeneous line with a detuning from the central frequency  $\Delta_j$ , the full expression for the relative

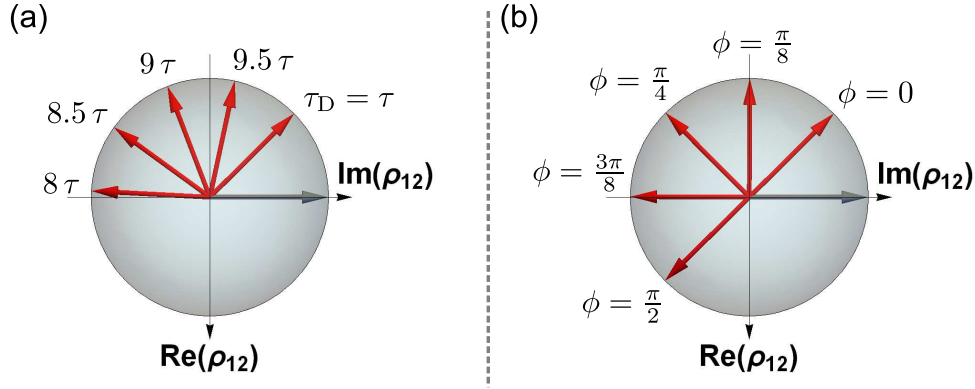


Figure 4.5: Simulation of Bloch vector (red) positions for atomic coherences after single RAP pulses with (a) different pulse durations  $\tau_D$  or (b) different driving field phases  $\phi$ . Only the xy-plane of the Bloch sphere is shown. The Bloch vector of the initial coherence is depicted in gray.

phase change  $\Delta\gamma(j)$  reads

$$\Delta\gamma(j) = \mathcal{A}_j - 2\phi + \Delta_j (\tau_1 - \tau_2) \quad (4.9)$$

where

$$\mathcal{A}_j = \int_0^{\tau_D} \sqrt{(\Omega^2(t) + \Delta_j^2(t))} dt \quad (4.10)$$

Figure 4.5 (a) and (b) show simulations of Bloch vectors after a single RAP pulse for a varying pulse duration and a varying phase of the RAP pulse. In both cases, the initial coherence had a phase of  $\gamma = 0^\circ$ . The simulations clearly show, how the pulse duration or the phase of the RAP pulse affects the phase of the coherence, i.e., the position of the Bloch vector in the xy-plane. Concluding, only imperfect rephasing is performed by a single RAP pulse, i.e., it is unsuitable for rephasing.

### 4.3.1 Rephasing with Two RAP Pulses

Inefficient rephasing by a single RAP pulse can be overcome by the use of a second RAP pulse. The latter statement is actually valid for any pulse that works for population inversion [72]. Note that also for a single  $\pi$  pulse, this statement is valid, because technically, rephasing after a single pulse is imperfect due to an overall  $\pi$  phase shift. The accumulated phase  $\Delta\gamma(j)$  after two RAP pulses according to [68] is calculated by

$$\Delta\gamma(j) = \mathcal{A}_1 - \mathcal{A}_2 - 2\phi_1 + 2\phi_2 + \Delta_j (\tau_1 - \tau_2 + \tau_3) \quad (4.11)$$

where the subscripts 1 and 2 refer to the first and second RAP pulse. The last term contains the free evolution duration for a system with a static detuning  $\Delta_j$  from the center of the inhomogeneous line.  $\tau_1$  represents the time before the first RAP pulse,  $\tau_2$  between the two pulses and  $\tau_3$  after the second RAP pulse.

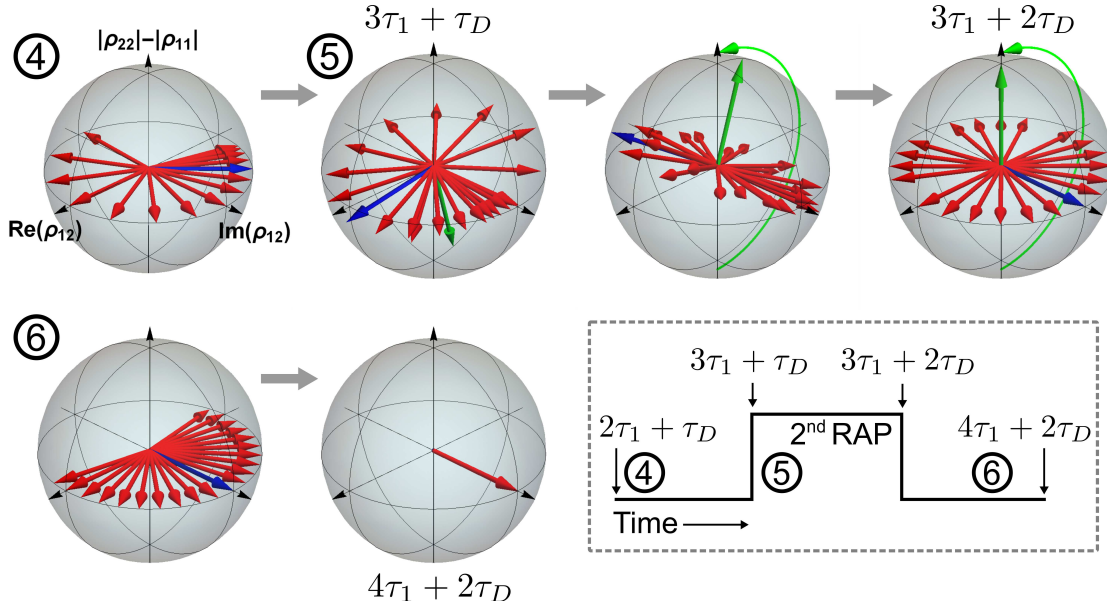


Figure 4.6: Simulation of a second RAP pulse acting on coherences as shown in figure 4.4, after step (3), i.e., after a first RAP pulse at time  $2\tau_1 + \tau_D$ . (4) The coherences continue to dephase. (5) A second RAP, identical to the first, acts on the Bloch vectors. (6) The coherences rephase. Bloch vectors are colored in red, the blue vector is resonant with the rotating frame of the Bloch sphere, the torque vector has a green color. The temporal sequence is shown in the gray dashed box.

The easiest way to make  $\Delta\gamma_j$  equal to zero (for non-vanishing  $\tau_i$ ) is the use of two identical RAP pulses and the choice of  $\tau_3 = \tau_2 - \tau_1$ , which is fulfilled for the simple case  $\tau_3 = \tau_1$  and  $\tau_2 = 2\tau_1$ . Note that the latter condition is also mandatory for  $\pi$  pulse based rephasing. Starting from the last snapshot in figure 4.4, figure 4.6 shows the influence of the second RAP, which perfectly rephases the initial coherences.

Taken into account the above discussion, it becomes clear that a pair of identical RAP pulses is perfectly suitable to rephase atomic coherences. In particular, the second RAP compensates all individual phases, accumulated during the first RAP and thus each coherence is rephased to its initial position on the Bloch sphere, independent from its detuning. Thus RAP based rephasing offers a robust and broadband alternative for  $\pi$  pulse based rephasing.

RAP based rephasing can also be understood in the picture of the adiabatic states. Starting from the mentioned initial condition, we find the system in the state (see section 4.2)

$$|\psi(t)\rangle = c_+ e^{-\frac{i}{2}\Omega_{\text{eff}}t} |\psi_+\rangle + c_- e^{+\frac{i}{2}\Omega_{\text{eff}}t} |\psi_-\rangle \quad (4.12)$$

The fact that both adiabatic states are involved in the description of the system involves also the phase evolution of each adiabatic state, given by the exponential factor in the above equation. This relative phase evolves with the effective Rabi frequency and adds an additional, time-dependent phase to the otherwise constant probability amplitudes  $c_{\pm}$ . Note that  $c_{\pm}$  are constant, because we change the

system adiabatically. Hence, we find two temporal evolutions again: The adiabatically changing mixing angle  $\beta$  and a superposed phase oscillation, given by the effective Rabi frequency. The change of  $\beta$  results in an inversion of the probability amplitudes of states  $|1\rangle$  and  $|2\rangle$  within every adiabatic state. The relative phase evolution of the adiabatic states other on the other hand adds a distinct phase that depends on the pulse duration and the effective Rabi frequency. Thus after a first pulse, the system ends up with a distribution of phases, just as discussed above. If the diabatic probability amplitudes are  $c_1 = c_2 = 1/\sqrt{2}$ , this just changes the phase of the coherence, i.e.,  $|c_j|$  are constant. After the second pulse, the relative phase evolution is reversed (because the system evolves with inverted probability amplitudes of the diabatic states) and the system has been inverted for a second time to its original state with its original phase.

The latter two sections described extreme initial conditions, i.e., a maximum superposition at equally distributed population and a maximum population difference. However, every other initial condition is just a combination of these two cases and a pair of RAP pulses rephases also non-maximum coherences and the population is inverted after each RAP.

To conclude the results of the above considerations, RAP seem most suitable to fulfill the tasks of population inversion and rephasing of atomic coherences. RAP is easy to implement, e.g., by applying a chirp and a temporal evolution of the Rabi frequency that fulfills the adiabaticity criterion. Apart from this, no other strict requirements confine the adiabatic pulses, i.e., they are robust against a variety of possible errors, such as power fluctuations, technical uncertainties concerning pulse duration, Rabi frequency or frequency detuning. Especially the latter enables rephasing in inhomogeneously broadened media, because RAP based rephasing acts on all systems, independent from their detuning without loss of efficiency. In particular in comparison with the commonly used  $\pi$  pulses this is beneficial, as  $\pi$  pulses are not robust to parameter fluctuations and are highly dependent on detuning. Section 4.5 presents an experimental examination of RAP pulses used for rephasing and compares the latter to rephasing by  $\pi$  pulses.

## 4.4 Experimental Setup

In order to perform experiments, which allow light storage and rephasing by RAP and  $\pi$  pulses, the setup must provide optical fields, i.e., a control and a probe beam and an additional driving field in order to generate the rephasing pulses. The frequency of the latter field has to be in the radio-frequency regime in order to couple to the hyperfine ground states in PrYSO, which carry the atomic coherences. This section first introduces the generation of optical and RF fields for our experiment, as well as the method of detection of the light storage signal. Subsequent to the experimental setup, it describes the necessary steps in order to prepare the storage medium for an experiment and presents the complete measurement sequence.

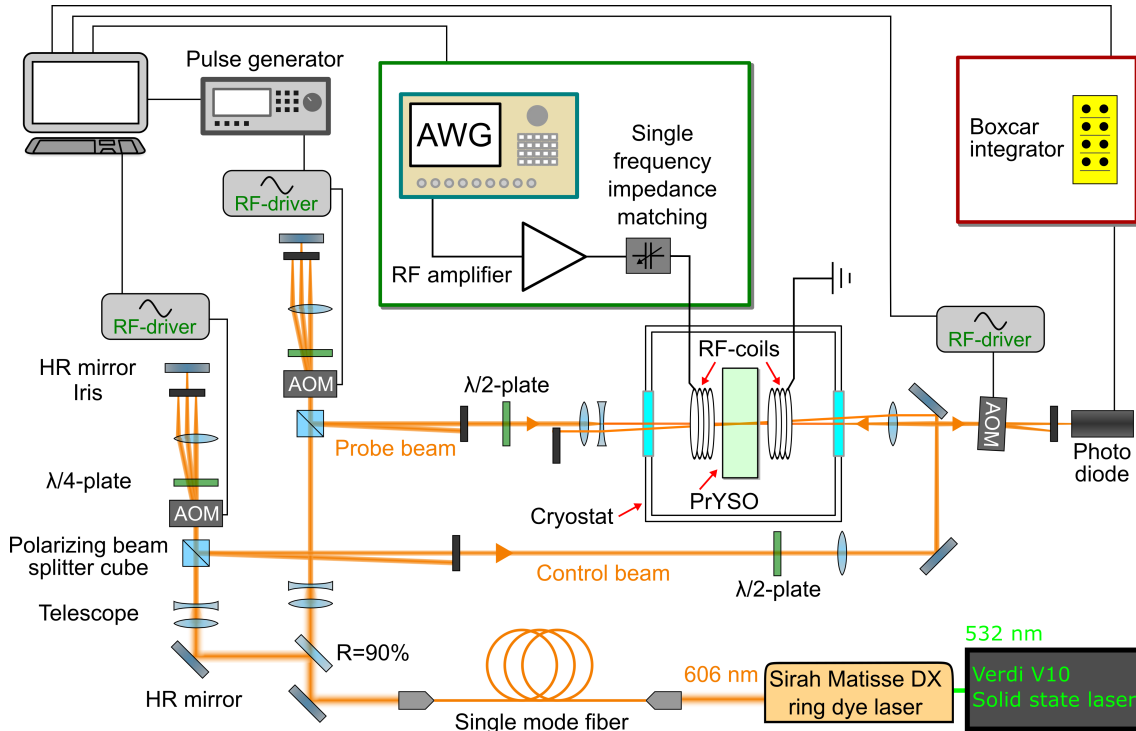


Figure 4.7: Schematic experimental setup, consisting of optical setup, RF setup (green box) and a detection unit for stored light pulses (red box and photo diode). Black lines represent transmission lines for electronic signals, orange lines represent the laser beam.

#### 4.4.1 Crystal and Cryostat

Figure 4.7 shows the complete experimental setup, used for light storage and rephasing experiments. The central part of the setup is the storage medium, a praseodymium doped YSO crystal (Scientific Materials, dimensions of 5x5x3 mm), where 0.05% of the Yttrium ions are replaced by praseodymium ions (see chapter 1). The crystal has an optical depth of  $OD \approx 6$ .

It is attached to the cold finger of a liquid helium flow cryostat (Janis Research, ST-100). The cryostat cools the crystal to  $T \approx 4\text{K}$  with a cooling power of 3W. Before the cryostat is cooled down, a rotary valve and a turbo pump evacuate the cryostat to a pressure of  $p \approx 10^{-6}$  mbar. Additional information on how the crystal is mounted inside the cryostat can be found in [73].

#### 4.4.2 Optical Setup

A ring dye laser system (SIRAH, Matisse-DX) provides cw optical radiation at a wavelength  $\lambda = 606\text{nm}$  to drive the relevant optical transition in PrYSO. The output power of the laser system is around  $P = 1\text{W}$ , which is frequency stabilized by an external stabilization unit to  $\Delta\nu \approx 100\text{kHz}$  on a time scale of  $\Delta t = 100\text{ms}$ . Note that the OPO-SFG laser system was not yet available for experiments with RAP.

The output radiation is guided to the experiment via a single mode fiber, whereat mainly reflection losses at the fiber ports reduce the available power after

the fiber to  $P \approx 500$  mW. The laser beam after the fiber has a Gaussian shaped spatial profile. Because light storage requires two radiation fields, a mirror with 90% reflectivity splits the beam into a weak probe (or signal) beam, and a strong control beam. The two beams are each guided through an acousto-optical modulator (Brimrose, BRI-VFF-80-50-V-B1-F1) in double-pass configuration in order to enable amplitude and frequency modulation in a range of  $\Delta\nu_{\text{AOM}} = \pm 50$  MHz around the AOM central frequency  $\nu_{\text{AOM}} = 80$  MHz. In particular, the AOM are used to produce pulses at relative, shifted frequencies from the cw, monochromatic beams. The AOM are driven with RF waves from direct digital synthesis (DDS) drivers (AA Opto-Electronic, DDSPA-B8b23b-0 for the control AOM, and Crystal Technologies, AODS 20160-1 for the probe AOM). A polarizing beam splitter cube (PBSC) before the AOM assures a horizontal linear polarization of the incoming light.

The maximum power which is available after the AOM is  $P_C \approx 100$  mW in the control beam line and  $P_p \approx 4$  mW in the probe beam line.

The two beams are guided counter propagating to the crystal as indicated in figure 4.7, whereat there is a small angle between probe and control beam. Both assures that the strong control field does not reach the photo diode at any time and in particular during the readout process. Thus this setup avoids unwanted signals during the detection of the weaker probe beam.

Inside the crystal, the Gaussian shaped probe and control beam overlap and are mildly focused to a FWHM diameter of  $d_p = 150$   $\mu\text{m}$  and  $d_C = 220$   $\mu\text{m}$ . This provides Rabi frequencies of  $\Omega_p = 2\pi \times 280$  kHz and  $\Omega_C = 2\pi \times 950$  kHz.

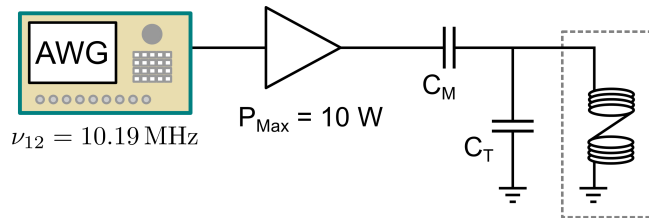
### 4.4.3 Generation of Radio-Frequency Magnetic Fields

Besides the optical fields used for light storage, rephasing experiments require pulses in the radio-frequency domain in order to manipulate atomic coherences in the hyperfine ground state transitions of PrYSO. In a light storage experiment, the atomic coherences are prepared in the hyperfine ground state transition  $|\pm 1/2\rangle \leftrightarrow |\pm 3/2\rangle$  with a frequency of  $\omega = 2\pi \times 10.19$  MHz.

In order to generate an RF magnetic field that couples to this transition, we use a pair of RF coils, which are placed around the PrYSO crystal inside the cryostat. Each coil carries 7 windings of copper wire with a diameter of  $d = 200$   $\mu\text{m}$ . The diameter of each coil is  $d = 5$  mm, the length is  $l = 2$  mm and the coils are separated by 3.4 mm. Note that we use these coils in all experiments, if not indicated otherwise. Figure 4.7 (green box) depicts the setup used for the RF magnetic field generation. The RF wave that is sent to the coils, is initially generated in an arbitrary wave form generator (Tektronix, AWG 5014). The AWG provides full frequency, amplitude and phase control of the generated RF wave with a sampling rate of 1.2 GS/s. The AWG output is guided to an RF amplifier (EM Power, 1028-BBM 1C3KAJ) with a maximum output power of  $P_{\text{max}} = 10$  W and a gain of 40 dB in a frequency range between 1 MHz and 500 MHz.

The amplified signal is then sent to the coils inside the cryostat. However, the imaginary and frequency dependent impedance of the coils,  $Z_{\text{RF}} = i\omega L$  is significantly different from the impedance of the RF amplifier,  $Z_{\text{Amp}} = 50$   $\Omega$ . As a

Figure 4.8: Setup for the generation of RF pulses. AWG is an arbitrary waveform generator, the triangle represents an RF amplifier.  $C_T$  and  $C_M$  are capacitors to match the impedance of the RF coils inside the cryostat (indicated by the gray box) to the amplifier.



consequence, the RF wave is reflected from the coils back into the RF amplifier and no or only little RF magnetic field is generated. In order to suppress back reflections and to guarantee a maximum transfer efficiency of the RF wave to the coils, we insert an impedance matching circuit between amplifier and coils as indicated in figure 4.8. It consists of two capacitors, one parallel and one in series to the RF coils inside the cryostat (indicated by the gray dashed box). The basic idea of this circuit is to build a resonance circuit including the RF coils and a tuning capacitor  $C_T$  in order to increase the coupling efficiency for a specific frequency [74]. A matching capacitor  $C_M$  serves to compensate the residual imaginary part of the impedance. Of course this is a simplified idea of the more complex interplay of capacitive, inductive and resistive elements in the circuit. The exact formula to calculate the values of  $C_T$  and  $C_M$  for a frequency to match are given in appendix D. We use tunable capacitors, in order to adjust the circuit very precisely for the frequency  $\omega = 2\pi \times 10.19 \text{ MHz}$ . The adjustment is done with a network analysis tool (mini Radio Solutions, miniVNA) that allows to measure the impedance, or the reflected waves, respectively, of an electronic system. We adjust our matching circuit such that more than 99% of the incident RF wave is coupled into the coils. The maximum achievable Rabi frequency at  $P_{\text{max}} = 10 \text{ W}$  and with the here described setup is  $\Omega_{\text{RF}} \approx 2\pi \times 140 \text{ kHz}$ .

#### 4.4.4 Detection of Stored Light Signals

The last step in our light storage experiment is to detect the retrieved probe beam as indicated in figure 4.7 (photo diode and red box). The restored probe pulse propagates out of the crystal and is detected by a photo diode (New Focus, model 2051). In addition, the optical path to the photo diode passes through another AOM that acts as a gate in order to suppress any signal on the photo diode outside the reading process. The photo diode records a time resolved signal of the retrieved probe beam, which is integrated in a boxcar integrator (Stanford Research Systems, SR 250). The integrated value is finally read and stored by a computer via an AD converter.

#### 4.4.5 Measurement Procedure

In order to perform EIT-based light storage, it is necessary to prepare a  $\Lambda$ -system in the storage medium PrYSO (see chapter 3.2.1). However, the optical transition in PrYSO is subject to inhomogeneous broadening and thus a single frequency laser

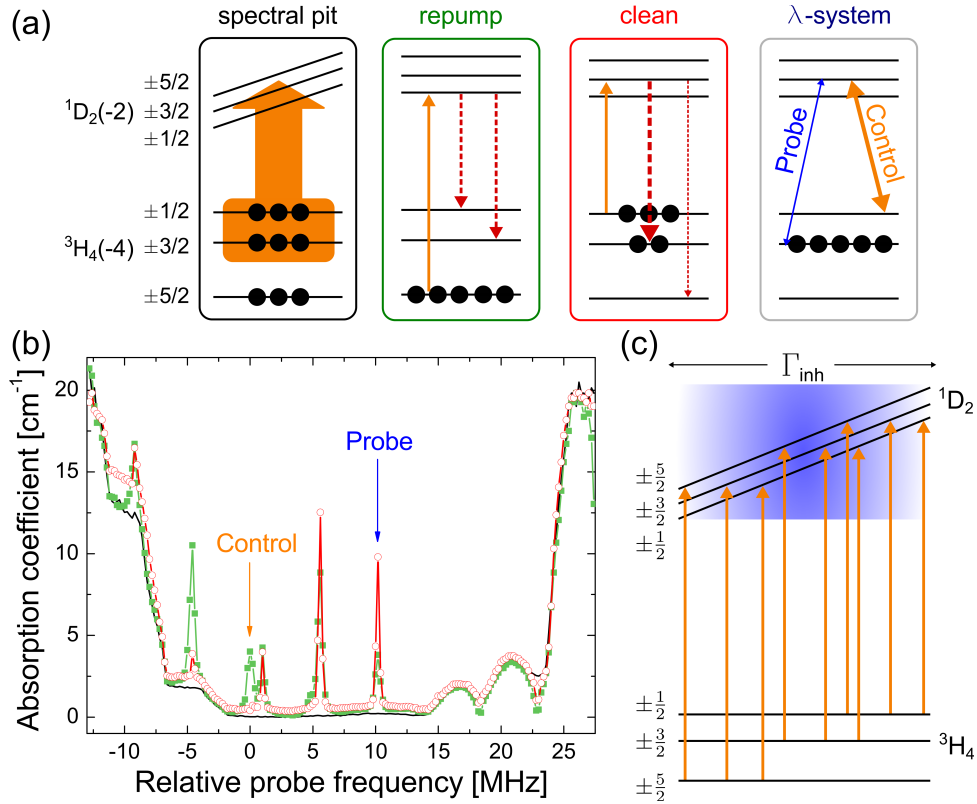


Figure 4.9: (a) Optical pumping scheme for PrYSO to prepare a specific ensemble in the inhomogeneously broadened transition for light storage with a control and a probe beam. (b) Absorption spectra after each preparation step. (c) A single frequency laser beam couples up to nine different transitions in unprepared PrYSO, because the inhomogeneous broadening exceeds the hyperfine splitting by orders of magnitude.

beam couples up to nine different transitions, each in an individual ensemble, as indicated in figure 4.9 (c). Hence, prior to any light storage, the medium has to be prepared in such a way that eight transitions are free of population, and only one transition (or ensemble, respectively) contains population and interacts with the laser pulses.

The preparation used during this work is described in [40, 75] and relies on optical pumping. All pulses have a rectangular profile in time. Figure 4.9 (a) shows the optical pumping scheme used to prepare a specific ensemble for light storage experiments. First, the control laser frequency is chirped in a range of  $\Delta\nu = 18$  MHz over a temporal duration of  $\Delta t = 12$  ms. This process is repeated six times and results in an absorption-free spectral region within the inhomogeneous optical line, the *spectral pit*. Figure 4.9 (b) shows a prepared spectral pit in PrYSO as well as the population distribution after each preparation step. The color code is the same as for the optical pumping scheme in (a). A probe or signal beam with a relative frequency of  $\omega = 2\pi \times 10.19$  MHz is not absorbed inside the pit, i.e., all transitions are depopulated. In order to prepare a single ensemble in  $\Lambda$  configuration, a laser pulse with a fixed frequency  $\nu_R = 22.9$  MHz, i.e., outside the spectral pit, with a duration of  $\Delta t_R = 1.25$  ms and with a power of  $P_R = 65$  mW re-pumps population of one specific ensemble back into previously emptied



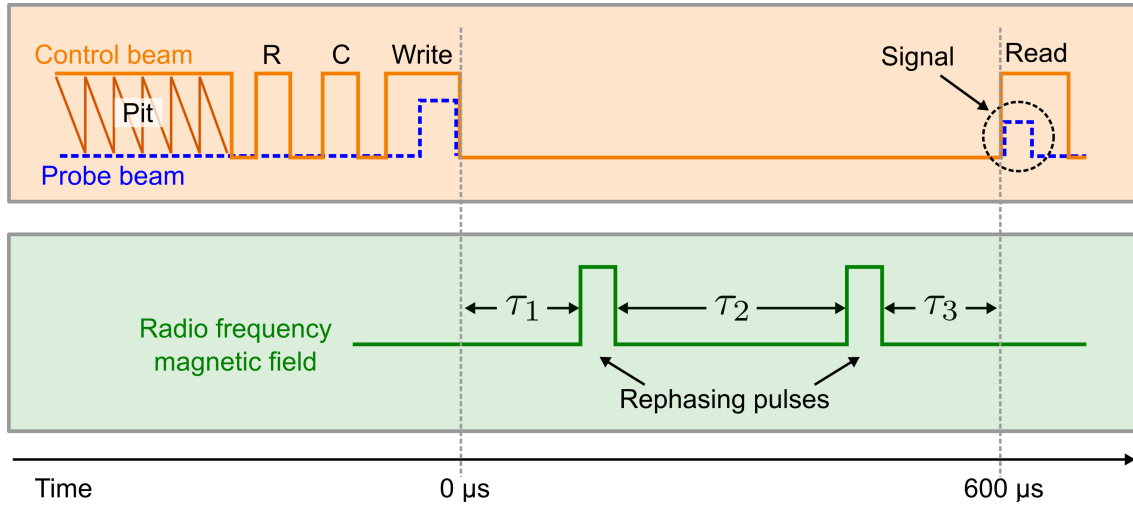


Figure 4.10: (Upper, orange box) Temporal sequence of optical and (lower, green box) RF pulses used for light storage and rephasing of atomic coherences. R is an optical re-pumping, C is an optical cleaning pulse. Rephasing pulses can be  $\pi$  pulses or RAP pulses.

levels. Thereby, absorptions lines appear in the spectral pit again. However, not all population ended up in one state, but is distributed among two states within the specific ensemble. Therefore, a second pulse called *cleaner*, empties this state by optical pumping. It has a relative frequency of  $\nu_{\text{Cl}} = 0$  MHz, a duration of  $\Delta t_{\text{Cl}} = 1.5$  ms and a power of  $P_{\text{Cl}} = 90$  mW. Because of the quite different relative oscillator strength in PrYSO (see table 1.1), almost all population decays into state  $|2\rangle$  of the desired ensemble, as indicated in figure 4.9 and experimentally indicated by an increased absorption at the probe transition frequency after the cleaner. All preparation steps, i.e., spectral pit preparation, re-pumping and cleaning, are separated by a time  $\Delta t \approx 1$  ms, in order to allow full relaxation from the optically excited to the ground state and to assure full decoherence in the ground states.

After this preparation, one specific ensemble provides a  $\Lambda$ -system for EIT-based light storage. In presence of the strong control field, the absorption for the probe field vanishes on resonance as shown by the data in figure 4.11. The system is prepared for an EIT-based light storage experiment.

Figure 4.10 shows the sequence used for light storage (see upper, orange box) and rephasing with RAP and  $\pi$  pulses (see lower, green box). The sequence starts with the optical preparation of the medium as discussed above. After this step the control write pulse is turned on with a power of  $P_{\text{C}} = 140$  mW for a time duration  $\tau_{\text{W}} = 100 \mu\text{s}$ . The control beam creates EIT conditions for the probe pulse which has a duration of  $\tau_{\text{p}} = 20 \mu\text{s}$  and a power of  $P_{\text{p}} \approx 3$  mW. The probe pulse and the control pulse are shut off simultaneously at time  $t = 0 \mu\text{s}$  in order to create a persistent atomic coherence in PrYSO. Note that both probe and control pulse have a rectangular temporal shape, which is not the ideal condition for efficient light storage. However, it is not the goal of this work to yield a maximum storage efficiency, but to investigate rephasing by RAP. Rectangular pulses already yield a well observable light storage signal, which is fully sufficient for this work.

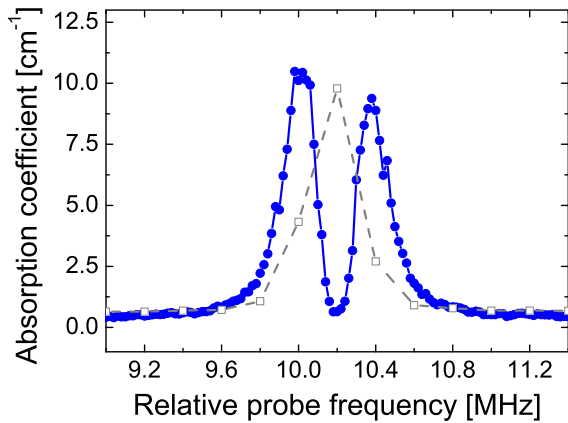


Figure 4.11: EIT absorption spectrum for the probe beam in presence of the control laser (blue, solid circles). The gray hollow squares represent the absorption spectrum in absence of the control beam, i.e., without EIT for the probe beam.

For all experiments, we choose a storage time of  $\Delta\tau = 600 \mu\text{s}$ . This is in the range of the decoherence time  $T_2$  and well above the dephasing time of  $\tau_{\text{deph}} \approx 10 \mu\text{s}$ . The rephasing pulses are centered according to equation (4.11), i.e., the time  $\tau_1$  before the first and the time  $\tau_3$  after the second rephasing pulse is equal, and the time  $\tau_2$  between the two rephasing pulses is the sum of both.

After the rephasing we apply a control read pulse in order to read the rephased atomic coherence and convert it into a probe light field again. The probe light field propagates through the crystal under EIT conditions and is finally detected and processed.

## 4.5 Experimental Results

This section presents the experimental implementation of rapid adiabatic passage based rephasing of atomic coherences. It will give a comparison of RAP and  $\pi$  pulse based rephasing under the systematic variation of experimental parameters, e.g., detuning and Rabi frequency. Also the influence of an inhomogeneous RF magnetic field on rephasing is investigated. Finally, we consider the performance of RAP pulses that operate at the edge of the adiabaticity criterion.

During the experiments we apply either rectangular or Gaussian shaped pulses, whereat we use rectangular pulses if not indicated otherwise. For the RAP pulses, we apply always linear chirps with a total chirp range  $\Delta$ , symmetric around the center of the inhomogeneous line. It is important to note that the single frequency impedance matching has a 3dB bandwidth of around 600 kHz. Thus the RF circuit still allows Rabi frequencies of more than  $\Omega_{\text{max}}/2$  in the range of the maximum used chirp range  $\Delta = 900 \text{ kHz}$ . As a consequence, the rising and falling slopes of a rectangular pulse are still steep, even if the pulse does not exhibit a perfect flat top profile.

### 4.5.1 Rephasing with Limited Rabi Frequency

A common limitation in experimental setups is the maximum achievable Rabi frequency. It is actually the main motivation to replace a  $\pi$  pulse with a RAP pulse in order to rephase atomic coherences in an inhomogeneously broadened system. Covering the inhomogeneous broadening by  $\pi$  pulses requires a high spectral bandwidth or short pulses, respectively. In order to achieve a pulse area of  $\pi$

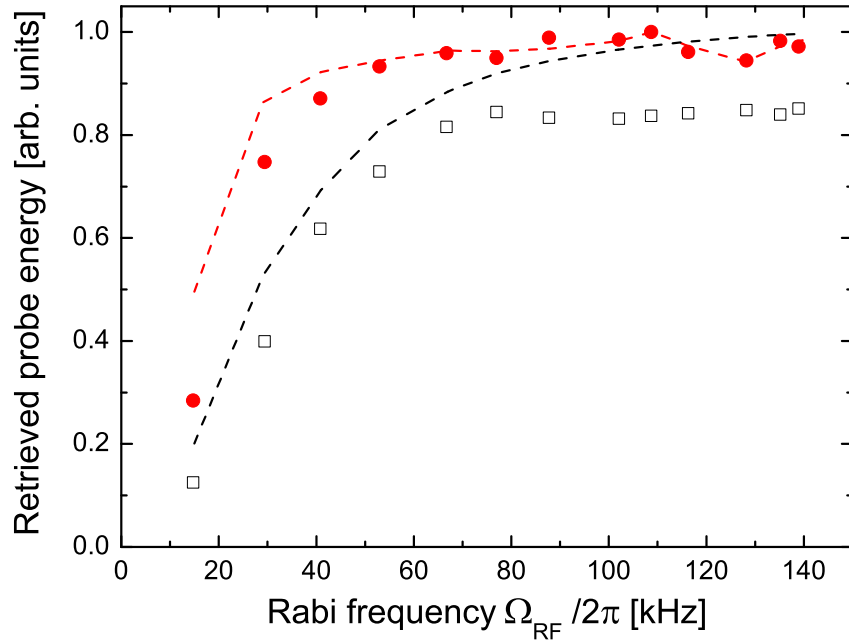


Figure 4.12: Retrieved probe pulse energy for different Rabi frequencies  $\Omega_{\text{RF}}$ , either for rephasing with RAP (red, solid circles) or  $\pi$  pulses (black, hollow squares), optimized for the respective Rabi frequency in order to yield maximum signal. The pulse parameters for each point are given in table 4.1. Red and Black dashed lines show numerical simulations for rephasing with RAP and  $\pi$  using the data in table 4.1 and an inhomogeneous broadening of  $\Gamma_{\text{inh}} = 44$  kHz.

Table 4.1: Experimental parameters for rephasing by  $\pi$  pulses and RAP, as relevant for the single data points and simulations in figure 4.12.  $\Omega_{\text{RF}}$  is the Rabi frequency,  $\tau_{\pi}$  and  $\tau_{\text{RAP}}$  are pulse durations of  $\pi$  and RAP pulses,  $\Delta$  is the total chirp range, and  $\Omega_{\text{RF}}^2/r$  is the simplified adiabaticity criterion.  $\beta$  is the initial mixing angle given by equation (4.3).

$\Omega_{\text{RF}}/2\pi$ [kHz]	$\tau_{\pi}/\mu\text{s}$	$\tau_{\text{RAP}}/\mu\text{s}$	$\Delta$ [kHz]	$\frac{\Omega_{\text{RF}}^2}{r}$	$\beta(t=0)$
140	3.6	6.5	600	1.33	12,5
135	3.7	7	600	1.34	12,1
128	3.9	6.5	600	1.12	11,6
116	4.3	7.5	500	1.27	12,4
109	4.6	9	400	1.68	14,3
102	4.9	9	400	1.47	13,5
88	5.7	10.1	350	1.40	13,3
77	6.5	11.5	300	1.43	13,6
67	7.5	14	250	1.58	14,1
53	9.45	16.5	200	1.46	14.0
41	12.25	24	150	1.69	14,3
29	17	36.5	100	1.93	15,1
15	34	75	50	2.12	15,5

this would in turn require a high Rabi frequency, which might not be available.

Thus in the first experiment, we compare rephasing by optimized  $\pi$  or RAP pulses at a given Rabi frequency. In this measurement, we optimize the duration of  $\pi$  and RAP pulses and the chirp range for RAP for each Rabi frequency. The result of this measurement is shown in figure 4.12. The red, solid circles represent the integrated light storage (or probe pulse energy) after rephasing with a pair of RAP pulses. The black, hollow squares show the same quantity after  $\pi$  pulse based rephasing. Table 4.1 shows the respective pulse parameters for each measured point, as well as the simplified adiabaticity criterion (4.7) and the mixing angle  $\beta$  at the beginning of the RAP pulse. Figure 4.12 also shows a numerical simulation for each measured data point based on the data from table 4.1.

The data show a rising rephasing efficiency with increasing Rabi frequency for both types of rephasing. In case of  $\pi$  pulses, the increasing Rabi frequency results in shorter pulse durations to reach a  $\pi$  pulse area. Short pulses have a larger spectral bandwidth and thus they cover a larger part of the inhomogeneous broadening  $\Gamma_{\text{inh}}$ . Beyond  $\Omega_{\text{RF}} \approx 2\pi \times 70$  kHz, the efficiency does not increase any further, implying that the pulses already cover the inhomogeneous linewidth sufficiently. For the RAP pulses, the efficiency increases, because the higher Rabi frequency allows for higher chirp rates, and a corresponding larger chirp range during the pulse duration. A high chirp range signifies a large initial detuning and consequently a mixing angle that is close to zero or  $90^\circ$ , as required for a RAP pulse. For small Rabi frequencies, we could also decrease the chirp rate by increasing the pulse duration. However, we chose the RAP pulse duration to obtain the maximum rephasing efficiency with the shortest possible pulse in order to enable a fair comparison with the  $\pi$  pulses. With our choice of short pulses, we operate on the edge of the adiabaticity criterion (see table 4.1). Section 4.5.5 discusses this issue in further detail.

The data indicate a superior performance of RAP pulses for every Rabi frequency. Especially for small Rabi frequencies, the signal enhancement by using RAP based rephasing is of a factor of 2, whereas for large Rabi frequencies it is of a factor of 1.15, compared to  $\pi$  pulse based rephasing. Thus even on the edge of adiabaticity, RAP already yields a higher performance compared to diabatic  $\pi$  pulses. The simulations shown in figure 4.12 confirm this result, but reveal another weakness of  $\pi$  pulses. Even though, the data show no further enhancement in efficiency, the simulations predict a higher possible performance of  $\pi$  pulses for larger Rabi frequencies. However, this discrepancy can be explained by the fact that the simulation excludes any RF-field inhomogeneities.

## 4.5.2 Rephasing with RF Field Inhomogeneities

Figure 4.12 indicates that beyond the influence of inhomogeneous broadening, a second mechanism reduces the efficiency of diabatic rephasing. This mechanism is an RF-field inhomogeneity of the RF magnetic field coils that generate all pulses used for rephasing. In order to experimentally verify the influence of field inhomogeneity, we perform a light storage experiment in two different PrYSO crystals with length  $l = 10$  mm and  $l = 1$  mm. Besides the length, both crystals have the

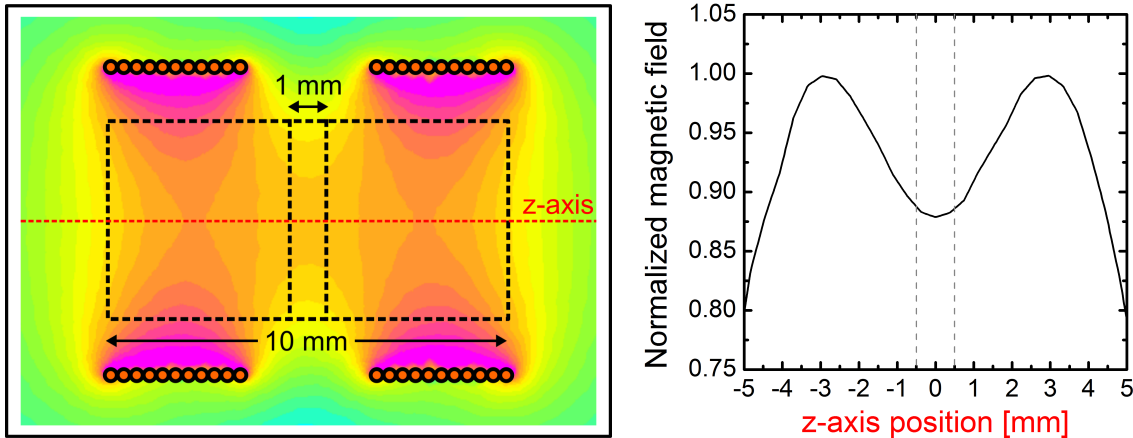


Figure 4.13: (Left) Schematic drawing of an intersection plane of the coils and the crystal used to investigate RF field inhomogeneities. The dots represent the copper wires of the RF coils, the black dashed boxes depict a PrYSO crystal with length  $l = 10$  mm and  $l = 1$  mm, respectively. The propagation axis of the light beams is collinear with the z-axis, depicted by the red, dashed line. The contour plot is a simulation (made with the software FEMM 4.2) of the magnetic field produced by the pair of RF coils, where green color indicates a weak magnetic field, purple color indicates a strong magnetic field. (Right) Normalized field strength along the z-axis in a range of  $\pm 5$  mm around the crystal center position  $z = 0$ . The gray dashed lines indicate the spatial extension of the 1 mm crystal.

same specifications. Note that for these specific experiments we exchanged the RF coils in order to fit the large crystal inside the cryostat. The new coils have 11 windings each, a diameter of  $d = 7.7$  mm, a length of each coil of  $l = 3.5$  mm and they are separated by 3.4 mm. The RF coils are located with respect to the crystals as depicted in figure 4.13. The figure shows an intersecting plane along the symmetry axis of the coils, which is collinear with the beam propagation direction. It includes also a simulation of the magnetic field, induced by our exact coil geometry, depicted as a contour plot in the figure. For both pulses we again optimized duration and chirp range at a Rabi frequency of  $\Omega_{\text{RF}} = 2\pi \times 70$  kHz, which is the maximum value for this specific coil geometry. This Rabi frequency is sufficiently large to operate the  $\pi$  pulse in a regime, where it covers the full inhomogeneous broadening (compare figure 4.12). Figure 4.14 shows the time resolved light storage signal from the short (a) and the long (b) crystal after  $\pi$  (black, hollow squares) and RAP pulse based rephasing (red, solid circles). It is evident from the measurement that  $\pi$  pulse based rephasing suffers from the application in a long crystal, while RAP based rephasing still permits high retrieval efficiency. In the short crystal, RAP pulses provide a 1.15 times higher efficiency, whereas in the long crystal RAP based rephasing yields a 1.67 times higher retrieved signal. The reason for the superior performance of RAP pulses can be understood with the spatial variation of the magnetic field along the center z-axis of the crystal, i.e., the propagation axis of the control and probe beam that create the atomic coherences. The right graph in figure 4.13 shows this quantity inside the long crystal (whose center is located at position  $z = 0$ , i.e., the center of the RF coils). The Rabi frequency varies by more than 20% over the whole crystal length

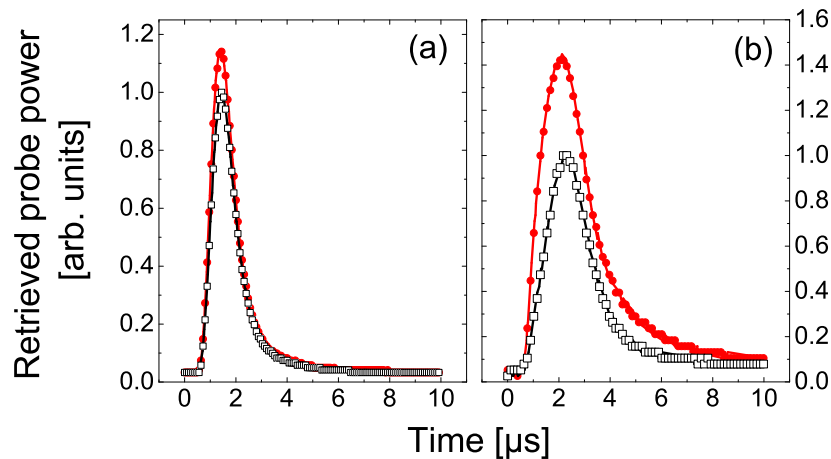


Figure 4.14: Time resolved, retrieved stored light signals from a crystal with (a) length  $l = 1$  mm and (b)  $l = 10$  mm. Red, solid circles indicate the signal after rephasing with two RAP pulses. Black, hollow squares represent the signal after two rephasing  $\pi$  pulses.

and thus it is impossible to define a  $\pi$  pulse for all positions at the same time. Therefore, an optimized  $\pi$  pulse is only an average solution for the inhomogeneous magnetic field distribution. However, the efficiency of a RAP pulse does not depend on pulse areas but on the adiabaticity criterion. Thus the rephasing process happens to be perfect, even if the Rabi frequency (or magnetic field strength) varies. The spatial variation of the magnetic field is much lower inside the short crystal (whose spatial extension is indicated by the gray dashed lines). Thus the condition for a  $\pi$  pulse is easier - but yet impossible - to fulfill for small RF field inhomogeneity.

### 4.5.3 Rephasing with Varying Rabi Frequency

We saw from the last measurement that the variation of Rabi frequency (or RF magnetic field, respectively) has a significant influence on the rephasing efficiency of  $\pi$  pulses, whereas RAP pulses are robust against such variations. Thus in the next measurement, we systematically vary the Rabi frequency, while keeping all other parameters fixed. We start from an optimized RAP and  $\pi$  pulse for a Rabi frequency  $\Omega_{\text{RF}} = 2\pi \times 140$  kHz, and record the retrieved stored light signal. The RAP pulse duration is not as short as shown in table 4.1, but  $\tau_{\text{RAP}} = 51 \mu\text{s}$  (with a chirp range of 600 kHz). Note that these experiments were performed again in the PrYSO crystal with a length  $l = 3$  mm and with the RF coils described in section 4.4.3. The result of this measurement is depicted in figure 4.15, where black, hollow squares represent the data for  $\pi$  based rephasing and red, solid circles depict the data after RAP based rephasing. Both rephasing techniques yield a similar rephasing efficiency for a Rabi frequency  $\Omega_{\text{RF}} = 2\pi \times 140$  kHz. However, as soon as the Rabi frequency decreases, rephasing with  $\pi$  pulses immediately loses efficiency, which is well confirmed by a numerical simulation (black, dashed line). The deviation at high Rabi frequencies is again caused by the RF inhomogeneity.

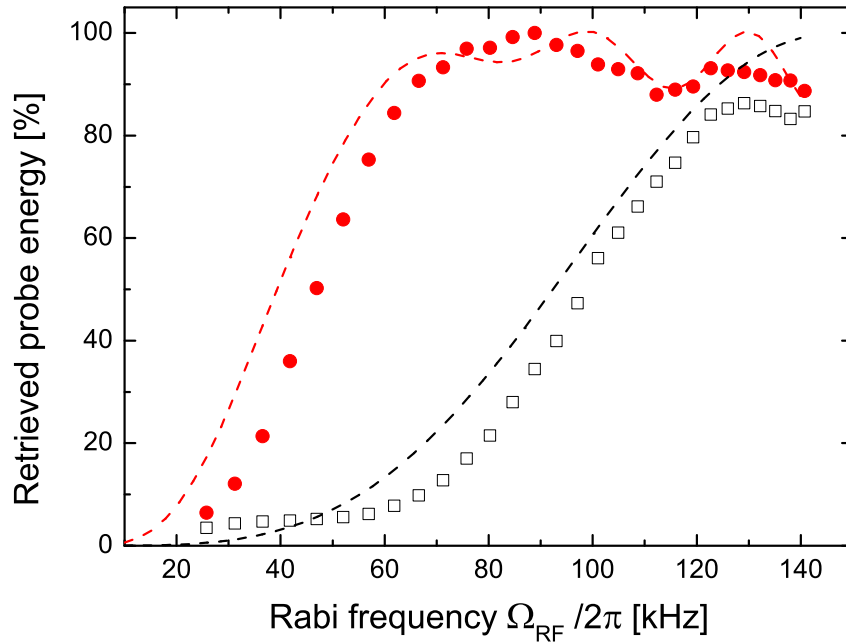


Figure 4.15: Change of retrieved probe pulse energy after two rephasing pulses when the Rabi frequency  $\Omega_{\text{RF}}$  for an optimized rephasing RAP (red solid circles) or  $\pi$  pulse (black, hollow squares) is varied. The rephasing pulses were initially optimized for  $\Omega_{\text{RF}} = 2\pi \times 140$  kHz. The red and black dashed lines show numerical simulations for rephasing with RAP and  $\pi$  pulses, respectively.

Rephasing with RAP on the other hand yields almost constantly high retrieval efficiency until the Rabi frequency drops below  $\Omega_{\text{RF}} \approx 2\pi \times 70$  kHz. The adiabaticity criterion yields  $\Omega_{\text{RF}}^2/r > 2.6$  for all Rabi frequencies above  $2\pi \times 70$  kHz, indicating adiabatic evolution. However, rephasing with  $\pi$  pulses start to fail completely for Rabi frequencies  $\Omega_{\text{RF}} < 2\pi \times 60$  kHz, where robust rephasing with RAP pulses still yields almost 100% efficiency. Note that the numerical simulation for RAP as well as the experimental data show slight oscillations, which will be discussed in section 4.5.5.

#### 4.5.4 Rephasing with a Static Detuning

The last systematic variation of an experimental parameter concerns the static detuning. Again we start with optimized pulses at two fixed Rabi frequencies of  $\Omega_{\text{RF}} = 2\pi \times 130$  kHz or  $\Omega_{\text{RF}} = 2\pi \times 60$  kHz. The  $\pi$  pulses have durations of  $\tau_{\pi} = 3.5 \mu\text{s}$  for the higher Rabi frequency and  $\tau_{\pi} = 8.3 \mu\text{s}$  for the weaker Rabi frequency. The RAP pulses have durations and chirp ranges of  $\tau_{\text{RAP}} = 6.9 \mu\text{s}$  and  $\Delta = 600$  kHz for the high, and  $\tau_{\text{RAP}} = 17.75 \mu\text{s}$  and  $\Delta = 200$  kHz for the weak Rabi frequency.

Now we scan the center frequency of the pulse around the center frequency of the inhomogeneous linewidth, i.e.,  $\omega = 2\pi \times 10.19$  MHz, while keeping all other parameters fixed. Thus we record the bandwidth of the pulses or in other words, we verify the maximum inhomogeneous broadening the rephasing pulses cover. Figure 4.16 shows the retrieved probe energy versus the central pulse frequency

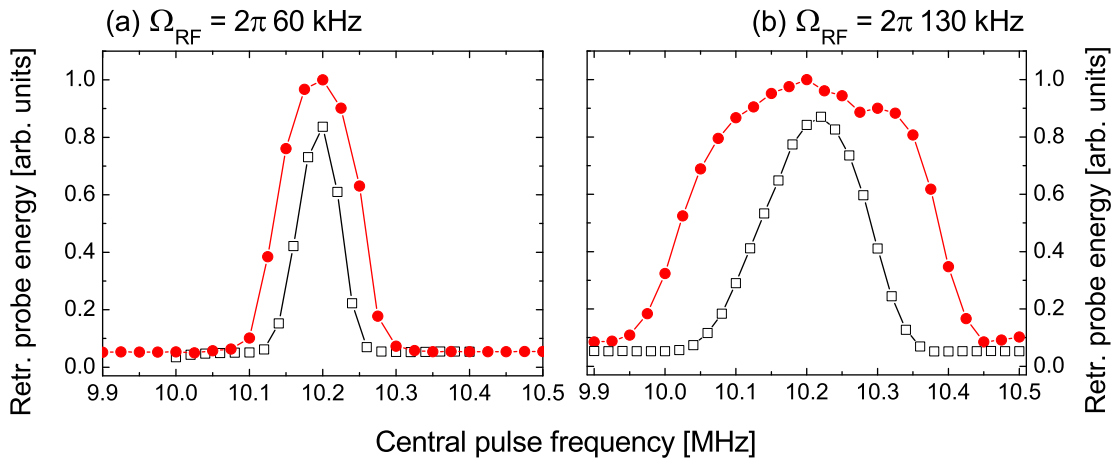


Figure 4.16: Retrieved probe pulse energy after rephasing with RAP (red, solid circles) and  $\pi$  pulses (black, hollow squares) for different central pulse frequencies. Figure (a) shows the result for weak, figure (b) for high Rabi frequency  $\Omega_{\text{RF}}$ .

for  $\pi$  (black, hollow squares) or RAP pulse based rephasing (red, solid circles). Both graphs prove a higher efficiency with RAP pulses over a broader spectrum, compared to  $\pi$  based rephasing. The latter suffers from any detuning, because the required pulse area for a  $\pi$  flip immediately becomes incorrect for changed detuning. The data show this feature for both Rabi frequencies, whereat the spectral full width half maximum of a  $\pi$  pulse is  $\Delta\nu = 75$  kHz for  $\Omega_{\text{RF}} = 2\pi \times 60$  kHz and  $\Delta\nu = 175$  kHz for  $\Omega_{\text{RF}} = 2\pi \times 130$  kHz and thereby comparable to the Rabi frequency. However the spectrum of a RAP pulse exceeds this width by roughly a factor of 2. In fact the detuning is limited by the total chirp range, which defines in combination with the Rabi frequency the mixing angle  $\beta$ . For a perfect RAP,  $\beta$  has to be  $0^\circ$  at the beginning of the pulse and  $90^\circ$  at its end (or vice versa). However, RAP pulse rephasing fails entirely at a detuning of  $\pm 100$  kHz for  $\Omega_{\text{RF}} = 2\pi \times 60$  kHz and  $\pm 250$  kHz for  $\Omega_{\text{RF}} = 2\pi \times 130$  kHz. This results in a mixing angle of  $\beta_{60} = 45^\circ$  and  $\beta_{130} = 55^\circ$  at the beginning or the end of the pulse, depending on whether the detuning is negative or positive. Thus the probability amplitudes for the diabatic states have not been inverted, i.e., the system has not undergone a  $\pi$  flip during the RAP pulse.

#### 4.5.5 Perfect RAP Pulses

All RAP pulses that have been used so far, had a rectangular shaped temporal profile for the Rabi frequency. A perfectly adiabatic pulse however should evolve smoothly in time as demanded by the adiabaticity criterion (4.6). The last section of this chapter provides a short note on the optimal temporal design of RAP pulses. Figure 4.17 shows the retrieved probe energy while scanning the pulse duration of two rephasing RAP pulses. Besides the pulse duration, all other parameters are fixed, i.e., the total chirp range is constant and the Rabi frequency is kept constant at  $\Omega_{\text{RF}} = 2\pi \times 135$  kHz. Varying the pulse duration while keeping the total chirp range fixed, also changes the chirp rate. Figure 4.17 shows three scans,



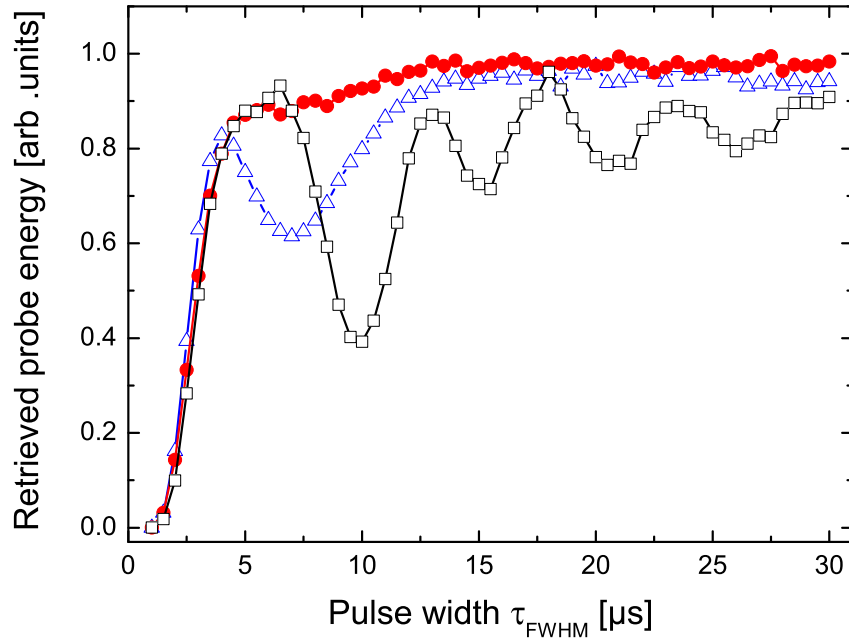


Figure 4.17: Retrieved probe pulse energy vs. the pulse width (FWHM) of rephasing RAP pulses with either rectangular shape and a chirp range of  $\Delta = 600$  kHz (black, hollow squares), a Gaussian shape with a chirp range of  $\Delta = 600$  kHz (blue, hollow triangles), or a Gaussian shape with a chirp range of  $\Delta = 900$  kHz (red, solid circles). The Rabi frequency is kept constant at  $\Omega_{\text{RF}} \approx 2\pi \times 135$  kHz.

corresponding to three different applied RAP pulses. The first is a rectangular shaped pulse with a total chirp range of  $\Delta = 600$  kHz (black, hollow, squares), i.e., a pulse, used in prior experiments as well. For short pulse durations, the pulse does not fulfill the adiabaticity criterion, because the chirp rate is too high. With increasing duration, the efficiency increases and the rephasing approaches a first maximum at  $\tau_{\text{RAP}} = 6 - 7 \mu\text{s}$ . However, if the duration is scanned further, the rephasing efficiency exhibits oscillations. These are a sign of diabatic interaction, i.e., the steep rising and falling wings of the rectangular shape lead to a coupling of the adiabatic states and thus the system does not evolve fully adiabatic. A second contribution to the oscillations is correlated to the mixing angle. At the beginning of the pulse, the Rabi frequency is not zero, and thus the mixing angle is not perfectly zero, but  $\beta = 12.1^\circ$  at the beginning of the pulse (for  $\Delta = 600$  kHz and  $\Omega_{\text{RF}} = 2\pi \times 135$  kHz). Obviously, rectangular shaped pulses do not provide a perfect RAP pulse, although, they already yield a good performance for rephasing atomic coherences. In order to further improve RAP, we exchange the rectangular shape by a Gaussian shape. The pulse duration given in figure 4.17 represents the full width half maximum (FWHM) of the Gaussian envelope, whereat the total pulse duration is defined by thrice the FWHM. This choice yields equal pulse area for the rectangular and the Gaussian shaped pulses at equal FWHM pulse duration. The blue, hollow triangles represent the data for a Gaussian shaped pulse with a 600 kHz total chirp range. Indeed, the pronounced oscillations almost vanish and the data show only a single oscillation between  $5 \mu\text{s}$  and  $10 \mu\text{s}$ . If the total chirp range is increased by a factor of 1.5 to 900 kHz (red, solid circles), we obtain a

purely adiabatic behaviour as soon as the simplified adiabaticity criterion  $\Omega_{\max}^2/r$  is sufficiently fulfilled. Note that the latter yields a value of  $\sim 2$  for durations  $\tau_D > 15 \mu\text{s}$ , which is sufficiently adiabatic as proven by the Gaussian shaped RAP pulses in figure 4.17. Thus the reason for the oscillations in the rectangular shaped case is the steep rising and falling edge, i.e., a fast change of the Rabi frequency, and an imperfect initial condition, which both leads to a coupling between the adiabatic states, i.e., diabatic behaviour.

## 4.6 Conclusion

Concluding, RAP enables efficient rephasing which is insensitive to fluctuations of Rabi frequency, pulse duration and detuning, provided the adiabaticity criterion is fulfilled. RAP therefore provides superior performance when compared to  $\pi$  pulses, which must obey strict confinements of their pulse parameters. In particular, RAP provides high rephasing efficiency in inhomogeneously broadened systems, with inhomogeneous driving fields or limited available driving field power. A simple way to realize a perfect RAP pulse is the use of a Gaussian shaped pulse and a linear chirp. However, in order to fulfill the adiabaticity criterion, perfect RAP pulses typically require long pulse durations in comparison to  $\pi$  pulses. In particular, pulse durations become very long when the maximum available driving field power is low or the inhomogeneous broadening of a system is large. Long pulse durations are indeed a drawback of RAP (and other adiabatic pulses) as long pulses signify increased power dissipation in a system. The latter usually causes heating, especially when many pulses are used in, e.g., dynamical decoupling sequences. Long pulse durations become also a problem when the decoherence time of a system is short and rephasing has to happen within this short time period. A critical view on RAP reveals as well that perfect RAP-based rephasing requires an even number of identical pulses (or more complicated pulse sequences) in order to restore the exact initial phase of every coherence within the inhomogeneous line. Thus, perfect RAP-based rephasing requires stable parameters on the time scale of two subsequent RAP pulses, even though the pulse parameters themselves are not tied to strict confinements.

An alternative, promising approach towards robust and efficient rephasing are composite pulses [76, 77]. These pulses use phase changes between a series of, e.g.,  $\pi$  pulses in order to improve the performance of a single  $\pi$  pulse with respect to specific parameter fluctuations, i.e., the detuning or the Rabi frequency [77]. If the order of a composite pulse, i.e., the number of pulses within a series, is not too high, the pulse duration can be less than for adiabatic pulses. Composite pulses have also been used with RAP to improve the latter, whereas composite RAP pulses require even longer durations than single RAP pulses [78].

## Chapter 5

# Coherence Population Mapping

It is a central goal of this work to prolong the storage duration for coherent information storage in PrYSO. When we store information, we use atomic coherences, which contain amplitude and phase information of an input data pulse. The maximum life-time of coherences is limited by decoherence processes, i.e., stochastic, irreversible interactions between a quantum system and its environment. The characteristic decoherence time is typically orders of magnitude shorter than its theoretical maximum given by twice the population relaxation time.

The usual approach to extend the life-time of an atomic coherence is to decouple the atomic system from its environment. In PrYSO, two techniques are usually combined, static and dynamical decoupling. Static decoupling uses a static magnetic field that aligns Y and Pr spins and thus reduces the probability of spin flips, a main source of decoherence [63]. In addition, the magnitude and the direction of the magnetic field are set to a *critical point*, where some Zeeman levels and their corresponding transitions become first order insensitive to fluctuations of magnetic fields, as induced by residual spin flips (termed ZEFOZ = **Z**ero **F**irst **O**rders **Z**eeman shift) [25, 63].

Dynamical decoupling uses pulsed RF magnetic fields to reduce the influence of residual fluctuations of transition frequencies and the corresponding change of the coherence phase evolution [28, 29]. The combination of dynamical and static decoupling leads to strongly enhanced decoherence times in the range of the population relaxation time. However, it comes with the price of a complicated and complex experiment.

An alternative approach to prolong the life-time of a coherence is to reversibly map amplitude and phase of the coherence onto a long-lived population distribution. When a population distribution is used as a shelving state, we can ignore the effect of decoherence during the storage time and no decoupling techniques are required to reach storage times in the range of the population relaxation time. We just need a writing and a reading sequence to reversibly map the coherence.

The stimulated photon echo (SPE) is a common approach to transfer the amplitude and phase of a coherence to a population distribution in an inhomogeneously broadened transition [30, 31, 33, 79]. However, not all individual systems in the storage medium carry the same information. Each stores an individual portion of the coherent information depending on the spectral position of the system in the inhomogeneous line. SPE requires only two  $\pi/2$  pulses on a single (inhomogeneously broadened) transition to store and retrieve an initial coherence from populations. It is thus relatively easy to implement and avoids complex experimental setups beyond the ability to generate mapping pulses. How-

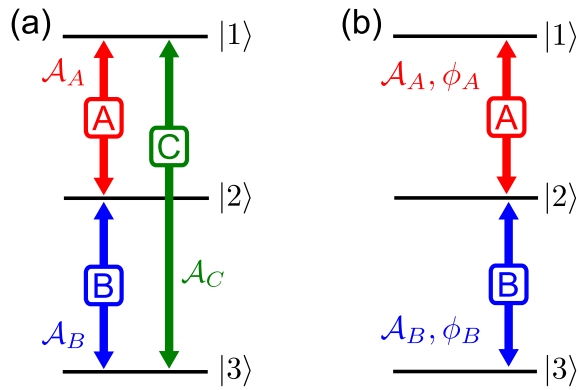


Figure 5.1: Three-state  $\Xi$ -system. (a) CPM coupling scheme with three coupling fields “A”, “B” and “C”. The control parameter for a CPM mapping sequence are the pulse areas  $\mathcal{A}$  of each coupling field. (b) CPM coupling scheme with two coupling fields “A” and “B”, each with two control parameters, pulse area  $\mathcal{A}$  and driving field phase  $\phi$ .

ever, a coherence contains two parameters that we need to store, amplitude and phase. Consequently a protocol that stores a coherence in populations requires two independent mapping parameters. SPE uses the population difference in a two-state transition and inhomogeneous broadening of the latter to fulfill this condition. Thus inhomogeneous broadening is mandatory for SPE to store the full information of a coherence. In particular this is necessary to store a coherence independent from its initial phase.

In this thesis we present a novel approach to reach ultra-long storage durations by means of reversible *coherence population mapping* (CPM). Our approach maps the full information of a coherence, i.e., amplitude and phase, onto a population distribution in a single three-state system. The latter already provides two independent population probability amplitudes which we can use to store amplitude and phase in a single system. As an important consequence, CPM stores the information of an initial coherence in every individual system equally well, a significant difference to SPE. CPM thus works in homogeneously as well as in inhomogeneously broadened media, an expansion in comparison to SPE.

The original proposal for CPM was developed by Yatsenko et al. [80] and uses three coupling fields “A”, “B” and “C” as depicted in figure 5.1 (a). In this approach all coupling fields are resonant. Each field and its interaction with the corresponding transition is described with a single parameter, the pulse area  $\mathcal{A}_{A,B,C}$ . In [80], we show that all three coupling fields are mandatory to map amplitude and phase onto the three states. We thus apply a short CPM “write” sequence involving all three coupling fields with well defined pulse areas to map a coherence onto a population distribution in the three-state system. After a storage time, which is only limited by population relaxation, a short CPM “read” sequence maps the population back onto a coherence. Thus, just like SPE, also CPM offers a simple approach to preserve coherences without elaborate techniques and requires only a short write and read sequence.

However, a drawback of CPM with three coupling fields is the following. In a three-state system we hardly find all three transitions allowed. If transition A and B are allowed transitions, transition C is usually forbidden by a selection rule, e.g., the selection rule for the orbital angular momentum when all transitions are optical transitions. Even in systems like PrYSO, where the selection rules impose only softer constraints, a three-state system usually exhibits one weak transition compared to the other two. This is a severe obstacle in order to experimentally

implement CPM. In particular in inhomogeneously broadened media, weak transitions and corresponding weak Rabi frequencies prevent a full coverage of the transition and lead to a decreased storage efficiency. In addition, low Rabi frequencies result in very long pulses and decoherence starts to play a role during the mapping sequence.

In order to avoid the problem of weak or forbidden transitions, Vitanov et al. developed CPM sequences that introduce the phase  $\phi$  of the coupling field as an additional control parameter [81]. This allows to exclude the weakest transition from the CPM scheme as already two transitions provide four control parameters, which are sufficient to map amplitude and phase. The control parameters are now the pulse areas  $\mathcal{A}_{A,B}$  and the driving field phases  $\phi_{A,B}$  as depicted in figure 5.1 (b). Solutions that contain the phase as an additional control parameter are often termed *composite* solutions. Composite pulses (CP) have been used for decades in NMR in order to perform accurate and robust spin manipulations [76]. The main idea of CPs is to replace an imperfect interaction by a series of interactions with properly chosen phases that compensate for the imperfection. More recently, composite pulses have also been used for robust rephasing of optically driven atomic coherences [77, 78]. Besides the new set of control parameters, composite CPM works just in the same way as the originally proposed CPM. Both the CPM write and read sequence consist of three pulses. Write and read sequences contain at least one pulse acting on the transition “A” and a second acting on transition “B” (or vice versa). The driving field of the remaining pulse has a phase that is different from the phase of the other two pulses.

In this thesis, we implement the composite CPM protocol and compare it to the SPE protocol. This chapter starts with a theoretical description of composite CPM. This includes an analysis on how composite CPM sequences are derived and a presentation of the most important properties of composite CPM. The next section analytically describes SPE and its characteristic features. The chapter continues with an overview on the experimental implementation of CPM and SPE in PrYSO. The last section presents experimental results for CPM and SPE with either RF induced coherences or optically driven coherences after an EIT-based light storage experiment.

## 5.1 Theoretical Background

This section provides a theoretical discussion of composite CPM according to the work of Vitanov and co-workers [81]. It is based on the Hamilton operator for a driven three-state system in rotating wave approximation (3.20). For a three-state system as depicted in figure 5.1 (b), with couplings on two transitions and all detunings given with respect to state  $|2\rangle$ , it reads

$$\hat{H}(t) = -\frac{\hbar}{2} \begin{pmatrix} -2\Delta_{12} & e^{i\phi_{12}}\Omega_{12}(t) & 0 \\ e^{-i\phi_{12}}\Omega_{12}^*(t) & 0 & e^{i\phi_{23}}\Omega_{23}(t) \\ 0 & e^{-i\phi_{23}}\Omega_{23}^*(t) & 2\Delta_{23} \end{pmatrix} \quad (5.1)$$

with selectable phases  $\phi_{ij}$  for the driving fields. For the CPM write and read process, we use a consecutive pulse sequence, which enables a separated treatment of each coupling on transition A or B with, e.g., the Hamiltonian  $\hat{H}_A$ ,

$$\hat{H}_A(t) = -\frac{\hbar}{2} \begin{pmatrix} -2\Delta_{12} & e^{i\phi_{12}}\Omega_{12}(t) & 0 \\ e^{-i\phi_{12}}\Omega_{12}^*(t) & 0 & 0 \\ 0 & 0 & 2\Delta_{23} \end{pmatrix} \quad (5.2)$$

The Hamiltonian  $\hat{H}_B$  for transition B is deduced in a similar way.  $\hat{H}_A(t)$  (and  $\hat{H}_B(t)$ ) almost have the form of a two-state interaction, including an additional detuning for the second transition. The easiest way of deriving CPM sequences is to consider the resonant case, i.e.,  $\Delta_{12} = \Delta_{23} = 0$ . In addition we consider pulses which have a temporal rectangular shape, i.e., a constant Rabi frequency  $\Omega_{ij}$  during each interaction. Hence, the Hamiltonian for each interaction is time independent and has the form of a pure two state interaction. As a consequence, the value of the probability amplitude vector  $\vec{c}(t) = (c_1(t), c_2(t), c_3(t))$  after an interaction time  $\Delta t$  is determined by a unitary propagator  $\hat{U} = \exp(-i\hat{H}t)$  to  $\vec{c}(t_f) = \hat{U}\vec{c}(0)$ . The propagator for pulses acting on transition A with the above assumptions takes the simple form

$$\hat{U}_{\phi_A}^A(\mathcal{A}) = \begin{pmatrix} \cos(\mathcal{A}/2) & -ie^{-i\phi_A}\sin(\mathcal{A}/2) & 0 \\ -ie^{-i\phi_A}\sin(\mathcal{A}/2) & \cos(\mathcal{A}/2) & 0 \\ 0 & 0 & 1 \end{pmatrix} \quad (5.3)$$

where  $\phi_A$  is the phase of the driving field and  $\mathcal{A}_A$  is the respective pulse area for the interaction with duration  $\Delta t$  on transition A. The propagator for transition B is obtained in a similar way.

The next step in order to determine a write and read pulse sequence is to calculate the transformation of the density matrix elements under the influence of the write and read sequence. The calculation described here is exemplary and assumes a write sequence that consists of a pulse A, a subsequent pulse B and again a pulse A. Each pulse can have an individual phase and possesses a well defined pulse area. We assume an initial density matrix  $\hat{\rho}^{\text{ini}}$  that has arbitrary populations  $\rho_{ii}$  and coherent superpositions  $\rho_{ij}$ . The density matrix after the write sequence  $\hat{\rho}^{\text{w}}$  is obtained by calculating

$$\hat{\rho}^{\text{w}} = \hat{U}^{\text{w}}\hat{\rho}^{\text{ini}}(\hat{U}^{\text{w}})^\dagger \quad \text{with} \quad \hat{U}^{\text{w}} = \hat{U}_{\phi_{w3}}^A(\mathcal{A}_{w3})\hat{U}_{\phi_{w2}}^B(\mathcal{A}_{w2})\hat{U}_{\phi_{w1}}^A(\mathcal{A}_{w1}) \quad (5.4)$$

After the write sequence, the system is subject to decoherence and consequently, only the diagonal entries in the density matrix are left such that

$$\hat{\rho}^{\text{w}} \rightarrow \hat{\rho}^{\text{dec}} = \sum_i \rho_{ii}^{\text{w}} \quad (5.5)$$

After the storage time  $\Delta\tau$ , we apply the read sequence

$$\hat{\rho}^{\text{read}} = \hat{U}^{\text{r}}\hat{\rho}^{\text{dec}}(\hat{U}^{\text{r}})^\dagger \quad \text{with} \quad \hat{U}^{\text{r}} = \hat{U}_{\phi_{r3}}^A(\mathcal{A}_{r3})U_{\phi_{r2}}^B(\mathcal{A}_{r2})U_{\phi_{r1}}^A(\mathcal{A}_{r1}) \quad (5.6)$$

Equations (5.4) - (5.6) give an expression for the final coherence after the read sequence on a desired transition. In the most general case, this yields an expression which is rather long. Therefore, we will first present pulse sequences that provide the most efficient mapping and retrieval and then discuss the result. The condition a CPM sequence has to fulfill is  $\gamma_{\text{read}} = \gamma_{\text{ini}} + \phi_{\text{var}}$ , i.e., the phase of the initial coherence is fully restored and we allow an additional phase induced by the write or read pulses. We choose the latter phase  $\phi_{\text{var}}$  to enable, e.g., built-in rephasing by introducing a phase shift  $\phi_{\text{var}} = \pi$  to the initial phase. The second condition is to restore the amplitude of the initial coherence  $|\rho_{12}^{\text{ini}}|$  with a constant pre-factor  $f$  such, that  $|\rho_{12}^{\text{read}}| = f|\rho_{12}^{\text{ini}}|$ , with  $0 < f \leq 1$ . Table 5.1 shows the most efficient write and read sequences so far obtained by Vitanov and co-workers. All sequences consist of three write and read pulses, either in the order A-B-A or B-A-B. Note that the read sequences in table 5.1 contain an overall phase  $\phi$ , which indicates a phase shift of all pulses. Now we let either the ABA, or the BAB sequence from table 5.1 act on the system. We are interested in the restored coherence  $\rho_{12}^{\text{read}}$ . The relevant density matrix elements determined with equations (5.4) - (5.6) read

$$\rho_{11}^{\text{read}} = \rho_{22}^{\text{read}} = \rho_{33}^{\text{read}} = \frac{1}{3} \sum_{n=1}^3 \rho_{nn}^{\text{ini}} \quad (5.7)$$

$$\text{ABA: } \rho_{12}^{\text{read}} = -\frac{1}{3} e^{i\phi} \left( \rho_{12}^{\text{ini}} + e^{-i\phi_w} \rho_{23}^{\text{ini}} - e^{i\phi_w} \rho_{31}^{\text{ini}} \right) \quad (5.8)$$

$$\text{BAB: } \rho_{12}^{\text{read}} = -\frac{1}{3} e^{i(\phi + \phi_r - \phi_w)} \left( \rho_{12}^{\text{ini}} + e^{i\phi_w} \rho_{23}^{\text{ini}} - e^{2i\phi_w} \rho_{31}^{\text{ini}} \right) \quad (5.9)$$

The first line shows the populations after the CPM read sequence. It indicates equally distributed populations among the three states after CPM, no matter what the initial population distribution was. The second and third line show the coherence we retrieve from the system with the ABA or BAB sequence. First of all, this coherence is a mixture of all initial coherences that were present in the initial system. Thus CPM works for cases, in which two states only are in a coherent superposition, i.e., only one coherence  $\rho_{12}^{\text{ini}}$  was initially prepared and  $\rho_{23}^{\text{ini}} = \rho_{31}^{\text{ini}} = 0$ .

Second, we find a pre-factor of  $-(1/3)$  for the coherence amplitude. In fact, every transition in the three-state system carries  $(1/3)$  of the initial coherence, i.e., the coherence is not lost, but distributed among all transitions. The latter fact is strongly connected with the equal population distribution among all three states, which does not allow the preparation of a maximum coherence after the read sequence. To date, the theoretical retrieval of  $1/3$  of the coherence amplitude on a single, i.e., the desired read-out transition is the best obtained with CPM. It is also not clear yet, if this value is a theoretical limit or if it can be further enhanced.

The minus sign in front of the coherence indicates a  $\pi$  phase shift of the coherence, which we introduced on purpose to automatically rephase the restored coherence after the CPM read sequence. In general, both sequences add phases  $\phi_w$ ,  $\phi_r$  and  $\phi$  to the coherence phase. These are freely selectable in the write and read sequences and without loss of efficiency, they can be set to zero or to a desired value if necessary. Last but not least the retrieval efficiency

$$\eta_{\text{CPM}} = \frac{|\rho_{12}^{\text{read}}|}{|\rho_{12}^{\text{ini}}|} = \frac{1}{3} \quad (5.10)$$

Table 5.1: CPM write and corresponding read sequences deduced from equations (5.4) - (5.6) by Vitanov et al.  $A_{\phi_A}(\mathcal{A})$  represents pulses on the transition A with pulse area  $\mathcal{A}$  and phase  $\phi_A$ .  $B_{\phi_B}(\mathcal{A})$  represents pulses on the transition B.  $\theta$  is a specific pulse area  $\theta = \arccos(-1/3)$ .  $\phi$  is an overall phase for the read sequence.

write	read
$A_0(\pi/2)B_{\phi_w}(\theta)A_{\pm\pi/2}(\pi/2)$	$[A_{\pm\pi/2}(\pi/2)B_{\phi_r}(\theta)A_0(\pi/2)]_{\phi}$
$B_0(\pi/2)A_{\phi_w}(\theta)B_{\pm\pi/2}(\pi/2)$	$[B_{\pm\pi/2}(\pi/2)A_{\phi_r}(\theta)B_0(\pi/2)]_{\phi}$

is independent from the initial coherence phase  $\gamma$ . This is an important feature of CPM which no other protocol based on populations in single systems provides. It signifies that the protocol reversibly maps arbitrary initial coherences equally well.

Concluding, CPM maps an arbitrary initial coherence onto populations in a three-state system and restores it with a maximum efficiency of one third. CPM stores the full information about amplitude and phase in each single three-state system of the medium, i.e., in the probability amplitudes  $c_j$  of each state. This is why no manifold of systems is required to store the information.

However, it is crucial to understand that even though the full information is stored in the probability amplitudes of a single system, it cannot be obtained from a single system only. This is because the CPM process involves decoherence between the write and read sequence. Decoherence signifies a randomization of the phase such that all macroscopic coherences in the system vanish, whereas the population distribution persists. A coherence in a single system can change its phase randomly in a decoherence process, but it does not automatically vanish at the same time. Equations (5.8) and (5.9) indicate that a coherence on any transition before the read process will mix to the coherence we want to obtain after the read process. In an ensemble of systems, the randomized phases after the decoherence process lead to destructive interference of all residual coherences. Therefore the output after the read sequence consists only of the desired coherence, i.e., the coherence we initially mapped onto the population distribution. Storing the full information in a single must not be confused with retrieving the information from a single system. CPM needs an ensemble of systems in order to provide decoherence. Note that decoherence beyond phase randomization is caused by population relaxation. The latter is also the limitation for CPM.

In summary, CPM uses a simple write and read sequence, consisting of three pulses each, to reversibly map coherences onto populations. It is solely necessary to control the phase and the pulse area of the mapping pulses. Note that the above considerations base on resonant pulses, a condition which is not valid for inhomogeneously broadened transitions in PrYSO (see section 5.3.4 on how to encounter this problem experimentally). More elaborated CPM sequences are currently derived to encounter these problems. In this work, the goal is to prove the concept of CPM with its most important characteristics, i.e., phase-insensitive storage efficiency and ultra-long storage time with an easily applicable pulse sequence.



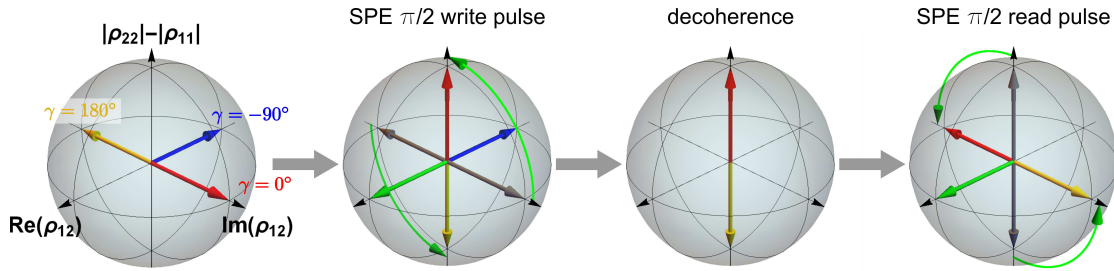


Figure 5.2: Simulation on the Bloch sphere of SPE with a zero time delay between data and write pulse for three characteristic phases  $\gamma = 0^\circ$  (red vector),  $\gamma = -90^\circ$  (blue vector) and  $\gamma = 180^\circ$  (yellow vector) of the initial coherence. The green vector is the torque vector.

## 5.2 Stimulated Photon Echo

The stimulated photon echo, or sometimes termed three pulse photon echo, is a well-known approach to store coherent information in populations [30, 31, 79]. It is also a common spectroscopic tool in order to determine population relaxation times on a single transition or to measure spectral diffusion [33, 44, 82]. This section introduces SPE, because later we compare it to the novel CPM protocol.

### 5.2.1 Theoretical Background

The SPE sequences we use consist of three  $\pi/2$  pulses. We refer to the first pulse as the data pulse. Note that in the literature some references refer to the second pulse as the data pulse. In general, the data pulse can also have a pulse area smaller than  $\pi/2$ . The pulses act all on a single transition, in our case the transition A. The data pulse and the write  $\pi/2$  pulse are separated by a time delay  $T$ . The time between the mapping write and read  $\pi/2$  pulses defines the storage time  $\Delta\tau$ . In order to understand the SPE protocol, it is convenient to first consider SPE in case of zero delay  $T$  between data and write pulse.

Figure 5.2 depicts each step of SPE with zero time delay  $T = 0$  on the Bloch sphere. The data  $\pi/2$  pulse creates a maximum coherent superposition of states  $|1\rangle$  and  $|2\rangle$ . The phase of the data pulse defines the axis of the Bloch sphere. Equivalent to the convention in chapter 3.1.2 we define a Bloch vector with  $\gamma = 0^\circ$  to point along the y-axis, i.e., the coherence has only an imaginary part. We consider three characteristic cases, a data  $\pi/2$  pulse with a phase  $\gamma^{\text{ini}} = 0^\circ$  (red Bloch vector),  $\gamma^{\text{ini}} = -90^\circ$  (blue Bloch vector) and  $\gamma^{\text{ini}} = 180^\circ$  (yellow Bloch vector). Since  $T = 0$ , the system has no time to evolve, which is why no phase evolution takes place. This excludes also dephasing in case of an inhomogeneous broadening. Immediately after the data pulse, the write pulse with a phase  $\phi = 0^\circ$  acts on the Bloch vectors. The torque vector of the writing pulse points into the  $\text{Re}[\rho_{12}]$  direction. As a consequence, not all Bloch vectors are rotated. The coherences with an initial phase of  $\gamma^{\text{ini}} = 0^\circ$  and  $\gamma^{\text{ini}} = 180^\circ$  are transferred into a population difference. Thereby, the initial phase determines the population distribution between states  $|1\rangle$  and  $|2\rangle$ . Coherences with an initial phase of  $\gamma^{\text{ini}} = 90^\circ$  on the other hand are mapped onto an equal population difference, i.e, they do not change during

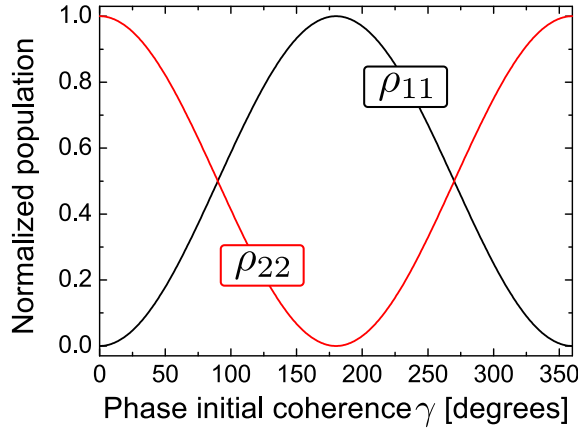


Figure 5.3: Population distribution after the SPE write pulse for an initial coherence, created by a  $\pi/2$  pulse with a varying phase  $\gamma$ .  $\rho_{11}$  is the population in state  $|1\rangle$ ,  $\rho_{22}$  is the population in state  $|2\rangle$ .

the write pulse. Figure 5.3 shows the population distribution for a varying initial phase  $\gamma$  of an initial maximum coherence. The oscillatory dependence becomes a problem when the waiting time between write and read pulse exceeds the decoherence time. The Bloch vector components representing superpositions vanish and only the population distribution remains (see figure 5.2). The population difference after the write pulse is a projection of the imaginary part of the coherence on the population z-axis of the Bloch sphere. When the read pulse is applied, it creates only coherences, where the population difference was non-zero. Thus the coherence with an initial phase  $\gamma^{\text{ini}} = 90^\circ$  is completely lost. However, SPE restores coherences with initial phases  $\gamma^{\text{ini}} = 0^\circ$  and  $\gamma^{\text{ini}} = 180^\circ$  with 100% efficiency. Obviously, SPE with a zero time delay is highly phase-sensitive and thus not suitable as a storage protocol for arbitrary coherences. The phase-dependent efficiency results directly from the sinusoidal population distribution simulated in 5.3. It reads

$$\eta_{\text{SPE}}(T = 0) = -ie^{i\gamma} \sin\gamma \quad (5.11)$$

The phase-sensitivity of SPE can be overcome by introducing a non-zero time delay  $T$  between data and write pulse. Figure 5.4 shows a series of Bloch vector evolutions on the Bloch sphere during a time delayed SPE sequence. First, the data  $\pi/2$  pulse creates a coherence with an arbitrary phase, e.g.,  $\gamma = 0^\circ$ . If the data pulse acts on an inhomogeneously broadened medium, the time delay between data and write pulse allows the system to dephase (figure 5.4 (1)). If  $T \gg \Gamma_{\text{inh}}^{-1}$ , i.e., the time delay is longer than the dephasing time, the coherence phases are distributed continuously between  $0^\circ$  and  $360^\circ$  on the equatorial plane of the Bloch sphere. After the time  $T$ , the  $\pi/2$  write pulse maps the coherences onto population differences. However, these depend on the respective phases of each coherence at the time  $T$ , i.e., the population difference depends on the imaginary part of the coherence. After the write pulse and a waiting time longer than the decoherence time  $T_2$ , the inhomogeneously broadened system contains a distribution of population differences as indicated in figure 5.4 (2) and (3) and figure 5.5. The population distribution depends on the spectral position of a system within the inhomogeneous line, because the transition frequency defines the phase evolution and therefore the phase after the time delay  $T$ . Thus we have created a population grating in the inhomogeneous line. The grating period in the frequency domain

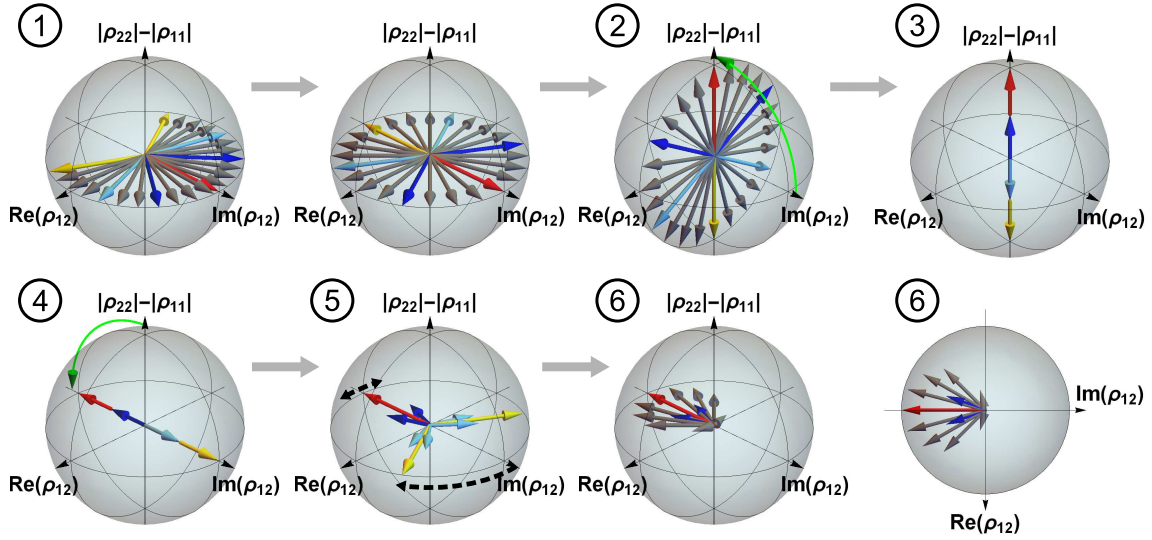


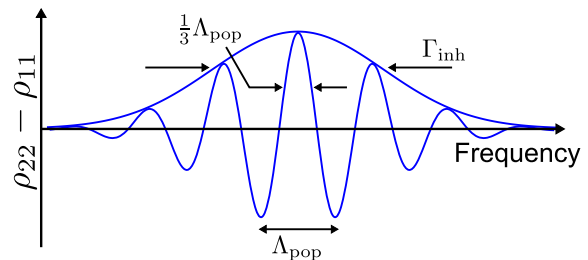
Figure 5.4: Bloch vector simulation for time delayed SPE. The red vector represents the resonant ensemble in the Bloch sphere frame. The colored vectors represent non-resonant ensembles and serve as visual orientation. (1) The system starts to dephase. (2) After a time  $t=T$  an SPE write pulse flips all Bloch vectors by  $90^\circ$  around the x-axis. (3) Decoherence leaves the system with an incoherent population distribution. (4) An SPE read pulse flips the Bloch vectors by  $90^\circ$ . The length of the vectors now depends on the population difference after the decoherence process. (5) The vectors start to rotate in two ways: The two yellow vectors rephase towards the red Bloch vector. Around the red and yellow vectors, dephasing occurs. (6) Stimulated photon echo at a time  $t=T$  after the read pulse (Yellow and red vectors, as well as the light blue and dark blue vectors have the same position).

$\Lambda_{\text{pop}}$  is given by the time delay  $T$  to [30]

$$\Lambda_{\text{pop}} = \frac{1}{2T} \quad (5.12)$$

Note that if  $T$  is shorter than the dephasing time, the grating period becomes larger than the inhomogeneous linewidth. Thus we can treat the transition as purely homogeneously broadened. In other words, a zero time delay experiment ignores the effect of inhomogeneous broadening and simulates a purely homogeneously broadened two-state system. If we apply the  $\pi/2$  read pulse after the storage time (see figure 5.4 (4)), only transitions with a non-zero population difference will create a coherence. Immediately after the read pulse, we find coherences with a phase  $\gamma = 0^\circ$  and  $\gamma = 180^\circ$  (depending on whether more population was in state  $|1\rangle$ )

Figure 5.5: Population difference  $\rho_{22} - \rho_{11}$  within the inhomogeneous linewidth  $\Gamma_{\text{inh}}$  after the SPE write pulse. The initial coherence is completely dephased when the write pulse interacts with the medium at time  $T \gg \Gamma_{\text{inh}}^{-1}$ .  $\Lambda_{\text{pop}}$  is the population grating period.



or  $|2\rangle$ ). All systems start to dephase again and yield a maximum overall coherence after a time  $T$ , the initial waiting time between data and write pulse (see figure 5.4 (5) and (6)). However, the different coherences do not exactly rephase and the population grating picture reveals why this is the case. After the read pulse, only non-zero population differences allow the generation of a coherence. Thus we find discrete oscillators at relative spectral positions  $0, \Lambda_{\text{pop}}/2, \Lambda_{\text{pop}}, \dots$  within in the inhomogeneous linewidth. These rephase after a time  $t = 1/2\Lambda_{\text{pop}} \equiv T$ . However, the discrete oscillators are broadened by  $(1/3)\Lambda_{\text{pop}}$  (FWHM), represented by the systems that have a population difference between 0 and  $\pm 1$ . The broadening leads to an additional dephasing which decreases the magnitude of the overall coherence retrieved after the waiting time  $T$ .

Time delayed SPE does indeed allow phase-insensitive storage and retrieval of coherences. However, it does not restore the exact phase of the initial coherence. In fact it generates an echo after the time  $T$  with an average phase that is defined by the SPE read pulse. The FWHM phase distribution around this average phase is determined by  $(1/3)\Lambda_{\text{pop}} \cdot T$ . Note that the efficiency in this case is

$$\eta_{\text{SPE}}(T \gg \Gamma_{\text{inh}}^{-1}) = \frac{1}{2} \quad (5.13)$$

In the experimental realization of CPM and SPE we will always perform experiments with a zero time delay  $T = 0$ . This allows the investigation of SPE (or CPM) without dephasing. It thus enables systematical measurements with a well defined phase, ignoring dephasing effects in inhomogeneously broadened media. The results obtained from these measurements, i.e., with a single, well defined phase can easily be expanded to a general case that involves many initial phases.

### 5.2.2 Comparison of CPM and SPE

The last two sections about CPM and SPE allow a first theoretical comparison of the two protocols. SPE requires an inhomogeneously broadened transition and a time delay  $T$  between data and write pulse in order to map and retrieve a coherence independent from its initial phase. The maximum retrieval efficiency is in this case  $1/2$  of the initial coherence magnitude. However, during the mandatory time delay before the write pulse, decoherence further reduces the efficiency. If the inhomogeneous broadening is small or the time delay  $T$  is short, the retrieval efficiency depends on the phase of the initial coherence. Therefore, storing arbitrary coherences with SPE is limited to inhomogeneously broadened systems. On the other hand, SPE requires only a  $\pi/2$  write and read pulse on one transition. It is thus a rather simple protocol.

CPM stores an initial coherence in the populations of a single three-state system. This does neither require a time delay between data pulse and write sequence nor inhomogeneous broadening. CPM thus works in any system that provides three states with two allowed transitions. The retrieval efficiency is  $1/3$  of the initial coherence magnitude. In particular it is always independent on the initial phase of the coherence. Both, the CPM write and read sequence, consist of three pulses on two transitions in a three-state system. Thus, CPM requires slightly more pulses than SPE but is still a simple protocol.

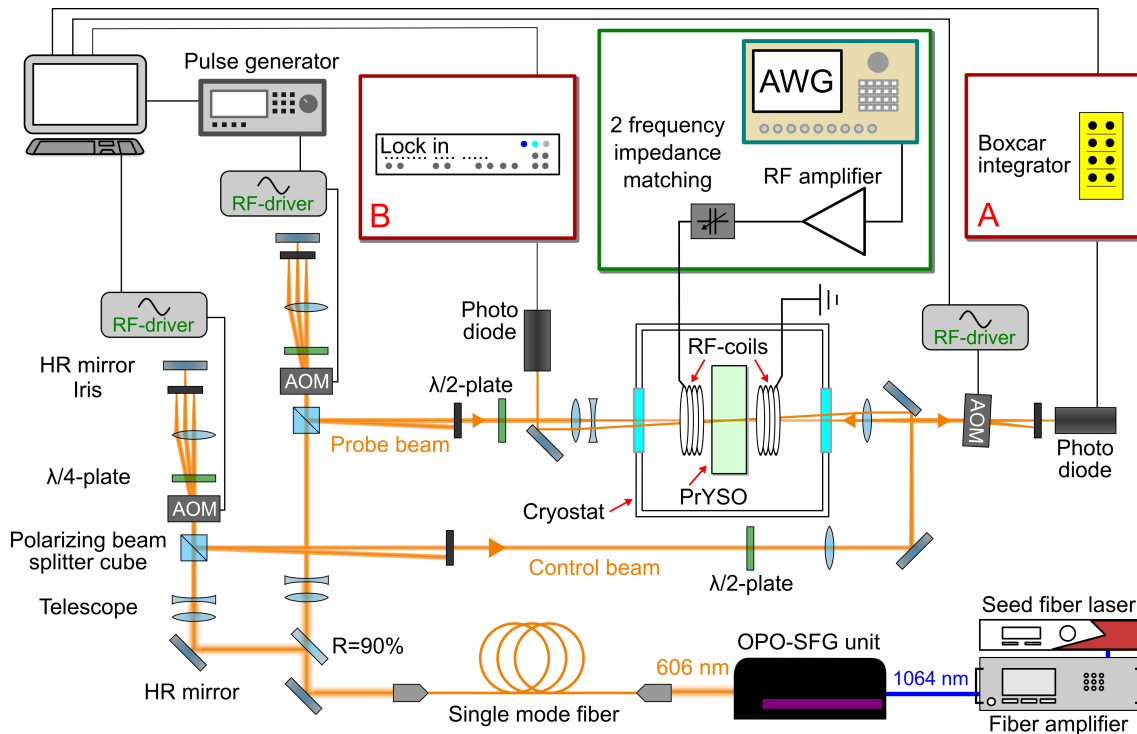


Figure 5.6: Schematic experimental setup for CPM and SPE, including optical setup, RF setup (green box) and two different detection units (red boxes A and B). Black lines represent transmission lines for electronic signals, orange lines represent the laser beam.

## 5.3 Experimental Setup

We implement CPM (and SPE) in the hyperfine levels of the  $^3\text{H}_4$  ground state of PrYSO. For the rest of the chapter, we relabel the states to  $|\pm 1/2\rangle = |1\rangle$ ,  $|\pm 3/2\rangle = |2\rangle$  and  $|\pm 5/2\rangle = |3\rangle$  (see figure 1.2 for original labels). The pulses “A” and “B” are RF pulses on the “A” transition  $|1\rangle \leftrightarrow |2\rangle$  and on the “B” transition  $|2\rangle \leftrightarrow |3\rangle$ . We use the experimental setup depicted in figure 5.6 to generate all necessary optical and RF pulses and to detect restored coherences. The setup is in large parts similar to the one shown in chapter 4.4. This section highlights only changes applied to the latter in order to adapt it to experiments with CPM and SPE.

### 5.3.1 Optical Setup

In this setup we use the OPO-SFG laser system described in detail in chapter 2. Besides the replacement of the laser system, the optical system is identical to the previous setup, apart from the FWHM beam diameter inside the crystal. These are  $d_c = 400\ \mu\text{m}$  for the Gaussian shaped control beam and  $d_p = 150\ \mu\text{m}$  for the probe beam with a flattop profile inside the crystal. In contrast to the previously presented experiments, we test CPM on both, coherences prepared by pulsed RF magnetic fields and on coherences prepared in a light storage experiment. In case of pure RF experiments we use only the control beam line to generate pulses for the optical preparation (see section 5.3.4) and Raman heterodyne detection (see

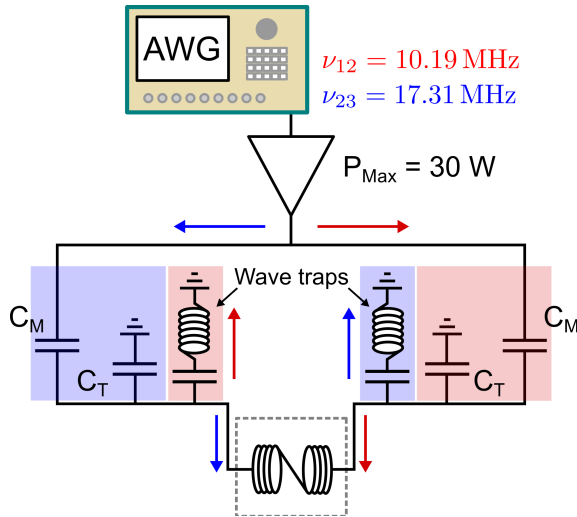


Figure 5.7: Schematic setup, including an impedance matching circuit, used to generate the RF fields for CPM or SPE experiments.  $C_T$  and  $C_M$  are capacitors, AWG is an arbitrary waveform generator and the triangle represents an RF amplifier. The coils inside the gray box represent the RF coils inside the cryostat. Red highlighted parts belong to the impedance matching for the frequency  $\nu_{12}$ , blue highlighted parts for the frequency  $\nu_{23}$ .

section 5.3.3). In case of light storage we use the probe as well as the control beam. In this case, the control beam is used for optical preparation and storage of the weak probe beam as described in chapter 4.4.5.

### 5.3.2 Generation of Radio-Frequency Magnetic Fields

CPM works in a three-state system and requires the coupling of two transitions in the RF regime. Thus the RF setup to generate magnetic fields has to be extended to the use of two frequencies. These are  $\nu_{12} = \nu_A = 10.19\text{ MHz}$  and  $\nu_{23} = \nu_B = 17.31\text{ MHz}$ , i.e., the frequencies of transition A and B. The RF setup is implemented as depicted in the green box in figure 5.6 and in detail in figure 5.7. The same arbitrary waveform generator as in the previous setup generates the CPM write and read sequence as well as the pulse used to prepare the initial coherence. The output is amplified in an RF amplifier (Minicircuits, LZY-22+) with a maximum output power of  $P = 30\text{ W}$  in a frequency range of  $\Delta\nu = 0.1 - 200\text{ MHz}$ . The RF coils are similar to the ones described in chapter 4.4. They have a diameter of  $d = 7.3\text{ mm}$  and length of  $l = 3.5\text{ mm}$ . Each coil carries 11 windings of copper wire with a diameter of  $d = 300\text{ }\mu\text{m}$ . Identical to the previous RF setup, we have to match the frequency-dependent, imaginary impedance of the RF-coils inside the cryostat to the amplifier's real impedance of  $Z = 50\text{ }\Omega$ . Note that the matching circuit has to match two frequencies simultaneously. A single frequency matching circuit does not work here, because the bandwidth of the latter is too small, compared to the difference of the two required frequencies. Usually, broadband impedance matching is established by a  $50\text{ }\Omega$  resistor. However, this method provides only imperfect matching and consequently low maximum Rabi frequencies. Thus we implement a new, two-frequency matching circuit, which is based on the single-frequency version [74]. In fact, it is a doubled version of the latter as indicated by the blue and red boxes in figure 5.7. The RF signal propagates through the matching circuit (consisting again of a tunable matching and tuning capacitor). Each circuit is adjusted to the particular frequency A or B. The RF coil inside the cryostat is part of both matching circuits. After the RF coils, the signal is

guided to ground level by a wave trap, which consists of a series oscillating circuit. We note that this is simplified description and all components of the circuit form several oscillating circuits. A detailed description of the matching circuit and its performance is given in [83] and Appendix D. The incident RF wave is not necessarily dissipated in the RF coils, even if the matching circuit provides an overall impedance to  $Z = 50 \Omega$ . This is why we adjust the circuit not with a network analysis tool, but by means of maximizing the Rabi frequency on both transitions A and B. Therefore we empty certain levels in the ground states of PrYSO by optical pumping with a single frequency laser beam. When an RF magnetic field is applied on one of the two transitions, population is transferred back to previously emptied states. This causes absorption of the same laser beam as used for optical pumping before. Thus by observing laser absorption we directly measure population oscillation, i.e., the Rabi frequency. The measured Rabi frequencies at maximum RF power of  $P = 30 \text{ W}$  are  $\Omega_{12} = \Omega_A = 2\pi \times 145 \text{ kHz}$  and  $\Omega_{23} = \Omega_B = 2\pi \times 50 \text{ kHz}$ .

### 5.3.3 Raman Heterodyne Detection

In order to investigate CPM, we create coherences in two different ways. Either, we apply RF pulses to directly create a coherence in the hyperfine ground states of PrYSO, or we prepare optically driven atomic coherences in a light storage experiment. The latter has been described in detail in the chapter 4.4.5, including the detection of stored light signals.

In order to detect RF induced coherences, we use Raman heterodyne detection (RHD), which is based on coherent, stimulated Raman scattering [84–86]. The goal of RHD is the conversion of an RF coherence  $\rho_{12}$  into a scattered light field by means of a detection laser (see figure 5.8). The latter has a real Rabi frequency  $\Omega_D$  and the angular frequency  $\omega_D = \omega_{13}$ , i.e., the detection laser is resonant with the transition between the ground state  $|1\rangle$  and an excited state  $|3\rangle$ .

Note that figure 5.8 (level scheme on the left-hand side) and the following description refer to the generation of a Raman Stokes beam, i.e., the frequency of the scattered Stokes field  $\omega_S = \omega_D - \omega_{12} = \omega_{23}$  is lower than the frequency of the initial detection laser beam  $\omega_D$ .

Raman scattering also produces an Anti-Stokes field at a frequency  $\omega_{AS} = \omega_D + \omega_{12}$ . In our coupling scheme, this occurs via an off-resonant process and the Anti-Stokes signal is very small. We thus detect mainly the Stokes radiation. In the inhomogeneously broadened optical line of PrYSO we find also systems which generate resonant Anti-Stokes radiation, i.e., when the initial laser field has a frequency  $\omega_D = \omega_{23}$ . Here, the Stokes field would be off resonant and thus weaker.

The source of the Stokes light field is the optical coherence  $\rho_{23}$  which leads to a time dependent polarization of the medium  $\vec{P}_{23}(t) = N\vec{\mu}_{23}\rho_{23}\exp(i\omega_S t)$ , with the particle number density  $N$  and the dipole transition moment  $\vec{\mu}_{23}$ . The polarization acts as a source of the Stokes radiation  $\vec{E}_S$  (compare equation (2.4)). It reads

$$\vec{E}_S(t) = \frac{L\mu_0\omega_S^2}{2ik_S}\vec{P}_{23}(t) = \frac{L\mu_0\omega_S^2}{2ik_S}N\vec{\mu}_{23}\rho_{23}e^{i\omega_S t} \quad (5.14)$$

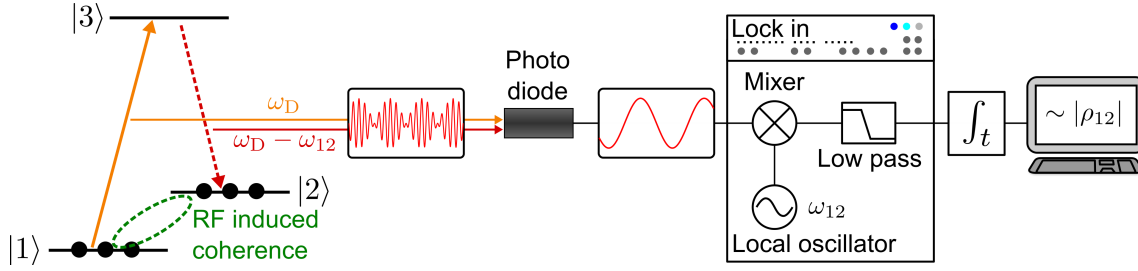


Figure 5.8: Raman heterodyne detection scheme used to detect RF induced coherences.

where  $L$  is the medium length and  $\mu_0$  is the vacuum permeability. Note that the electric dipole moment  $\mu_{23}$  is usually higher than the magnetic ground state dipole transition moment  $\mu_{12}$ . Therefore the field generated from the optical coherence is stronger than the radiation generated from the ground state coherence, i.e., the coherence we want to detect. Transferring the ground to an optical coherence thus yields a stronger detection signal. In order to calculate the optical coherence we solve the Liouville-von-Neumann equation (3.12). It describes the temporal evolution of the three-state system and yields six coupled differential equations for populations and coherences. Before we analytically solve equation (3.12), we neglect the influence of decoherence and population relaxation, which both happen on times scales  $> 100 \mu\text{s}$  in PrYSO. This is valid since the signal detection happens on much shorter time scales ( $< 10 \mu\text{s}$ ). Solving equation (3.12) yields the following expression for the optical coherence

$$\rho_{23} = i \sin\left(\frac{\Omega_D}{2} t\right) \rho_{12} \approx i \frac{\Omega_D}{2} t \rho_{12} \quad (5.15)$$

The optical coherence is thus linearly dependent on the ground state coherence  $\rho_{12}$ . The approximation in (5.15) is valid for short read out times  $t < \pi/\Omega_D$ , as it is the case in our experiment. Note that solution (5.15) refers to a single three-state system and does not include detuned detection fields or interferences between different Stokes or Anti-Stokes beams. A more general analysis is given in [85].

The process that leads to solution (5.15) is similar to a frequency mixing process of the coherence  $\rho_{12}$  with the detection laser field and the propagation direction of the initial laser beam and the Raman scattered light fields is collinear. The latter fact is crucial for heterodyne detection, which requires detection of both beams simultaneously on a photodiode with sufficiently high bandwidth to detect their beat note (Thorlabs, PDA 10A-EC). This yields a signal

$$I_{\text{RHD}} \propto \frac{1}{2} \left( |E_S|^2 + |E_D|^2 + (E_S E_D^* + c.c.) \right) \quad (5.16)$$

The first two terms contribute as a constant offset, whereas the latter term exhibits the beat note of the scattered and the initial beam. The beat note oscillates with their difference frequency  $\omega_{12}$ . The magnitude of the beat note is proportional to the Raman scattered field which depends linearly on the coherence  $\rho_{12}$ . In order to measure the beat note magnitude independent from noise and the constant offset, we demodulate the photodiode signal in a lock-in amplifier (Zurich Instruments, ZI HF2LI). Thereby we produce a signal that is linearly proportional to both the initial coherence amplitude  $|\rho_{12}|$  and the detection beam intensity  $\sim E_D^2$ .



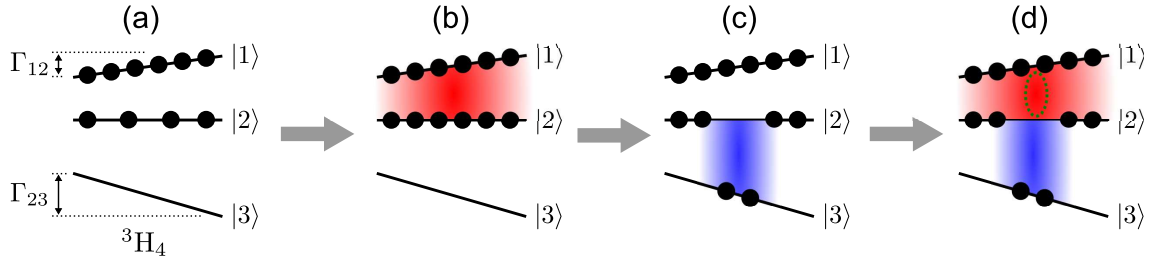


Figure 5.9: Sequential steps used to prepare an RF pit in the inhomogeneously broadened hyperfine ground state transitions in PrYSO: (a) Population distribution after optical pumping (not shown). (b) - (d) Population distribution after a series of A (red) and B (blue) pulses. The width of the colored boxes indicates the spectral width of the pulses A and B.

### 5.3.4 Measurement Procedure

In order to provide a systematical analysis of CPM, we prepare RF induced coherences. In a second experiment, we apply CPM to optically driven atomic coherence after a light storage process. We have to prepare the storage medium PrYSO in order to generate either RF induced coherences or optically driven coherences after a light storage process. The light storage experiment has already been described in the previous chapter. The preparation for a pure RF experiment is somewhat different to the preparation for light storage. It consists of three steps, two based on optical pumping, and one based on RF interaction.

First, we prepare an absorption free, spectral pit with a frequency chirped control laser pulse in a relative frequency range of 0 – 18 MHz. One chirp lasts 20 ms and has a laser power of  $P = 1$  mW. This procedure is repeated six times. In the second step, isolated absorption lines are prepared inside the spectral pit. We chose two rectangular shaped repumping pulses at relative frequencies  $\nu_1 = 20.5$  MHz and  $\nu_2 = 30.7$  MHz with a power of  $P_R = 1$  mW each.

Note that the detection beam for RHD has a relative frequency of  $\nu_D = 3.2$  MHz and a power of  $P_D = 1.5$  mW. We are thus interested in the population distribution in the ensembles addressed by this specific detection laser frequency. The detection laser couples all three possible ground states to one of the excited states. Each coupling happens in a different ensemble within the inhomogeneous line (compare figure 4.9). However, we are only interested in the detection of coherences in the  $|1\rangle \leftrightarrow |2\rangle$  transition and thus neglect all couplings from state  $|3\rangle = |\pm 5/2\rangle$ . In the RHD, coherences including these states would contribute with beat frequencies at 17.31 MHz or 27.5 MHz, frequencies that we do not demodulate in the lock-in amplifier, i.e., we do not detect them.

After the optical preparation, the averaged population distribution over all relevant ensembles shows no population in the third state and unequal population in states  $|1\rangle$  and  $|2\rangle$  as shown in figure 5.9 (a). In step three of the preparation we apply a series of rectangular shaped RF pulses on both transitions in order to prepare a population distribution which we term RF pit. We first equal the population between states  $|1\rangle$  and  $|2\rangle$  by applying three  $\pi/2$  pulses followed by incoherent coupling, all on transition A. The  $\pi/2$  pulses have durations of  $\tau(\pi/2) = 1.7 \mu\text{s}$ , the incoherent coupling lasts  $\approx 600 \mu\text{s}$ . All RF pulses are generated with the max-

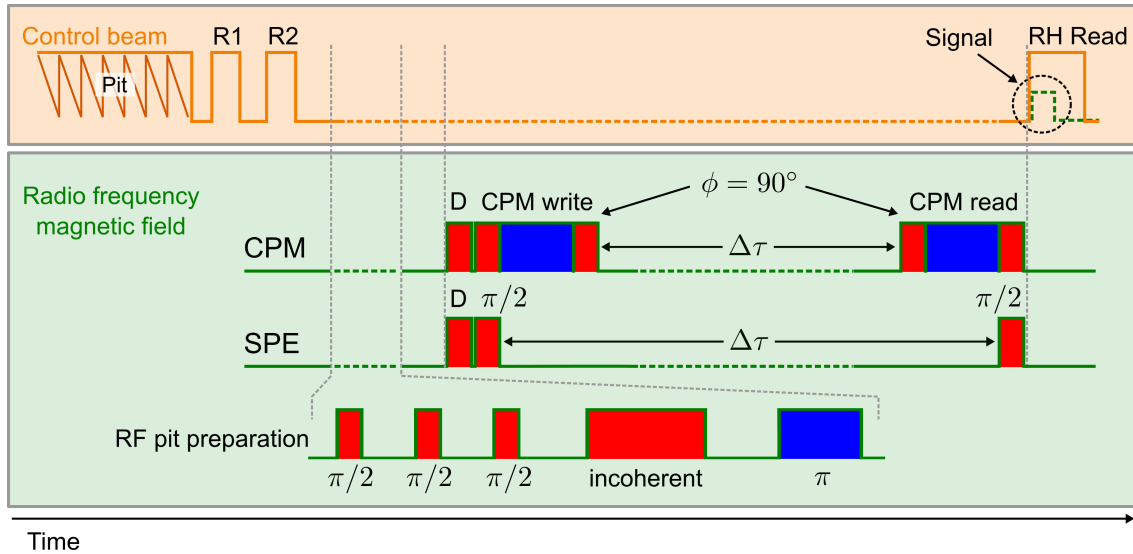


Figure 5.10: Temporal sequence of optical (orange box) and RF pulses (green box) used for optical preparation, preparation of an RF pit and optical detection as well as RF pulses used to perform a CPM or SPE experiment. D is the data pulse which creates the initial coherence. R1 and R2 are optical repumping pulses.

imum available RF power. Note that all pulses are separated by a time  $t > T_2$  to prevent coherent interaction between the pulses. The population distribution in the relevant ensembles is depicted in figure 5.9 (b). A subsequent  $\pi$  pulse B with duration  $\tau(\pi) = 5 \mu\text{s}$  transfers population to state  $|3\rangle$  as indicated in figure 5.9 (c). However, the B pulses we use in our experiment have a maximum Rabi frequency of  $\Omega_{23} = 2\pi \times 50 \text{ kHz} < 2\pi \times 80 \text{ kHz} = \Gamma_{\text{inh}}^{23}$ , i.e., a spectral width smaller than the inhomogeneous linewidth of the transition B. Thus, population transfer happens in a spectral width determined only by the B pulse. We call this population configuration an RF pit (analogue to the spectral pit in the optical regime). If we apply an A  $\pi/2$  pulse, which couples to the whole inhomogeneous line due to its high Rabi frequency, we generate a coherence exclusively in ensembles, prepared by the B pulse before. This is important to reduce errors due to weak B pulses and enables the systematical investigation of CPM in a pure RF experiment.

Figure 5.10 shows the temporal arrangement of optical (orange box) and RF preparation pulses (green box). After the preparation, we start a CPM or an SPE experiment (see figure 5.10 (green box)). We first apply a data  $\pi/2$  pulse on the transition A, labeled “D” in figure 5.10. The data pulse has a rectangular shape and a duration (just like all  $\pi/2$  pulses A) of  $\tau(\pi/2) = 1.7 \mu\text{s}$  at maximum Rabi frequency. In order to change the phase of the initial coherence created by the data pulse, we change the phase of the corresponding RF wave in the arbitrary wave form generator. Immediately after the data pulse we apply the CPM write sequence, or a  $\pi/2$  pulse A for SPE, respectively. Note that with the choice of a zero time delay between data and write pulses we investigate the case  $T = 0$  for SPE described in section 5.2.1. The CPM write (and read) sequence we use in all experiments is the first A-B-A sequence from table 5.1. It consists of a  $\pi/2$  pulse on

transition A, a pulse with duration  $\tau(\theta) = 6\mu\text{s}$  on transition B, and a second  $\pi/2$  pulse A with a phase shift of  $\phi = 90^\circ$ . After a storage time  $\Delta\tau > T_2$ , we apply the CPM read sequence. It is the reversed write sequence, or in case of SPE a single  $\pi/2$  pulse. In order to read the restored coherence on transition A, we apply a single frequency detection laser beam for RHD from the control beam line. The RHD detection laser has a power of  $P = 1.5\text{ mW}$ .

## 5.4 Experimental Results

This section presents the experimental implementation of composite CPM in the solid-state storage medium PrYSO. Our goal is to verify the key features of CPM experimentally, also compared to SPE. We first have to investigate whether CPM restores an initial coherence and does not create an arbitrary coherence, e.g., induced by the CPM read sequence itself. This measurement is included in an experiment, where we investigate the capability of CPM to store coherences with arbitrary initial phase equally well. In a second experiment we want to perform ultra-long coherence storage with CPM, whereat the storage time  $\Delta\tau$  should be only limited by population relaxation. Note that these experiment are all-RF experiments. Finally, we investigate if CPM works also for EIT-based light storage. For every experiment, we compare the CPM results to coherence storage by a zero time delay SPE experiment (see section 5.2.1 for details). This helps us to experimentally verify and distinguish the predicted features of each protocol. In addition, SPE experiments are well-known and rather simple to implement. If SPE yields the predicted characteristics, we know that storage in populations is in principle possible, i.e., the experiment is running properly.

### 5.4.1 Mapping Efficiency Depending on the Coherence Phase

Experiments intended to prove phase-insensitivity of the CPM protocol use solely RF pulses. The reason is that we can precisely control the phase and the amplitude of an RF induced coherence. Optically driven atomic coherences on the other hand contain typically an unknown mixture of phases. Thus we use the sequence described in section 5.3.4 to carry out this experiment.

Figure 5.11 shows the retrieved signal energy when the phase  $\gamma$  of the initial coherence is varied between  $\gamma = 0^\circ$  and  $\gamma = 360^\circ$ . The storage time is  $\Delta\tau = 4\text{ ms}$  for all measurements shown in figure 5.11. The red, solid squares show the signal retrieved after the CPM sequence, blue solid circles represent data obtained with SPE. CPM yields a constant retrieval efficiency, i.e., the efficiency of the protocol does not depend on the phase of the initial coherence. SPE on the other hand shows strong oscillations as predicted by theory. For phases  $\gamma = 160^\circ$  and  $\gamma = 340^\circ$  the retrieved signal reaches a maximum value. However, for phases  $\gamma = 70^\circ$  and  $\gamma = 250^\circ$ , the SPE signal vanishes completely, i.e., no storage was possible. Figure 5.12 shows a simulation of the retrieval efficiency for CPM, and SPE (as well as for time delayed SPE), calculated from equations (5.10), (5.11) and (5.13). The data and simulations are in very good agreement. Note that theory predicts a

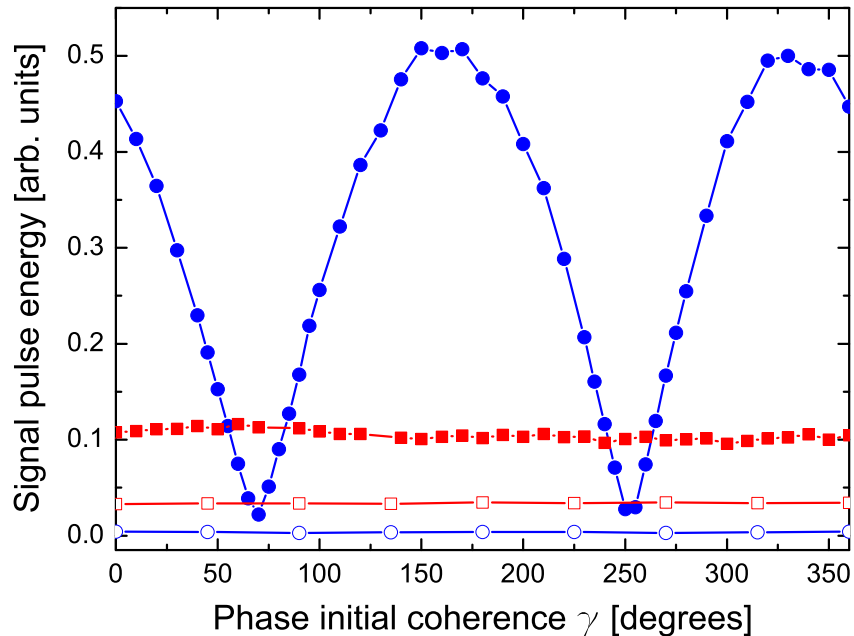


Figure 5.11: Retrieved Raman heterodyne signal energy versus phase  $\gamma$  of the initial coherence. Red, solid squares represent the signal retrieved with CPM, blue, solid circles represent SPE data. Hollow data indicate the retrieved signal after a CPM or an SPE sequence without an initial coherence.

zero efficiency for SPE with phases  $\gamma = 90^\circ$  and  $\gamma = 270^\circ$ . Our data is however constantly shifted by  $20^\circ$  to lower phases. This is due to a slightly detuned pulse A and has been confirmed by a simulation. Nevertheless, the data clearly show the key feature of both CPM and SPE and thus represent a first, evident proof of CPM.

Figure 5.11 also shows the retrieved signal energy when no initial coherence was prepared (hollow data points). This measurement indicates wrongly “restored” coherences, induced by the protocols themselves. The CPM protocol (red, hollow squares) produces a slightly higher error coherence than the SPE (blue hollow circles), caused mainly by weak pulses B on the  $|2\rangle \leftrightarrow |3\rangle$  transition. Note that without the RF pit, the noise introduced by weak B pulses would be substantially higher. In case of SPE, we do not use B pulses and consequently, the noise is reduced to zero. This result also shows a precise choice of experimental parameters, i.e., a correct pulse area of the A pulses. However, it is evident from the data that CPM restores the initial coherence and does not introduce substantial error coherences. The noise in case of CPM is always well below the obtained signal and thus, signals restored with CPM are always distinguishable from noise.

If we compare the maximum retrieved signal with SPE to the signals retrieved with CPM, the latter are smaller by a factor of about  $1/5$ , which is slightly lower than a theoretically predicted factor of  $1/3$ . The reduced CPM efficiency comes most likely with imperfect conditions for Raman heterodyne detection. After the read out sequence, population is equally distributed among all three involved ground states. Therefore, the laser beam used for optical detection couples to transitions within the inhomogeneous optical line, which have been emptied be-

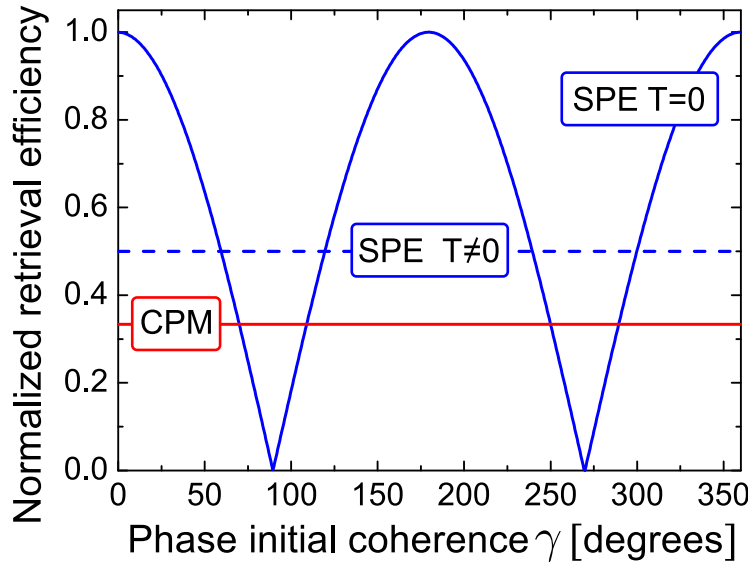


Figure 5.12: Simulation of retrieval efficiencies for time delayed SPE and non time delayed SPE and CPM according to equations (5.10),(5.11) and (5.13).

fore by optical pumping during the preparation scheme. A portion of the detection laser as well as the Raman scattered beam is thus absorbed by the repopulated transitions. SPE on the other hand results in equal population in states  $|1\rangle$  and  $|2\rangle$  only. Consequently, after CPM, the detection laser beam experiences enhanced absorption compared to detection after SPE. The overall signal is reduced below the relative factor of  $1/3$  accordingly.

#### 5.4.2 Mapping Efficiency Depending on the Storage Duration

In a second measurement we store an initial coherence either with a phase of  $\gamma = 70^\circ$  or  $\gamma = 160^\circ$  and vary the storage duration. The two initial phases represent extreme cases for SPE, as it restores a maximum signal for  $\gamma = 160^\circ$  and no signal in the other case. Figure 5.13 shows the retrieved signal energy after CPM or SPE for the two initial coherences versus the storage time  $\Delta\tau$ . Let us first look at the signal retrieved with SPE (black, hollow squares for an initial phase  $\gamma = 160^\circ$  and green, hollow triangles for  $\gamma = 70^\circ$ ). As expected from the previous measurement, SPE does not restore the coherence with  $\gamma = 70^\circ$ . However with an initial phase  $\gamma = 160^\circ$ , SPE retrieves a maximum signal that decays with a  $1/e$  time of  $\tau_{\text{SPE}} \approx 3.2\text{ s}$ . After a storage time of  $\Delta\tau \approx 30\text{ s}$ , the SPE signal has vanished completely. The situation with CPM restored coherences on the other hand is different. As expected from figure 5.11, the retrieved signal is lower than in the optimal case of SPE. However, CPM restores coherences at both phases equally well for storage durations until about 1 s. The  $1/e$  decay times are  $\tau_{\text{CPM}}^{70} \approx 5.4\text{ s}$  and  $\tau_{\text{CPM}}^{160} \approx 175\text{ s}$  and thus in both cases longer than for signals obtained with SPE. Please note that the decay for CPM signals is no single exponential, because two transitions and consequently two relaxation rates are involved during the storage process. We nevertheless define the  $1/e$  time as the storage time in order

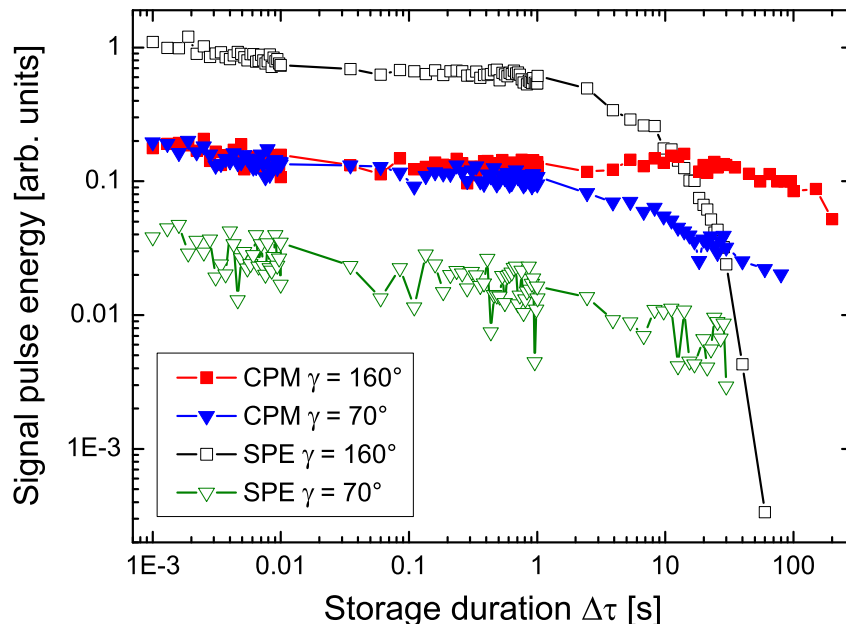


Figure 5.13: Retrieved Raman heterodyne signal energy versus storage duration  $\Delta\tau$  for two RF induced coherences with different initial phase  $\gamma$ , stored with CPM or SPE (see explanation in the figure).

to compare the different signal decays.

The data in figure 5.13 show ultra-long possible storage durations for coherences stored with CPM. However, the signals for different phases decay with different  $1/e$  times. This is due to different population relaxation times of the transitions A and B and becomes obvious by considering the phase dependent population distribution after the CPM write process (see figure 5.14). For an initial phase of  $\gamma = 160^\circ$  the population difference in the transition A is minimum, whereas the difference in the transition B is maximum. Therefore, the rather short relaxation time of  $T_1 = 8.7\text{s}$  on the transition A does not affect this specific population distribution much. The population relaxation only leads to an equal distribution of the anyway small population difference in the transition A. The population difference on the transition B is much larger, but relaxation on the transition B is slower. Hence,  $T_1$  on the transition B determines an upper limit for the storage duration for this specific phase. With an initial phase of  $\gamma = 70^\circ$ , the population distribution shows the opposite behaviour. The slowly relaxing transition B has a minimum population difference and the fast relaxing transition shows a maximum population difference. Therefore, the fast relaxation in the transition A is the main contribution to the signal decay, resulting in the observed, shorter storage time.

The SPE signal also shows a rather short decay, because it depends solely on the relatively fast population relaxation of the transition A. However, the decay time of  $\tau_{\text{SPE}} \approx 3.2\text{s}$  is shorter than expected from the population relaxation  $T_1 = 8.7\text{s}$ . Note that also the CPM signal for an initial phase of  $\gamma = 70^\circ$  shows a shorter decay time than expected from relaxation on the transition A.

Concerning this issue, the SPE data (black, hollow squares) in figure 5.13 re-

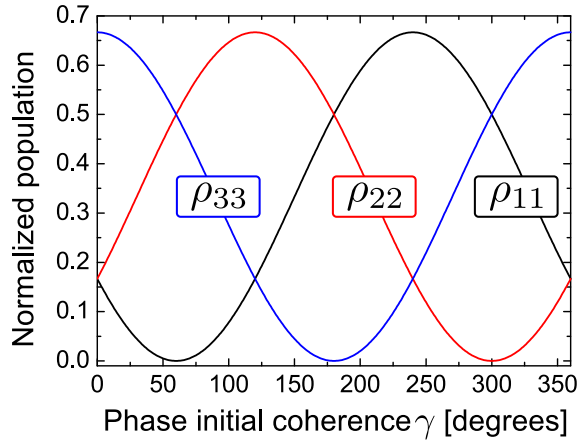


Figure 5.14: Dependence of the population distribution after the CPM write sequence on an initial coherence, created by a  $\pi/2$  pulse with a varying phase  $\gamma$ .  $\rho_{ii}$  is the population in state  $|i\rangle$  ( $i = 1, 2, 3$ ).

veal an interesting feature. For storage times shorter than  $\Delta\tau < 10$  ms, the signal exhibits a relatively fast decay. After 10 ms, the SPE signal stays almost constant for storage times up to a second, before a second decay starts and the signal finally vanishes. If we exclude the data on storage times below 10 ms, the signal decays indeed with a  $1/e$  time of  $\tau \approx 9$  s. Hence, there is a fast decay mechanism on a short timescale, which is most probably not related to population relaxation. Note that also the CPM data show this behaviour on short time scales.

At this stage of our work, we can only speculate on what might cause this fast decay. One mechanism that acts faster than population relaxation is spectral diffusion (see chapter 1.5). It typically occurs on timescales of ms and shifts transition frequencies of the ground state RF transitions as well as the optical transitions. However, the frequency shift is only of the order of 100 Hz for the RF transitions and thus rather small. Furthermore, the SPE pulses are spectrally broad and cover the whole inhomogeneous linewidth. This includes transitions that have been frequency shifted by spectral diffusion, e.g., outside the RF pit. In general, spectral diffusion changes the spectral configuration of the medium after the SPE or CPM write pulses. Therefore, the read pulses act on a different configuration, e.g., the RF pit has changed slightly its form and the frequency components of the stored information are slightly mixed. However, to our up to date knowledge this should not affect the read out efficiency.

Another fast decay mechanism is decoherence. With a decoherence time of  $T_2 = 500 \mu\text{s}$  all coherences should have vanished after  $\approx 1$  ms. However, there might still be an influence that is not included in our theoretical approach. Certainly, there is a need for further measurements beyond the proof of principle measurements presented here. That is why we suggest to apply SPE and CPM to a different storage medium with different decoherence times or spectral diffusion properties. Another rare-earth-ion doped crystal, europium doped YSO (EuYSO) (see e.g., [33]), is currently implemented as a storage medium in our group. EuYSO exhibits different spectroscopic properties than PrYSO. Applying SPE and CPM might thus help to investigate the influence of decoherence and spectral diffusion on the SPE and CPM signal decay. It might as well serve as a second proof of the capability of CPM to store arbitrary coherent information for durations as long as the population relaxation time.

However, the measurements presented in this thesis deviate only very little

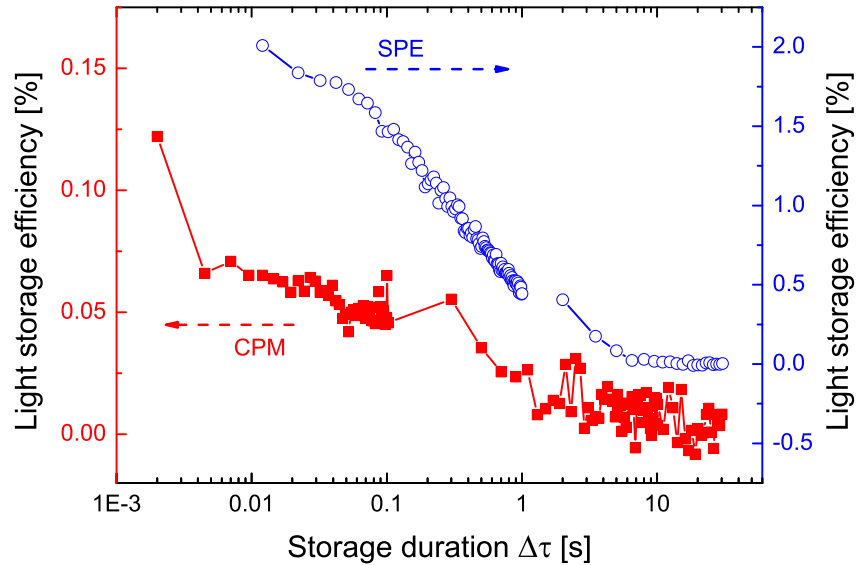


Figure 5.15: Light storage efficiency after applying CPM (red, solid, squares) or SPE (blue, hollow circles) versus storage duration  $\Delta\tau$ . Note the different axis scaling for the two curves.

from theoretically predicted results. They already work very well and are understood to a high degree. The signals decay almost on the timescale of the population relaxation times of the involved transitions, which is the dependency we expect from a coherence population mapping protocol

### 5.4.3 Light Storage with CPM and SPE

In a last measurement we test the novel CPM protocol on optically driven coherences after EIT-based light storage. In order to prepare these coherences, we use the preparation and light storage sequence described in chapter 4.4.5 with a slightly changed preparation control power of  $P = 5$  mW and a control write and read power for EIT-based light storage of  $P = 40$  mW.

Figure 5.15 shows the overall light storage efficiency versus storage duration for coherences restored with CPM (blue, solid circles) and SPE (red, hollow squares). The overall light storage efficiency is defined as the ratio between incoming and retrieved probe pulse. Note that this involves the efficiency of the light storage process as well as the efficiency of the used mapping protocol. However, we used the same light storage process for CPM and SPE experiments. This allows a direct comparison of the two protocols from the efficiency data.

Figure 5.15 shows that both mapping protocols enable the restoration of a stored probe light field. However, both protocols yield only little absolute efficiency of maximum 2%. In addition, the signal restored with CPM is a factor of 1/15 less than the signal restored with with SPE.

One reason comes with the population distribution after the respective CPM or SPE read sequences and the related absorption of the probe and control beam. In case of SPE, the population is equally distributed among states  $|1\rangle$  and  $|2\rangle$ . After CPM, the population is equally distributed among all three levels in the hyperfine



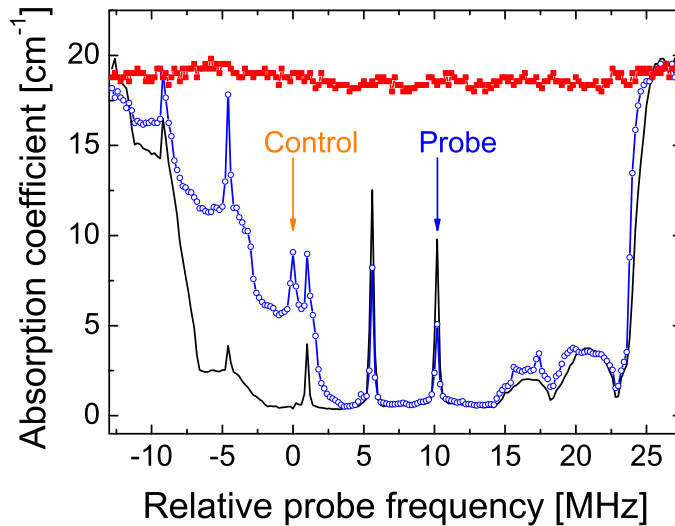


Figure 5.16: Absorption spectrum before (black line) and after a light storage experiment with CPM (red, solid squares) and SPE (blue, hollow circles). Control and probe indicate the frequencies of the corresponding light fields in the light storage experiment.

ground state of PrYSO. Figure 5.16 shows the absorption spectra before a light storage experiment (black line) and after an SPE (blue, hollow circles) or a CPM sequence (red, solid squares). SPE causes an enhanced absorption for the control beam, indicating non negligible population in state  $|1\rangle$  of the  $\Lambda$ -system used for light storage. Thus not all control power is used to open an EIT window and the associated loss-free propagation of the probe beam through the storage medium. At the same time, the system is no more in the dark state as discussed in chapter 3.2.1. This further reduces the light storage efficiency by involving unwanted couplings between the dark and bright states in the coupled three-state system.

For CPM, the situation is even worse. The equal distribution among all three levels causes the spectral pit to vanish entirely. Thus, the control field is absorbed to an even higher portion. In addition, the previously emptied state  $|3\rangle$  causes additional absorption of the retrieved probe beam. Note that no EIT condition exists for the transitions from state  $|3\rangle$  to the excited states, because the two photon detuning of probe and control beam,  $\Delta\nu = 10.19\text{ MHz}$ , does not match any transition involving the third state, i.e.,  $|1\rangle \leftrightarrow |3\rangle$  ( $\Delta\nu = 27.5\text{ MHz}$ ) or  $|2\rangle \leftrightarrow |3\rangle$  ( $\Delta\nu = 17.31\text{ MHz}$ ). Thus, inefficient read out due to control beam absorption is accompanied by enhanced probe beam absorption.

Another reason for a reduced performance with CPM is the weak coverage of the inhomogeneous broadening on the  $|2\rangle \leftrightarrow |3\rangle$  transition by the B pulses. Therefore CPM does not efficiently map coherences that have been prepared outside the frequency bandwidth of the B pulses. EIT-based light storage on the other hand prepares coherences in the full inhomogeneously broadened transition  $|1\rangle \leftrightarrow |2\rangle$ . Remember that for light storage we do not prepare an RF pit. Thus, CPM loses efficiency compared to SPE, which uses only A pulses that are spectrally broad enough to cover the full inhomogeneous broadening and to interact with all coherences prepared during light storage.

Figure 5.15 reveals a second feature, i.e., both signals decay with approximately the same  $1/e$  time of  $\tau \approx 0.5\text{ s}$ . This is much lower than expected from the previous measurements with RF induced coherences.

First of all we note that efficiency reducing effects should not have an influence

on the storage time. They only affect the read-out process itself. The reduction of the storage time by an order of magnitude must have a different origin. To date we could not identify a particular reason for this observation. However, we performed measurements to rule out some possible influences on storage duration (see Appendix C for the individual measurements). First we suspected the missing RF pit and corresponding errors due to weak pulses B to have some influence. Thus we performed an all-RF experiment with SPE for an initial phase of  $\gamma = 160^\circ$  without RF pit, but the result was similar to the one shown in figure 5.13, i.e., SPE with an RF pit.

In a next step we did not use a specific initial phase  $\gamma$ . Unlike in all previous RF experiments, we implemented a waiting time  $T = 100 \mu\text{s}$  between the data pulse and the write sequence. This time is longer than the dephasing time  $\sim 10 \mu\text{s}$ . Thus the initial coherence contains all possible phases when we apply CPM or SPE. This situation is very similar to a light storage experiment in the sense that coherences with all phases are prepared in the medium. However, also restoring a dephased macroscopic coherence yielded similar decay times. Thus we can rule out the influence of the RF pit and the influence of a dephased coherence as a reason of storage time limitation.

Another specific issue is that SPE does not preserve all phases equally well. It restores a coherence that does not have the exact initial phase distribution (see section 5.2.1) and some coherences are entirely lost. This is a complicated situation to think about in a light storage experiment. However, CPM does store the phases equally well. We proved this with the data in figure 5.11. But both protocols yield the same signal decay time. Thus we can rule out a storage time limitation due to the specific issue of phase sensitivity as well.

To date, these have been the thoughts and measurements on what might have limited the storage duration when CPM and SPE are applied in combination with light storage. In summary we believe that the limitation has its origin in the combination of CPM (or SPE) and EIT-based light storage, because CPM and SPE proved to work fine in RF experiments. Also light storage on the basis of EIT was used for storing information on ultra-long timescales up to a minute [26]. Thus the individual techniques do not show this storage duration limitation.

In order to perform further experiments with CPM on optically driven coherences, we suggest a slightly different CPM scheme. Instead of using only RF pulses that act on all praseodymium ions in the crystal, we could use optical pulses, which act on the specific light storage ensemble only. This involves an optically excited state which is subject to a fast population decay. However, an additional optical pulse could transfer population to a long lived shelving ground state similar to the approach in [5]. The proposed scheme would exclusively interact with the ensemble that carries the stored light signal. This might help to reduce the problems with RF-CPM for EIT-based light storage.

## Conclusions and Future Work

This work had three objectives to improve an EIT-based, solid-state memory for light. First, we set up a solid-state-laser system for radiation at the wavelength  $\lambda = 606$  nm, i.e., the optical transition in our storage medium, the rare-earth-ion doped crystal PrYSO. Second, we implemented efficient rephasing of optically driven coherences after EIT-based light storage by means of rapid adiabatic passage (RAP) pulses. Last but not least we implemented a novel coherence population mapping (CPM) protocol in order to shelve fragile atomic coherences in robust and long-lived populations in PrYSO.

**Solid-State-Laser System:** We developed a solid-state-laser system based on two nonlinear processes, optical parametric oscillation (OPO) and intra-cavity sum-frequency generation (SFG). The system is designed to generate continuous wave output in the orange part of the visible spectrum. OPO and SFG are implemented on a periodically poled lithium niobate crystal (PPLN). The crystal is divided into sections with appropriate poling periods for quasi phase matching of OPO and SFG. In addition, the poling period changes along the crystal height to allow tuning of the OPO-SFG output wavelength. The system provides output in a range between  $\lambda_{\text{vis}} = 605$  nm and  $\lambda_{\text{vis}} = 616$  nm with an output power  $P_{\text{vis}} > 1$  W. For light storage experiments, we operate the OPO-SFG at  $\lambda = 606$  nm with a maximum available output power of  $P_{\text{vis}} = 1.3$  W. An external Pound-Drever-Hall (PDH) frequency stabilization reduces the laser linewidth to  $\Delta\nu \approx 60_{-10}^{+20}$  kHz on a time scale of 100 ms. The OPO-SFG provides stable output for more than 30 hours with a root-mean-square power jitter below 2%.

In comparison to a previously used dye laser, the OPO-SFG requires less maintenance, performs more robust against external temperature fluctuations and vibrational noise and allows easier (re-) alignment. It performs slightly better in terms of frequency stability and the two systems are comparable in terms of output power. Dye lasers on the other hand provide a larger tuning range.

Future work should include a revised crystal design, i.e., a reversed section order of OPO and SFG on the PPLN crystal. This has been suggested to yield higher efficiency and output stability. In addition, we use three discrete poling periods in the SFG section, whereas the OPO section consists of a fanned poling structure. A double-fanned structure could provide enhanced tunability and help to partially suppress power fluctuations for different output wavelength. In addition, it should be possible to further reduce the laser-frequency linewidth by revising the locking loop or using a higher finesse cavity for the PDH stabilization.

**Adiabatic Rephasing of Atomic Coherences:** We experimentally implemented rephasing of optically driven coherences in PrYSO by RAP pulses. As a feature of adiabatic pulses, the parameters for RAP are defined in loose boundaries given by the adiabaticity criterion. This makes RAP potentially robust to parameter fluctuations. We experimentally verified this property and showed that rephasing with RAP provides superior performance compared to rephasing with  $\pi$  pulses. In particular, RAP provides enhanced robustness against variations in the Rabi frequency, pulse detuning and spatial inhomogeneity of the driving field. In our specific (3 mm long) PrYSO crystal and for standard experimental parameters, RAP yielded a factor of 1.15 higher rephasing efficiency compared to rephasing with  $\pi$  pulses. This value further increased when we artificially increased experimental imperfections or performed experiments with lower maximum Rabi frequencies. Concluding, RAP provides higher efficiency and more robust performance than  $\pi$  pulses in inhomogeneously broadened media, in the case of low available driving field power and for driving field inhomogeneities. However, RAP pulses typically require longer pulse durations than  $\pi$  pulses. This can cause heating or prevent the use of RAP when fast rephasing is required. An alternative to adiabatic pulses are, e.g., composite pulses or single-shot-shaped pulses. These are investigated in the context of another Ph.D thesis [87].

**Coherence Population Mapping:** We implemented a novel CPM protocol to store atomic coherences in long-lived populations in PrYSO. CPM works in any three-state system and does not require complex setups beyond a radiation source to generate a short write and read sequence. As an important feature, CPM stores arbitrary coherences equally well in the populations of a three-state system, i.e., CPM does neither require inhomogeneous broadening, nor is the storage efficiency dependent on the phase of the initial coherence. To our best knowledge, this exhibits a unique feature, which no other coherence population mapping protocol provides. Thus, CPM is an alternative to the stimulated photon echo (SPE), which requires inhomogeneous broadening to map an arbitrary initial coherence onto populations. However, the maximum retrieval efficiency with CPM is 1/3 of the initial coherence amplitude (and 1/2 with SPE).

We experimentally verified the main characteristics of both protocols with RF driven mapping sequences and RF induced initial coherences. Our results confirm phase-insensitive storage with CPM and storage times reaching the minute regime, i.e., the population relaxation time.

We also tested CPM in combination with EIT-based light storage. However, we obtained retrieval efficiencies below 1% and we observed reduced storage durations (for both SPE and CPM) compared to our previous experiments with RF induced coherences. A major contribution to the reduced efficiency is due to the fact that light storage works in a specific ensemble in the inhomogeneously broadened optical line in PrYSO. Our specific CPM (and SPE) pulses on the other hand couple to more ensembles and cause enhanced absorption for the retrieved signal. Future work should thus focus on the implementation of optical CPM to address only the ensemble used for light storage. Regarding a reduced storage duration, we could not yet find an explanation and suggest to implement CPM in different storage media to further investigate the limitation of storage duration.

# Zusammenfassung

Die vorliegende Dissertation ist thematisch auf dem Gebiet der Quanten-Informationsverarbeitung angesiedelt. Von Quanteninformation und deren Verarbeitung spricht man, wenn die zugrunde liegenden Wechselwirkungsmechanismen maßgeblich durch die Gesetze der Quantenmechanik bestimmt werden. Ein vielversprechender Ansatz zur Quanten-Informationsverarbeitung ist die Wechselwirkung zwischen Quantensystemen und Licht als effizientem Informationsträger [3,4]. Zukünftige Kommunikations- und Rechnernetzwerke benötigen daher Quanten-Speicher für optische Information.

Diese Arbeit ist Teil eines Projektes, das die Entwicklung und Optimierung eines solchen Quanten-Speichers für Licht zum Ziel hat. Als Speichermedium dient dabei der Seltenerd-dotierte Kristall PrYSO. Seltenerd-dotierte Kristalle besitzen schmale homogene Linienbreiten, die mit denen von Gasen vergleichbar sind. Gleichzeitig eignen sie sich als Festkörper aufgrund leichter Handhabung auch für den Einsatz außerhalb des Laborbetriebes. Zur Speicherung von Licht manipuliert ein Kontroll-Laser die dispersiven und absorptiven Eigenschaften des Speichermediums derart, dass es für einen Daten-Lichtpuls zunächst transparent wird. Dieser Effekt wird elektromagnetisch induzierte Transparenz (EIT) genannt. Mittels EIT ist es dann möglich, den Lichtpuls vollständig im Medium zu stoppen und in eine Vielzahl aus Überlagerungen atomarer Zustände zu übertragen. In dieser atomaren *Kohärenz* ist der volle Quantenzustand des Lichtpulses gespeichert und kann zu einem späteren Zeitpunkt wieder ausgelesen werden [9, 10]. Die maximal mögliche Speicherzeit für einen Lichtpuls ist dabei durch die Lebensdauer der atomaren Kohärenz, der Dekohärenzzeit  $T_2$  gegeben. Diese ist durch verschiedene Mechanismen limitiert und liegt typischerweise deutlich unter ihrem theoretischen Maximum, dem zweifachen der Besetzungs-Lebensdauer.

In PrYSO liegt die Dekohärenzzeit zunächst im Bereich weniger  $10 \mu\text{s}$ . Der Grund hierfür ist die Dephasierung einzelner Kohärenzen, welche durch die inhomogene Verbreiterung des Kohärenzübergangs verursacht wird. Dephasierung führt zu destruktiver Interferenz und verhindert so ein Auslesen der optischen Information. Mittels gepulster, magnetischer Wechselfelder kann dieser Effekt kompensiert werden. Hierzu werden meist  $\pi$  Pulse verwendet, deren Parameter klar definiert sind und deshalb präzise kontrolliert werden müssen. In dieser Arbeit wurden hingegen adiabatische Pulse zur Rephasierung verwendet, deren Parameter ohne Effizienzverlust in einem breiteren Bereich variiert werden können. Die Grenzen sind lediglich lose durch ein sogenanntes Adiabaskriterium definiert [23,24]. In Kapitel 4 wurde gezeigt, dass die Rephasierung atomarer Kohärenzen mittels des adiabatischen Pulses *rapid adiabatic passage* (RAP) deutlich

robuster ist als die Rephasierung mittels  $\pi$  Pulsen. In einer Reihe systematischer Messungen wurde gezeigt, dass dies insbesondere bei geringer verfügbarer Leistung für die Rephasierungspulse oder räumlichen Inhomogenitäten des magnetischen Wechselfeldes der Fall ist. In einem typischen Experiment wurde mit RAP im Vergleich zum Einsatz von  $\pi$  Pulsen die Speichereffizienz um 15% gesteigert. Dieser Wert erhöht sich weiter, sobald Feldinhomogenitäten zunehmen oder die Leistung des Magnetfeldes auf geringere Werte limitiert ist.

Nach erfolgreicher Rephasierung beträgt die Dekohärenzzeit in PrYSO etwa  $500 \mu\text{s}$ , ein Wert der immer noch deutlich unter der Besetzungslebensdauer im Bereich mehrerer 10 s liegt. Die Ursache hierfür ist eine fluktuierende Kristallumgebung, die zu stochastischen Phasenänderungen einzelner Kohärenzen führt. Eine gängige Strategie zur Minimierung dieses Effektes ist der Einsatz präzise gewählter statischer Magnetfelder und einer Vielzahl hochfrequenter Magnetfeldpulse. So wurden bereits Dekohärenzzeiten im Bereich von einer Minute erreicht [26], die Speicherexperimente werden gleichzeitig aber komplex und schwer handhabbar. Kapitel 5 stellt eine alternative Technik zur Verlängerung der Speicherzeit vor. Sie basiert auf der Übertragung der Kohärenzinformation in eine langlebige Besetzungsverteilung (englisch: *coherence population mapping*, kurz CPM). Durch eine kurze Lese- und Schreibsequenz werden Amplitude und Phase der Kohärenz auf eine Besetzungsverteilung in einem Dreiniveausystem übertragen und wieder ausgelesen. Die Speicherzeit ist dabei nur noch durch die Lebensdauer der Besetzungen begrenzt. Das neuartige CPM Protokoll hebt sich dabei von dem bekannten stimulierten Photonenecho ab, welches zwingend ein inhomogen verbreitertes Medium benötigt um eine Kohärenz unabhängig von ihrer Phase zu speichern [30, 31]. Die Information ist hierbei unterschiedlich auf eine Vielzahl von Einzelsystemen verteilt. CPM hingegen speichert die volle Information in einem einzelnen Dreiniveausystem bzw. in jedem atomaren System innerhalb des Speichermediums gleichwertig. Eine Speicherung ist dann in homogen und inhomogen verbreiterten Speichermedien unabhängig von der Kohärenzphase möglich [80, 81]. Innerhalb dieser Arbeit konnten die genannten Merkmale von CPM erstmals experimentell bestätigt werden. Atomare Kohärenzen, die mittels magnetischer Wechselfelder präpariert wurden, konnten so bis in den Bereich einiger Minuten gespeichert werden. In Kombination mit EIT basierter Lichtspeicherung wurde bisher aber nur eine geringe Speichereffizienz erreicht und Licht lediglich bis zu einer halben Sekunde gespeichert. Die Ursache hierfür ist noch nicht abschließend geklärt und Kapitel 5 beinhaltet auch Vorschläge für weiterführende Untersuchungen.

Das dritte Ziel dieser Arbeit war der Aufbau und die Implementierung eines Festkörper-Lasersystems zur Kopplung des relevanten optischen Übergangs in PrYSO bei  $\lambda = 606 \text{ nm}$  (s. Kapitel 2). Strahlung bei dieser Wellenlänge wurde bisher von einem Farbstofflaser erzeugt. Diese Systeme erfüllen die Anforderungen hoher Ausgangsleistung und guter Frequenzstabilität, jedoch sind dafür komplexe optische Resonatoren und ein hoher Wartungsaufwand nötig. Farbstofflaser eignen sich daher nur bedingt für (zukünftige) Anwendungen außerhalb des Laborbereichs. Im Rahmen dieser Arbeit wurde mit der Firma Aculight ein Lasersystem entwickelt und aufgebaut, das mittels optisch parametrischer Oszillation

und Summenfrequenzmischung Strahlung bei  $\lambda = 1064$  nm in sichtbare Strahlung im Bereich um  $\lambda = 606$  nm konvertiert. Dieses System zeichnet sich durch eine kompakte und robuste Bauweise aus, auch weil beide Frequenzmischprozesse auf einem einzigen, periodisch gepolten Lithiumniobat Kristall implementiert sind. Dabei sorgen Bereiche bestimmter periodischer Polung für die quasi Phasenanpassung der entsprechenden Mischprozesse. Das spezielle Design der Polungsstruktur auf dem Kristall erlaubt Ausgangsstrahlung in einem Wellenlängenbereich von  $\lambda = 605$  nm bis  $\lambda = 616$  nm mit über 1 W Ausgangsleistung. Durch eine externe Pound Drever Hall Stabilisierung wird die Frequenz des Lasersystems auf eine Linienbreite von unter 100 kHz stabilisiert.

Damit wurde während dieser Arbeit der EIT basierte Festkörper-Speicher zu einem reinen Festkörperexperiment ausgeweitet, in dem mit geringem Aufwand Speicherzeiten für atomare Kohärenzen bis in den Minutenbereich demonstriert wurden.

## Appendix A

### Ground-State Population-Relaxation Times

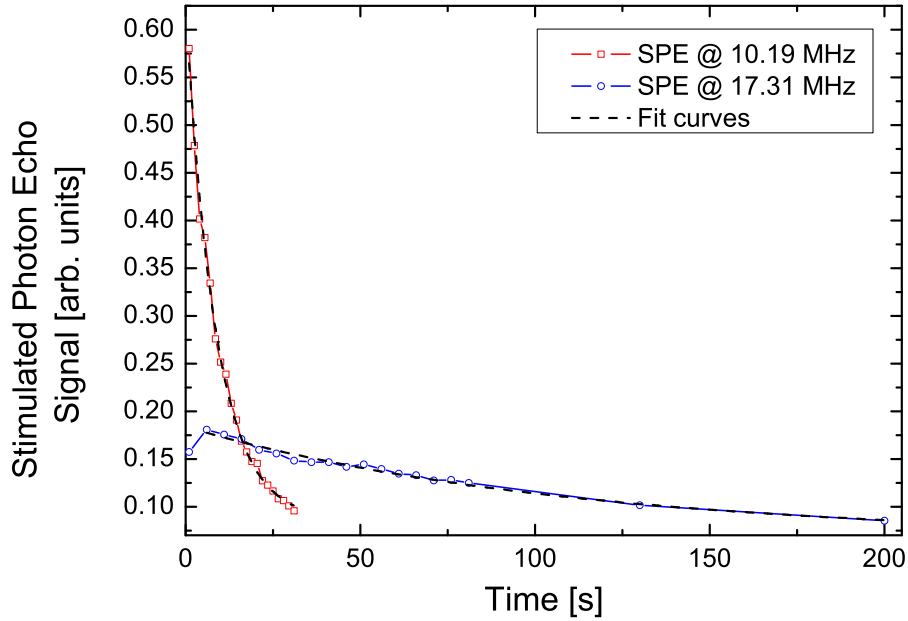


Figure A.1: Stimulated photon echo measurements used to determine the population relaxation times in two hyperfine ground state transitions of PrYSO.

Figure A.1 shows zero time delay SPE measurements on the  $|\pm 1/2\rangle \leftrightarrow |\pm 3/2\rangle$  and the  $|\pm 3/2\rangle \leftrightarrow |\pm 5/2\rangle$  hyperfine ground state transition in PrYSO. The SPE decay depends on spectral diffusion on short timescales ( $< 1$  ms) and only on population relaxation in the corresponding transition on longer timescales. Thus we can deduce the population relaxation time from SPE measurements on long timescales. For a detailed description of SPE see chapter 5.2.1 or, e.g., SPE used for spectroscopy [33, 82] and references therein. The sequence used for these measurements was the same as described in chapter 5.3.4.  $\pi/2$  pulses on the  $|\pm 1/2\rangle \leftrightarrow |\pm 3/2\rangle$  transition with frequency  $\nu = 10,19$  MHz had durations of  $\tau = 1.7 \mu\text{s}$ .  $\pi/2$  pulses on the transition  $|\pm 3/2\rangle \leftrightarrow |\pm 5/2\rangle$  with frequency  $\nu = 17,31$  MHz had durations of  $\tau = 5 \mu\text{s}$ . The initial coherence had a phase of  $\gamma = 0^\circ$ . An exponential function fitted to each curve yields population relaxation times of  $T_1 = 8.67\text{s}$  on the  $|\pm 1/2\rangle \leftrightarrow |\pm 3/2\rangle$  transition and  $T_1 = 109.5\text{s}$  on the  $|\pm 3/2\rangle \leftrightarrow |\pm 5/2\rangle$  transition.



## Appendix B

## Laser-Linewidth Measurement via Spectral Holeburning

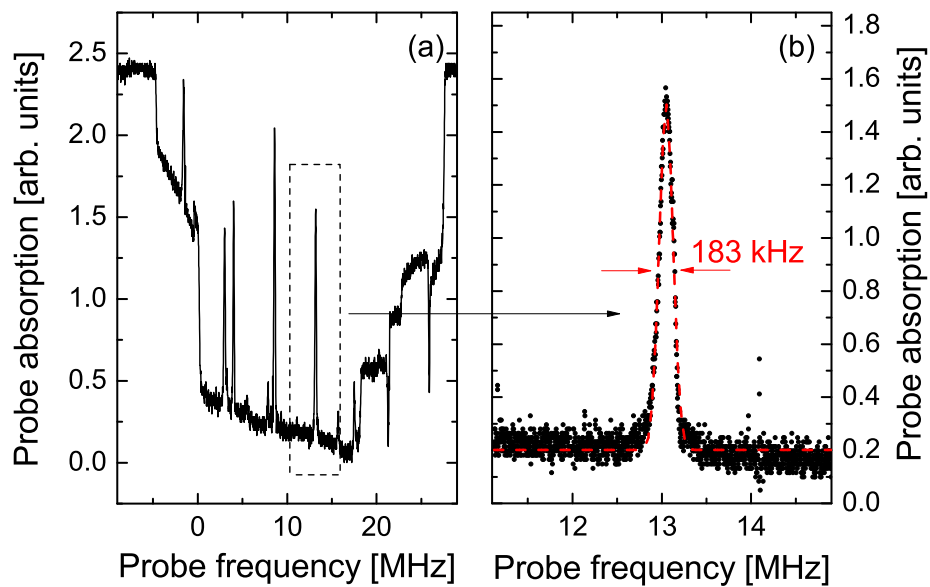


Figure B.1: Absorption spectrum in PrYSO, used to deduce the laser linewidth of the OPO-SFG laser system.

Figure B.1 (a): The figure shows a spectral pit with absorption lines in PrYSO, generated and probed by laser pulses from the frequency stabilized OPO-SFG laser system. The absorption spectrum was prepared with a sequence similar to the one described in chapter 4.4.5. Figure B.1 (b): We use one of the absorption lines to estimate the laser linewidth: The absorption line has a width of  $\Delta\nu = 183$  kHz (FWHM). We assume this width to be a convolution of the following contributions: (1) Two Lorentzian-shaped saturation broadenings generated by the optical pumping process to prepare the absorption line ( $\Delta\nu = 23$  kHz) and by the probe process to detect it ( $\Delta\nu = 16$  kHz). (2) The Fourier bandwidth of the pump and probe pulses (below 1 kHz). (3) Gaussian-shaped frequency noise or laser linewidth, respectively, during the two laser pulses. From these contributions and the measured absorption linewidth, we deduce an upper limit for the laser linewidth of  $\Delta\nu < 114$  kHz (FWHM) on a time scale  $\Delta t \approx 1$  ms.

## Appendix C

## Supplementary CPM and SPE Measurements

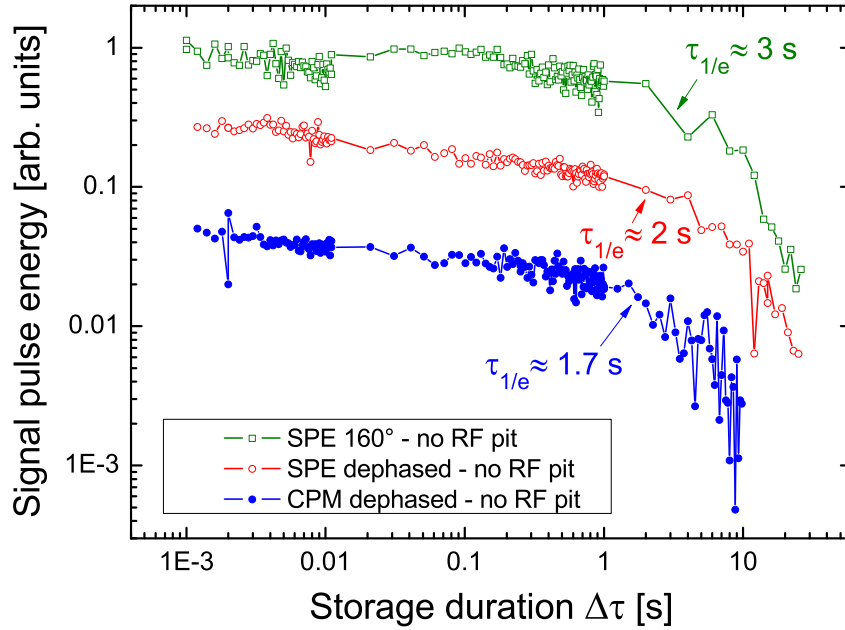


Figure C.1: Retrieved signals with CPM and SPE, acting on different RF induced coherences, versus storage duration  $\Delta\tau$ .

Figure C.1 shows supplementary measurements with SPE and CPM to investigate short storage durations for optically driven coherences mapped with SPE or CPM (see discussion in chapter 5.4.3). During all measurements we used the preparation described in chapter 5.3.4 without preparing an RF pit. The green, hollow squares represent the retrieved signal after an SPE measurement with an RF induced initial coherence with a phase  $\gamma = 160^\circ$  versus a scan of the storage duration. The red, hollow circles show the same quantity for a dephased initial coherence, i.e., we implemented a waiting time  $T = 100 \mu\text{s}$  between the data and the writing pulse. The blue, solid circles show the retrieved signal energy for CPM with an initially dephased coherence, i.e., the same time delay  $T = 100 \mu\text{s}$  between data pulse and writing sequence.

The data exhibit  $1/e$  decay times in the range of  $\sim 2 \text{ s}$ , i.e., longer than the observed decay times for stored light signals, which are in the range of  $\sim 0.5 \text{ s}$ . Dephasing and the missing RF pit are thus excluded as possible effects that reduce the storage duration for optically driven coherences mapped with CPM or SPE.

## Appendix D

### Single- and Two-Frequency Impedance-Matching

In this appendix, we give a more detailed description on how to calculate tuning and matching capacitors and wave traps for the impedance matching circuits described in chapters 4.4.3 and 5.3.2.

#### Single-Frequency Impedance-Matching

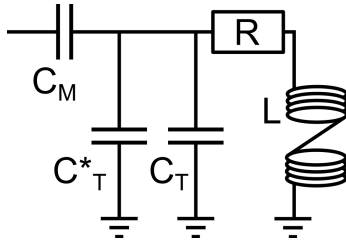


Figure D.1: Schematic electronic circuit of a single-frequency impedance-matching for RF coils ( $L$ ).

We start with the single-frequency impedance-matching circuit (see figure D.1), which is the basis for the two-frequency impedance-matching circuit.

The RF coils have an inductance  $L$ , tuning capacitor and matching capacitor are denoted  $C_T$  and  $C_M$ ,  $R$  is the resistance of the leads to the RF coils and  $\omega$  is the angular frequency of the RF current we want to transfer from the amplifier with a real impedance  $R_0$  to the RF coils. We find a maximum power transfer if the impedance  $Z$  of the matched RF coil is equal to the impedance of the amplifier. This condition reads  $\text{Im}[Z] = 0$  and  $\text{Re}[Z] = R_0 = 50\Omega$  and the overall impedance  $Z$  for our specific circuit reads

$$Z = \frac{1}{i\omega C_M} + \left( i\omega C_T + \frac{1}{R + i\omega L} \right)^{-1} = \frac{1}{i\omega C_M} + \frac{1}{i\omega C_T + Z_V^{-1}} \quad (\text{D.1})$$

Note that parasitic capacitances  $C_T^*$ , e.g., from coaxial cables, add linearly to the tuning capacitance  $C_T$ . The values for tuning (including parasitic capacitance) and matching capacitor are calculated to

$$C_M = \frac{R}{R_0} \frac{1}{\omega \sqrt{\frac{R}{R_0} (R^2 + \omega^2 L^2) - R^2}} \approx \frac{1}{\omega^2 L} \sqrt{\frac{R}{R_0}} \quad (\text{D.2})$$

$$C_T = \frac{\omega L - \sqrt{\frac{R}{R_0} (R^2 + \omega^2 L^2) - R^2}}{\omega (R^2 + \omega^2 L^2)} \approx \frac{1}{\omega^2 L} \left( 1 - \sqrt{\frac{R}{R_0}} \right) \quad (\text{D.3})$$

The approximation holds true, when  $R^2 \ll \omega^2 L^2$ , which is the case for our setup with  $\mu\text{H}$  inductance of the RF coil, angular frequencies in the 10 MHz range and a resistance  $R < 1\Omega$ .

## Two-Frequency Impedance-Matching

Impedance matching for two frequencies is realized by a combination of two single-frequency matching-circuits and two additional wave traps (each for a frequency) as shown in figure 5.7. The entire circuit is described by a parallel connection of two individual branches (ideally each for a certain frequency). These branches have the impedance  $Z_1$  and  $Z_2$  and read

$$Z_1 = \frac{1}{i\omega C_{M1}} + \frac{1}{i\omega C_{T1} + Z_{WT2}^{-1} + (Z_V + (Z_{WT1}^{-1} + i\omega C_{T2})^{-1})} \quad (\text{D.4})$$

$$Z_2 = \frac{1}{i\omega C_{M2}} + \frac{1}{i\omega C_{T2} + Z_{WT1}^{-1} + (Z_V + (Z_{WT2}^{-1} + i\omega C_{T1})^{-1})} \quad (\text{D.5})$$

with the impedance  $Z_{WT}$  for the wave trap, a series connection of a capacitor and a coil.

We now assume a wave with frequency  $\omega_1$  entering the circuit. Note that the wave traps are resonant for a specific frequency  $\omega_1$  or  $\omega_2$ , and for a wave with frequency  $\omega_1$  we find  $Z_{WT1} = 0$  and  $Z_{WT2} \rightarrow \infty$ . With these assumptions, the impedance of each branch turns into

$$Z_1 = \frac{1}{i\omega C_{M1}} + \frac{1}{i\omega C_{T1} + Z_V} \quad (\text{D.6})$$

$$Z_2 = \frac{1}{i\omega C_{M2}} \quad (\text{D.7})$$

The resulting impedance for the entire circuit is thus a parallel connection of a single frequency impedance matching circuit (compare equation (D.1)) and the matching capacitor  $C_{M2}$ . In order to match the RF coils for both frequencies, it is convenient to begin with the values obtained from equations (D.3). In an iterative manner, the influence of  $C_{M2}$  and  $C_{M1}$  can be compensated by the other components of the circuit.

## Bibliography

- [1] E. Knill, R. Laflamme, and G. J. Milburn. *A scheme for efficient quantum computation with linear optics*. Nature **409**(6816) 46 (2001). URL <http://dx.doi.org/10.1038/35051009>
- [2] H. J. Kimble. *The quantum internet*. Nature **453**(7198) 1023 (2008). URL <http://dx.doi.org/10.1038/nature07127>
- [3] C. Simon, M. Afzelius, J. Appel, A. Boyer de la Giroday, S. J. Dewhurst, N. Gisin, C. Y. Hu, F. Jelezko, S. Kröll, J. H. Müller, J. Nunn, E. S. Polzik, J. G. Rarity, H. De Riedmatten, W. Rosenfeld, A. J. Shields, N. Sköld, R. M. Stevenson, R. Thew, I. A. Walmsley, M. C. Weber, H. Weinfurter, J. Wrachtrup, and R. J. Young. *Quantum memories*. The European Physical Journal D **58**(1) 1 (2010). URL <http://dx.doi.org/10.1140/epjd/e2010-00103-y>
- [4] A. I. Lvovsky, B. C. Sanders, and W. Tittel. *Optical quantum memory*. Nature Photonics **3**(12) 706 (2009). URL <http://dx.doi.org/10.1038/nphoton.2009.231>
- [5] M. Afzelius, C. Simon, H. de Riedmatten, and N. Gisin. *Multimode quantum memory based on atomic frequency combs*. Physical Review A **79**(5) 052329 (2009). URL <http://dx.doi.org/10.1103/PhysRevA.79.052329>
- [6] M. Hosseini, B. M. Sparkes, G. Campbell, P. K. Lam, and B. C. Buchler. *High efficiency coherent optical memory with warm rubidium vapour*. Nature Communications **2** 174 (2011). URL <http://dx.doi.org/10.1038/ncomms1175>
- [7] M. Fleischhauer and M. D. Lukin. *Dark-State Polaritons in Electromagnetically Induced Transparency*. Physical Review Letters **84**(22) 5094 (2000). URL <http://dx.doi.org/10.1103/PhysRevLett.84.5094>
- [8] A. V. Gorshkov, A. André, M. Fleischhauer, A. S. Sørensen, and M. D. Lukin. *Universal Approach to Optimal Photon Storage in Atomic Media*. Physical Review Letters **98**(12) 123601 (2007). URL <http://dx.doi.org/10.1103/PhysRevLett.98.123601>
- [9] S. E. Harris, J. E. Field, and A. Imamoglu. *Nonlinear optical processes using electromagnetically induced transparency*. Physical Review Letters **64**(10) 1107 (1990). URL <http://dx.doi.org/10.1103/PhysRevLett.64.1107>
- [10] M. Fleischhauer, A. Imamoglu, and J. P. Marangos. *Electromagnetically induced transparency: Optics in coherent media*. Review of Modern Physics **77**(2) 633 (2005). URL <http://dx.doi.org/10.1103/RevModPhys.77.633>

- [11] K.-J. Boller, A. Imamoglu, and S. E. Harris. *Observation of electromagnetically induced transparency*. Physical Review Letters **66**(20) 2593 (1991). URL <http://dx.doi.org/10.1103/PhysRevLett.66.2593>
- [12] D. F. Phillips, A. Fleischhauer, A. Mair, R. L. Walsworth, and M. D. Lukin. *Storage of Light in Atomic Vapor*. Physical Review Letters **86**(5) 783 (2001). URL <http://dx.doi.org/10.1103/PhysRevLett.86.783>
- [13] L. V. Hau, S. E. Harris, Z. Dutton, and C. H. Behroozi. *Light speed reduction to 17 metres per second in an ultracold atomic gas*. Nature **397**(6720) 594 (1999). URL <http://dx.doi.org/10.1038/17561>
- [14] W. Tittel, M. Afzelius, T. Chanelière, R. L. Cone, S. Kröll, S. A. Moiseev, and M. Sellars. *Photon-echo quantum memory in solid state systems*. Laser & Photonics Reviews **4**(2) 244 (2010). URL <http://dx.doi.org/10.1002/lpor.200810056>
- [15] G. J. Pryde, M. J. Sellars, and N. B. Manson. *Solid State Coherent Transient Measurements Using Hard Optical Pulses*. Physical Review Letters **84**(6-7) 1152 (2000). URL <http://dx.doi.org/10.1103/PhysRevLett.84.1152>
- [16] M. D. Lukin and P. R. Hemmer. *Quantum Entanglement via Optical Control of Atom-Atom Interactions*. Physical Review Letters **84**(13) 2818 (2000). URL <http://dx.doi.org/10.1103/PhysRevLett.84.2818>
- [17] N. Ohlsson, R. K. Mohan, and S. Kröll. *Quantum computer hardware based on rare-earth-ion-doped inorganic crystals*. Optics Communications **201**(1-3) 71 (2002). URL [http://dx.doi.org/10.1016/S0030-4018\(01\)01666-2](http://dx.doi.org/10.1016/S0030-4018(01)01666-2)
- [18] J. Wesenberg and K. Mølmer. *Robust quantum gates and a bus architecture for quantum computing with rare-earth-ion-doped crystals*. Physical Review A **68**(1) 012320 (2003). URL <http://dx.doi.org/10.1103/PhysRevA.68.012320>
- [19] J. Hough, D. Hils, M. D. Rayman, L.-S. Ma, L. Hollberg, and J. L. Hall. *Dye-laser frequency stabilization using optical resonators*. Applied Physics B **33**(3) 179 (1984). URL <http://dx.doi.org/10.1007/BF00688526>
- [20] O. Mhibik, D. Pabœuf, C. Drag, and F. Bretenaker. *Sub-kHz-level relative stabilization of an intracavity doubled continuous wave optical parametric oscillator using Pound-Drever-Hall scheme*. Optics Express **19**(19) 18049 (2011). URL <http://dx.doi.org/10.1364/OE.19.018049>
- [21] J.-M. Melkonian, T.-H. My, F. Bretenaker, and C. Drag. *High spectral purity and tunable operation of a continuous singly resonant optical parametric oscillator emitting in the red*. Optics Letters **32**(5) 518 (2007). URL <http://dx.doi.org/10.1364/OL.32.000518>
- [22] W. R. Bosenberg, J. I. Alexander, L. E. Myers, and R. W. Wallace. *2.5-W, continuous-wave, 629-nm solid-state laser source*. Optics Letters **23**(3) 207 (1998). URL <http://dx.doi.org/10.1364/OL.23.000207>

- [23] N. V. Vitanov, T. Halfmann, B. W. Shore, and K. Bergmann. *Laser-induced population transfer by adiabatic passage techniques*. Annual Review of Physical Chemistry **52** 763 (2001). URL <http://dx.doi.org/10.1146/annurev.physchem.52.1.763>
- [24] M. Garwood and L. DelaBarre. *The return of the frequency sweep: designing adiabatic pulses for contemporary NMR*. Journal of magnetic resonance **153**(2) 155 (2001). URL <http://dx.doi.org/10.1006/jmre.2001.2340>
- [25] E. Fraval, M. J. Sellars, and J. J. Longdell. *Method of Extending Hyperfine Coherence Times in  $Pr^{3+}Y_2SiO_5$* . Physical Review Letters **92**(7) 077601 (2004). URL <http://dx.doi.org/10.1103/PhysRevLett.92.077601>
- [26] G. Heinze, C. Hubrich, and T. Halfmann. *Stopped Light and Image Storage by Electromagnetically Induced Transparency up to the Regime of One Minute*. Physical Review Letters **111**(3) 033601 (2013). URL <http://dx.doi.org/10.1103/PhysRevLett.111.033601>
- [27] M. Zhong, M. P. Hedges, R. L. Ahlefeldt, J. G. Bartholomew, S. E. Beavan, S. M. Wittig, J. J. Longdell, and M. J. Sellars. *Optically addressable nuclear spins in a solid with a six-hour coherence time*. Nature **517**(7533) 177 (2015). URL <http://dx.doi.org/10.1038/nature14025>
- [28] L. Viola, E. Knill, and S. Lloyd. *Dynamical Decoupling of Open Quantum Systems*. Physical Review Letters **82**(12) 2417 (1999). URL <http://dx.doi.org/10.1103/PhysRevLett.82.2417>
- [29] W. Yang, Z.-Y. Wang, and R.-B. Liu. *Preserving qubit coherence by dynamical decoupling*. Frontiers of Physics **6**(1) 2 (2011). URL <http://dx.doi.org/10.1007/s11467-010-0113-8>
- [30] T. W. Mossberg, R. Kachru, S. R. Hartmann, and A. M. Flusberg. *Echoes in gaseous media: A generalized theory of rephasing phenomena*. Physical Review A **20**(5) 1976 (1979). URL <http://dx.doi.org/10.1103/PhysRevA.20.1976>
- [31] M. U. Staudt, S. R. Hastings-Simon, M. Nilsson, M. Afzelius, V. Scarani, R. Ricken, H. Suche, W. Sohler, W. Tittel, and N. Gisin. *Fidelity of an Optical Memory Based on Stimulated Photon Echoes*. Physical Review Letters **98**(11) 113601 (2007). URL <http://dx.doi.org/10.1103/PhysRevLett.98.113601>
- [32] S. Hübner. *Optical spectra of transparent rare earth compounds*. Academic Press, New York (1978)
- [33] A.A. Kaplyanskii and R.M. Macfarlane, eds. *Spectroscopy of Solids Containing Rare Earth Ions, Vol. 21 of Modern Problems in Condensed Matter Sciences*. North Holland Publishing Co. (Elsevier), Amsterdam (1987)

- [34] R. Yano, M. Mitsunaga, and N. Uesugi. *Ultralong optical dephasing time in  $\text{Eu}^{3+}:\text{Y}_2\text{SiO}_5$* . *Optics Letters* **16**(23) 1884 (1991). URL <http://dx.doi.org/10.1364/OL.16.001884>
- [35] R. W. Equall, Y. Sun, R. L. Cone, and R. M. Macfarlane. *Ultraslow optical dephasing in  $\text{Eu}^{3+}:\text{Y}_2\text{SiO}_5$* . *Physical Review Letters* **72**(14) 2179 (1994). URL <http://dx.doi.org/10.1103/PhysRevLett.72.2179>
- [36] B. A. Maksimov, Y. A. Kharitonov, V. V. Illyukhin, and N. V. Belov. *Crystal structure of Y-Oxysilicate  $\text{Y}_2(\text{SiO}_4)\text{O}$* . *Soviet Physics Doklady* **13**(11) 1188 (1969)
- [37] W. Y. Ching, L. Ouyang, and Y.-N. Xu. *Electronic and optical properties of  $\text{Y}_2\text{SiO}_5$  and  $\text{Y}_2\text{Si}_2\text{O}_7$  with comparisons to  $\alpha\text{-SiO}_2$  and  $\text{Y}_2\text{O}_3$* . *Physical Review B* **67**(24) 245108 (2003). URL <http://dx.doi.org/10.1103/PhysRevB.67.245108>
- [38] R. W. Equall, R. L. Cone, and R. M. Macfarlane. *Homogeneous broadening and hyperfine structure of optical transitions in  $\text{Pr}^{3+}:\text{Y}_2\text{SiO}_5$* . *Physical Review B* **52**(6) 3963 (1995). URL <http://dx.doi.org/10.1103/PhysRevB.52.3963>
- [39] J. J. Longdell, M. J. Sellars, and N. B. Manson. *Hyperfine interaction in ground and excited states of praseodymium-doped yttrium orthosilicate*. *Physical Review B* **66**(3) 035101 (2002). URL <http://dx.doi.org/10.1103/PhysRevB.66.035101>
- [40] M. Nilsson, L. Rippe, S. Kröll, R. Klieber, and D. Suter. *Hole-burning techniques for isolation and study of individual hyperfine transitions in inhomogeneously broadened solids demonstrated in  $\text{Pr}^{3+}:\text{Y}_2\text{SiO}_5$* . *Physical Review B* **70**(21) 214116 (2004). URL <http://dx.doi.org/10.1103/PhysRevB.70.214116>
- [41] B. S. Ham, P. R. Hemmer, and M. S. Shahriar. *Efficient electromagnetically induced transparency in a rare-earth doped crystal*. *Optics Communications* **144**(4–6) 227 (1997). URL [http://dx.doi.org/10.1016/S0030-4018\(97\)00423-9](http://dx.doi.org/10.1016/S0030-4018(97)00423-9)
- [42] N. Lorenz. *Optimising EIT Light Storage Efficiency in  $\text{Pr}^{3+}:\text{Y}_2\text{SiO}_5$* . M.Sc. thesis, Technische Universität Darmstadt (2014)
- [43] J. R. Klauder and P. W. Anderson. *Spectral Diffusion Decay in Spin Resonance Experiments*. *Physical Review* **125**(3) 912 (1962). URL <http://dx.doi.org/10.1103/PhysRev.125.912>
- [44] R. Yano, M. Mitsunaga, and N. Uesugi. *Stimulated-photon-echo spectroscopy. I. Spectral diffusion in  $\text{Eu}^{3+}:\text{YAlO}_3$* . *Physical Review B* **45**(22) 12752 (1992). URL <http://dx.doi.org/10.1103/PhysRevB.45.12752>



- [45] J. A. Armstrong, N. Bloembergen, J. Ducuing, and P. S. Pershan. *Interactions between Light Waves in a Nonlinear Dielectric*. Physical Review **127**(6) 1918 (1962). URL <http://dx.doi.org/10.1103/PhysRev.127.1918>
- [46] R. W. Boyd. *Nonlinear Optics*. Academic Press, Amsterdam (2008)
- [47] M. Yamada, N. Nada, M. Saitoh, and K. Watanabe. *First-order quasi-phase matched LiNbO<sub>3</sub> waveguide periodically poled by applying an external field for efficient blue second-harmonic generation*. Applied Physics Letters **62**(5) 435 (1993). URL <http://dx.doi.org/10.1063/1.108925>
- [48] L. E. Myers, R. C. Eckardt, M. M. Fejer, R. L. Byer, W. R. Bosenberg, and J. W. Pierce. *Quasi-phase-matched optical parametric oscillators in bulk periodically poled LiNbO*. Journal of the Optical Society of America B **12**(11) 2102 (1995). URL <http://dx.doi.org/10.1364/JOSAB.12.002102>
- [49] J. E. Midwinter and J. Warner. *The effects of phase matching method and of uniaxial crystal symmetry on the polar distribution of second-order non-linear optical polarization*. British Journal of Applied Physics **16**(8) 1135 (1965). URL <http://dx.doi.org/10.1088/0508-3443/16/8/312>
- [50] W. Sellmeier. *Zur Erklärung der abnormen Farbenfolge im Spectrum einiger Substanzen*. Annalen der Physik **219**(6) 272 (1871). URL <http://dx.doi.org/10.1002/andp.18712190612>
- [51] O. Gayer, Z. Sacks, E. Galun, and A. Arie. *Temperature and wavelength dependent refractive index equations for MgO-doped congruent and stoichiometric LiNbO<sub>3</sub>*. Applied Physics B **91**(2) 343 (2008). URL <http://dx.doi.org/10.1007/s00340-008-2998-2>
- [52] *Covesion Guide to PPLN*. URL <http://www.covesion.com/support/material-properties-of-lithium-niobate.html>
- [53] K. K. Wong, ed. *Properties of lithium niobate, Vol. 28 of EMIS data reviews series*. Inspec, London, rev. ed. edition (2002)
- [54] I. Shoji, T. Kondo, A. Kitamoto, M. Shirane, and R. Ito. *Absolute scale of second-order nonlinear-optical coefficients*. Journal of the Optical Society of America B **14**(9) 2268 (1997). URL <http://dx.doi.org/10.1364/JOSAB.14.002268>
- [55] F. S. Chen. *Optically Induced Change of Refractive Indices in LiNbO<sub>3</sub> and LiTaO<sub>3</sub>*. Journal of Applied Physics **40** 3389 (1969). URL <http://dx.doi.org/10.1063/1.1658195>
- [56] G. Moore and K. Koch. *Optical parametric oscillation with intracavity sum-frequency generation*. IEEE Journal of Quantum Electronics **29**(3) 961 (1993). URL <http://dx.doi.org/10.1109/3.206580>

- [57] R. W. P. Drever, J. L. Hall, F. V. Kowalski, J. Hough, G. M. Ford, A. J. Munley, and H. Ward. *Laser phase and frequency stabilization using an optical resonator*. Applied Physics B **31**(2) 97 (1983). URL <http://dx.doi.org/10.1007/BF00702605>
- [58] E. D. Black. *An introduction to Pound–Drever–Hall laser frequency stabilization*. American Journal of Physics **69**(1) 79 (2001). URL <http://dx.doi.org/10.1119/1.1286663>
- [59] D. Lowenthal. *CW periodically poled LiNbO<sub>3</sub> optical parametric oscillator model with strong idler absorption*. IEEE Journal of Quantum Electronics **34**(8) 1356 (1998). URL <http://dx.doi.org/10.1109/3.704319>
- [60] B. W. Shore. *Volume 1 of: The theory of coherent atomic excitation*. Wiley Interscience, New York (1990)
- [61] D. Meschede. *Optik Licht und Laser (3. Auflage)*. Vieweg+Teubner GWV Fachverlage GmbH, Wiesbaden (2008)
- [62] M. Bajcsy, A. S. Zibrov, and M. D. Lukin. *Stationary pulses of light in an atomic medium*. Nature **426**(6967) 638 (2003). URL <http://dx.doi.org/10.1038/nature02176>
- [63] G. Heinze. *Kohärente optische Datenspeicherung mittels EIT in einem Pr<sup>3+</sup>:Y<sub>2</sub>SiO<sub>5</sub>-Kristall*. Ph.D. thesis, Technische Universität Darmstadt (2013)
- [64] E. L. Hahn. *Spin Echoes*. Physical Review **80**(4) 580 (1950). URL <http://dx.doi.org/10.1103/PhysRev.80.580>
- [65] C. J. Hardy, W. A. Edelstein, D. Vatis, R. Harms, and W. J. Adams. *Calculated T<sub>1</sub> images derived from a partial saturation-inversion recovery pulse sequence with adiabatic fast passage*. Magnetic Resonance Imaging **3**(2) 107 (1985). URL [http://dx.doi.org/10.1016/0730-725X\(85\)90247-4](http://dx.doi.org/10.1016/0730-725X(85)90247-4)
- [66] R. A. De Graaf and K. Nicolay. *Adiabatic rf pulses: Applications to in vivo NMR*. Concepts in Magnetic Resonance **9**(4) 247 (1997). URL <http://dx.doi.org/10.1002/%28SICI%291099-0534%281997%299%3A4%3C247%3A%3AAID-CMR4%3E3.3.CO%3B2-A>
- [67] S. Conolly, G. Glover, D. Nishimura, and A. Macovski. *A reduced power selective adiabatic spin-echo pulse sequence*. Magnetic resonance in medicine **18**(1) 28 (1991). URL <http://dx.doi.org/10.1002/mrm.1910180105>
- [68] M. F. Pascual-Winter, R. C. Tongning, T. Chanelière, and J.-L. Le Gouët. *Securing coherence rephasing with a pair of adiabatic rapid passages*. New Journal of Physics **15**(5) 055024 (2013). URL <http://dx.doi.org/10.1088/1367-2630/15/5/055024>
- [69] M. F. Pascual-Winter, R. C. Tongning, R. Lauro, A. Louchet-Chauvet, T. Chanelière, and J.-L. Le Gouët. *Adiabatic passage with spin locking in*

- $Tm^{3+}$ :YAG. *Physical Review B* **86**(6) 064301 (2012). URL <http://dx.doi.org/10.1103/PhysRevB.86.064301>
- [70] R. Lauro, T. Chanelière, and J.-L. Le Gouët. *Adiabatic refocusing of nuclear spins in  $Tm^{3+}$ :YAG*. *Physical Review B* **83**(3) 035124 (2011). URL <http://dx.doi.org/10.1103/PhysRevB.83.035124>
- [71] M. M. T. Loy. *Observation of Population Inversion by Optical Adiabatic Rapid Passage*. *Physical Review Letters* **32**(15) 814 (1974). URL <http://dx.doi.org/10.1103/PhysRevLett.32.814>
- [72] G. Genov. (*personal communication*). To be published (2015)
- [73] G. Heinze. *Kohärente magnetisch Hochfrequenzanregungen eines seltenerd-dotierten Festkörpers*. Diplomarbeit, Technische Universität Kaiserslautern (2008)
- [74] J. Mispelter, M. Lupu, and A. Briguet. *NMR probeheads for biophysical and biomedical experiments*. Imperial College Press, London (2006)
- [75] F. Beil, J. Klein, G. Nikoghosyan, and T. Halfmann. *Electromagnetically induced transparency and retrieval of light pulses in a  $\Lambda$ -type and a V-type level scheme in  $Pr^{3+}$ : $Y_2SiO_5$* . *Journal of Physics B: Atomic, Molecular and Optical Physics* **41**(7) 074001 (2008). URL <http://dx.doi.org/10.1088/0953-4075/41/7/074001>
- [76] M. H. Levitt. *Composite pulses*. *Progress in Nuclear Magnetic Resonance Spectroscopy* **18**(2) 61 (1986). URL [http://dx.doi.org/10.1016/0079-6565\(86\)80005-X](http://dx.doi.org/10.1016/0079-6565(86)80005-X)
- [77] G. T. Genov, D. Schraft, T. Halfmann, and N. V. Vitanov. *Correction of Arbitrary Field Errors in Population Inversion of Quantum Systems by Universal Composite Pulses*. *Physical Review Letters* **113**(4) 043001 (2014). URL <http://dx.doi.org/10.1103/PhysRevLett.113.043001>
- [78] D. Schraft, T. Halfmann, G. T. Genov, and N. V. Vitanov. *Experimental demonstration of composite adiabatic passage*. *Physical Review A* **88**(6) 063406 (2013). URL <http://dx.doi.org/10.1103/PhysRevA.88.063406>
- [79] T. W. Mossberg. *Time-domain frequency-selective optical data storage*. *Optics Letters* **7**(2) 77 (1982). URL <http://dx.doi.org/10.1364/OL.7.000077>
- [80] M. V. Gromovyi, V. I. Romanenko, S. Mieth, T. Halfmann, and L. P. Yatsenko. *Storage and retrieval of coherent optical information in atomic populations*. *Optics Communications* **284**(24) 5710 (2011). URL <http://dx.doi.org/10.1016/j.optcom.2011.08.005>
- [81] S. Mieth, G. T. Genov, L. P. Yatsenko, N. V. Vitanov, and T. Halfmann. *Phase-insensitive Storage of Coherences by Reversible Mapping onto Long-lived Populations*. submitted (2015)

- [82] T. Böttger. *Laser Frequency Stabilization to Spectral Hole Burning Frequency References in Erbium-doped Crystals: Material and Device Optimization*. Ph.D. thesis, Montana State University, Bozeman Montana (2002)
- [83] T. Weidner. *Anwendung einer Zweifrequenzimpedanzanpassung zur Lichtspeicherung in  $\text{Pr}^{3+}:\text{Y}_2\text{SiO}_5$* . B.Sc. thesis, Technische Universität Darmstadt (2014)
- [84] J. Mlynek, N. C. Wong, R. G. DeVoe, E. S. Kintzer, and R. G. Brewer. *Raman Heterodyne Detection of Nuclear Magnetic Resonance*. *Physical Review Letters* **50**(13) 993 (1983). URL <http://dx.doi.org/10.1103/PhysRevLett.50.993>
- [85] N. C. Wong, E. S. Kintzer, J. Mlynek, R. G. DeVoe, and R. G. Brewer. *Raman heterodyne detection of nuclear magnetic resonance*. *Physical Review B* **28**(9) 4993 (1983). URL <http://dx.doi.org/10.1103/PhysRevB.28.4993>
- [86] R. Neuhaus. *Optisch detektierte NMR durch kohärente Ramanstreuung*. Ph.D. thesis, Universität Dortmund (2001)
- [87] D. Schraft. Ph.D. project, Technische Universität Darmstadt (2016)

## Publications and Contribution to Conferences

### Publications in Peer-reviewed Journals

- S. Mieth, G. T. Genov, L. P. Yatsenko, N. V. Vitanov, and T. Halfmann  
*Phase-insensitive Storage of Coherences by Reversible Mapping onto Long-lived Populations*  
Physical Review A **93**(1) 012312 (2016)
- S. Mieth, A. Henderson, and T. Halfmann  
*Tunable, continuous-wave optical parametric oscillator with more than 1 W output power in the orange visible spectrum*  
Optics Express **22**(9) 11182 (2014)
- S. Mieth, D. Schraft, P. Yatsenko, and T. Halfmann  
*Rephasing of optically driven atomic coherences by rapid adiabatic passage in  $Pr^{3+}:Y_2SiO_5$*   
Physical Review A **86**(6) 063404 (2012)
- M. V. Gromovyi, V. I. Romanenko, S. Mieth, T. Halfmann and L. P. Yatsenko  
*Storage and retrieval of coherent optical information in atomic populations*  
Optics Communications **284**(24) 5710 (2011)
- G. Heinze, S. Mieth, and T. Halfmann  
*Control of dark-state polariton collapses in a doped crystal*  
Physical Review A **84**(1) 013827 (2011)

### Talks at National and International Conferences

- S. Mieth, G. T. Genov, L. P. Yatsenko, N. V. Vitanov, and T. Halfmann  
*Experimental Implementation of Coherence Population Mapping in a Doped Solid*  
Workshop on Control of Quantum Dynamics of Atoms, Molecules and Ensembles by Light (CAMEL XI) – Nessebar (Bulgaria), June 2015
- G. T. Genov, S. Mieth, L. P. Yatsenko, N. V. Vitanov, and T. Halfmann  
*Phase-insensitive Mapping of Coherences onto Long-lived Populations*  
Workshop on Control of Quantum Dynamics of Atoms, Molecules and Ensembles by Light (CAMEL XI) – Nessebar (Bulgaria), June 2015
- S. Mieth, and T. Halfmann  
*An all-solid-state, high power, tunable cw laser system for quantum optics applications*

Frühjahrstagung der Deutschen Physikalischen Gesellschaft – Heidelberg (Germany), March 2015

- S. Mieth, G. Hofmann, and T. Halfmann  
*An all-solid-state, high power, tunable cw laser system for quantum optics applications*  
Workshop on Control of Quantum Dynamics of Atoms, Molecules and Ensembles by Light (CAMEL X) – Nessebar (Bulgaria), June 2014
- S. Mieth, G. Hofmann, and T. Halfmann  
*An all solid state laser system and its application in coherent data storage*  
2nd mini school – Marie Curie Initial Training Network – Coherent Information Processing in Rare-Earth Ion Doped Solids (CIPRIS) – Paris (France), August 2013
- G. Heinze, C. Hubrich, S. Mieth, and T. Halfmann  
*Enhanced optical data and image storage by EIT in Pr:YSO*  
1st mini school - Marie Curie Initial Training Network - Coherent Information Processing in Rare-Earth Ion Doped Solids (CIPRIS) – Mainz (Germany), June 2012
- G. Heinze, C. Hubrich, S. Mieth, and T. Halfmann  
*Enhanced optical data storage up to 1 second by EIT in a doped solid*  
DPG-Frühjahrstagung – Stuttgart (Germany), March 2012
- (Joint talk) G. Heinze, S. Mieth, and T. Halfmann  
*Control of dark state beating in Pr:YSO*  
Workshop on Quantum Information Processing in Rare-Earth doped Solids – Barcelona (Spain), May 2011

## Posters at National and International Conferences

- G. T. Genov, S. Mieth, L. P. Yatsenko, N. V. Vitanov, and T. Halfmann  
*Phase-insensitive Mapping of Coherences onto Long-lived Populations*  
STIRAP in Physics, Chemistry and Technology, Current Status and Future Directions 25 years after the Introduction of STIRAP – Kaiserslautern (Germany), September 2015
- S. Mieth, G. Heinze, and T. Halfmann  
*Image storage by EIT in a doped solid for up to one minute*  
11th European Conference on Atoms, Molecules and Photons – Aarhus (Denmark), June 2013
- A. Henderson, S. Mieth, and T. Halfmann  
*CW OPO for quantum optics applications*  
21st International Conference on Laser Spectroscopy – Berkeley (USA), June 2013

- A. Henderson, S. Mieth, and T. Halfmann  
*3 Watt CW OPO tunable 604nm to 616nm for quantum optics applications*  
43rd Annual Meeting of the APS Division of Atomic, Molecular, and Optical  
Physics – Orange County (USA), June 2012

## Supervised Theses and Contribution to Teaching

### Master Theses

- Tobias Zöller, *to be written*, TU Darmstadt 2015
- Moritz Kick, *Aufbau eines Experiments zur Lichtspeicherung in Eu:YSO*, TU Darmstadt 2015
- Sören Kaufmann, *Lichtspeicherung in Pr:YSO mittels atomarer Frequenzkämme, getrieben durch ein OPO-Lasersystem*, TU Darmstadt 2015
- Nils Vogelmann, *Verlängerung der Speicherzeit atomarer Kohärenzen mittels Konversion in Besetzungen*, TU Darmstadt 2012

### Bachelor Theses

- Felix Weigand, *Spektroskopische Charakterisierung der Hyperfeinübergänge in Eu:YSO*, TU Darmstadt 2015
- Philip Prediger, *Besetzungsmanipulation durch Hochfrequenzpulse in Eu:YSO*, TU Darmstadt 2015
- Thomas Weidner, *Anwendung einer Zweifrequenzimpedanzanpassung zur Lichtspeicherung in Pr:YSO*, TU Darmstadt 2014
- Gregor Hofmann, *Erweiterungen zur automatischen Ansteuerung eines optisch-parametrischen Oszillators*, TU Darmstadt 2013
- Christian Hoyer, *Aufbau eines Resonators hoher Finesse zur Linienbreitenmessung*, TU Darmstadt 2013
- Nikolaus Lorenz, *Frequenzstabilisierung eines Lasers mittels akustooptischer Modulation*, TU Darmstadt 2012

### Contribution to Teaching

- SS 2011 - today, Supervision of the advanced lab course (Experiment 4.11: Optical pumping)
- Supervision of student seminar presentations:  
*Stabilisierungstechniken von AMO-Lasern* (WS 2013/2014)  
*Photonen-Echos* (WS 2012/2013)  
*Erzeugung durchstimmbarer Laserstrahlung* (WS 2011/2012)



# Curriculum Vitæ

of Simon Robert Mieth,  
born February 20, 1984 in Berlin,  
currently living in Frankfurt am Main.

---

## Education

1990 - 1994	Attendance of the Trinkborn Elementary School in Rödermark
1994 - 2003	Attendance of the Oswald von Nell-Breuning High School in Rödermark
06/2003	A-levels at the OvNB High School Rödermark

---

## University Education

2004 - 2007	Physics Studies (B.Sc) at TU-Darmstadt
11/2007	Bachelor of Science Degree in Physics
2008 - 2010	Physics Studies (M.Sc) at TU-Darmstadt
02/2009 - 10/2009	Semester Abroad at Pontificia Universidad Catolica de Chile, Santiago de Chile
11/2010	Master of Science Degree in Physics
since 02/2011	Doctoral Studies at the Department of Physics, TU-Darmstadt (Nonlinear and Quantum-Optics Group)

---

## Working Experience

09/2003 - 06/2004	Civil Service in the Paramedics Division of the German Red Cross, Darmstadt/Dieburg
2008 - 2010	Temporary Job in the Medical Emergency Service (Malteser Hilfsdienst) and the German Red Cross Paramedics Division, Darmstadt
since 02/2011	Graduate Researcher at TU-Darmstadt (Nonlinear and Quantum-Optics Group), from 01/2012 to 12/2014 as Stipendiary of the <i>Stiftung der deutschen Wirtschaft</i>

Darmstadt, October 12, 2015

# Acknowledgement

Keine Arbeit schreibt oder erledigt sich von alleine und selten bis gar nicht nur durch eine Person. Zum Gelingen dieser Arbeit haben eine Vielzahl von Menschen beigetragen, denen mein aufrichtiger und herzlicher Dank gilt. Danke

**Thomas**, für deine umfassende Betreuung während meiner Promotion in den letzten viereinhalb Jahren! Du hast mich in dieser Zeit nicht nur wissenschaftlich unterstützt sondern auch in vielen anderen Bereichen gefördert und gefordert. Dadurch ist meine Zeit in deiner Arbeitsgruppe immer spannend und vielseitig geblieben. Ich habe deine Betreuung immer als angenehm persönlich empfunden, was bestimmt mit der Grund ist, warum du ein so tolles Team hast und in Zukunft hoffentlich auch immer haben wirst. Vielen Dank Thomas!

**Thomas Walther**, bei Ihnen habe ich die ersten wissenschaftlichen Gehversuche im Rahmen meiner Bachelorarbeit unternommen. Aber auch darüber hinaus haben sie mir immer wieder mit ihren positiven und sehr persönlichen Zweitgutachten, nicht zuletzt für meine Promotion, das Öffnen vieler Türen ermöglicht! Ich finde das in keiner Weise selbstverständlich und möchte Ihnen dafür herzlich danken.

**Leonid, Nikolai and Bruce**, without you, my thesis would miss an entire chapter! Your support on CPM was enormous and more than once, your interest and our discussions encouraged me to continue working on this topic, which finally succeeded. It was a pleasure to have met you.

**Danielowitsch**, zusammen haben wir unsere Masterarbeit in der AGH begonnen und es ist zu einem gemeinsamen Arbeiten geworden, dass uns bis in die Promotion begleitet hat. Wir freuen und regen uns über die gleichen Dinge auf, und so bist du mein vertrautester Kollege während der vergangenen Jahre geworden. Ich wünsche Dir viel Erfolg auf den letzten Metern deiner Promotion und hoffe, dass wir uns nicht aus den Augen verlieren werden.

**Georg**, Du bist wohl immer irgendwie mein Betreuer aus der Masterarbeit geblieben! Bei dir habe ich mir oft Rat fürs Labor oder die Betreuung von Studenten geholt. Deine Meinung war und ist mir wichtig und ich schätze sie sehr. Noch mehr schätze ich aber die Zeit, die wir hier in Darmstadt zusammen auf der Arbeit verbracht haben, sie war gezeichnet von lehrreichen und vor allem humorvollen Stunden. Ein Blick am Kaffeetisch genügte um zu verstehen über was wir grade

beide lachen, so etwas ist wichtig und ich hoffe für uns beide, dass wir das nicht verlieren!

**Genko**, thank you for your massive theory support and company during almost all final measurements for my PhD thesis, which often ended in after-measurement-midnight dinners in the Cafe Chaos! I enjoyed it very much and I wish you all the best for your upcoming time as an experimentalist in Darmstadt.

**Doktorandenstammtisch**, mit Euch habe ich einst angefangen zu studieren und unser fast wöchentlicher Austausch über diverse Sorgen und Freuden hat mir über so manche schwere Stunde hinweggeholfen und mir oft gezeigt, dass der eingeschlagenen Weg schon zu einem guten Ende führen wird.

**PrYSO/EuYSO Team**, für die beinahe ausnahmslos gute Arbeitsatmosphäre und den Eifer, mit dem wir zusammen gemessen, diskutiert und gelacht haben. Insbesondere geht mein Dank hier an die Studenten, die ich betreuen durfte oder mit denen ich gemeinsam an meinen Promotionsprojekten gearbeitet habe, namentlich **Moritz, Nikolaus, Gregor, Marcel, Sören, Thomas (Weidner), Nils, Tobias, Felix, Philip** und **Christian (Hoyer)**.

**AG Halfmann**, für eine gute Zeit bei und neben der Arbeit wie zum Beispiel bei unseren Gruppenausflügen, am Kaffeetisch und vielen Gelegenheiten mehr. Mein Dank geht dabei insbesondere an die Kollegen, die mich über längere Zeit durch die Promotion begleitet haben, **Patric, Frank, Uwe, Christian, Nina, Andreas, Fabian Beil, Thorsten** und **Lacho**. **Damaris** und **Nafiseh**, euch ebenfalls ein herzliches Danke für die Unterstützung aus organisatorischer Perspektive - selbst nach dem 100sten falsch ausgefüllten Dienstreiseantrag oder CIPRIS Timesheet habt ihr Ruhe bewahrt und mich nicht direkt ans Kreuz genagelt ;).

**Team der Feinmechanik- und Elektronikwerkstätten**, für schnelle, hilfsbereite und zuverlässige, aber vor allem unersetzliche Arbeiten rund ums Experiment!

Nicht zu letzt möchte ich meiner **Familie** danken. Ihr habt mich bedingungslos unterstützt und motiviert, so dass ich auch in schweren Zeiten nicht aufgeben konnte. Danke auch Dir **Mônica**, für Deine Unterstützung bis zum Schluss, ob von Deutschland oder von Brasilien aus - wir sehen uns bestimmt noch mindestens einmal wieder.

Liebe **Freunde**, auch ihr habt einen wesentlichen Teil zum Gelingen dieser Arbeit beigetragen. Vielleicht nicht im Labor, aber in der gesamten übrigen (wenn auch spärlichen) Zeit. Ihr seid - wie auch meine Familie - Rückhalt und Ausgleich, dafür danke.

Simon Mieth

Darmstadt (Dezember 2015)



# Erklärung zur Dissertation

Hiermit versichere ich, die vorliegende Dissertation ohne Hilfe Dritter nur mit den angegebenen Quellen und Hilfsmitteln angefertigt zu haben. Alle Stellen, die aus Quellen entnommen wurden, sind als solche kenntlich gemacht. Diese Arbeit hat in gleicher oder ähnlicher Form noch keiner Prüfungsbehörde vorgelegen.

Darmstadt, den 12. Oktober 2015

---

(Simon Robert Mieth)